

Diss. ETH No. 20496

**FILM COOLING
USING ANTI-KIDNEY VORTEX PAIRS
INVESTIGATED BY
LARGE-EDDY SIMULATION**

A dissertation submitted to

ETH ZURICH

for the degree of

Doctor of Sciences

presented by

Lars Gräf

Dipl.-Ing., Universität Stuttgart

born on December 30, 1980

citizen of Germany

accepted on the recommendation of

Prof. Dr.-Ing. L. Kleiser, examiner

apl. Prof. Dr.-Ing. U. Rist, co-examiner

2012

Printed by Grafische Werkstätte, BruderhausDiakonie, Stiftung Gustav Werner und Haus am Berg, Reutlingen.

A digital version of this thesis can be downloaded from ETH E-Collection: URL: <http://e-collection.ethbib.ethz.ch>

DOI: 10.3929/ethz-a-007336234

Abstract

Film cooling is an important measure to allow for an increase of gas turbine inlet temperatures and, thereby, to improve the engine's overall efficiency. The coolant is ejected through spanwise rows of holes in the blades or endwalls to build up a film shielding the material from hot gases. The holes often are inclined in the downstream direction and give rise to a kidney vortex pair. This counter-rotating vortex pair features an upward flow direction between the two vortices, which tends to lift the vortices off the surface and locally feeds hot air towards the blade outside the pair. Reversing the rotational sense of the vortices reverses these two drawbacks into advantages. In the case considered in this work, an anti-kidney vortex pair is generated using two subsequent rows of holes both inclined downstream and yawed in the spanwise direction with alternating yaw angles.

For validation of the computational setup, Large-Eddy Simulations of a turbulent flat-plate boundary layer are conducted using the relaxation term of the Approximate-Deconvolution Model to model the sub-grid scales. A Finite-Volume flow solver with up to fourth-order accurate numerical schemes is used and the computational domain is discretized by block-structured grids with 38 million cells at most. Results are found to be in good agreement with Direct Numerical Simulation data and the law of the wall. The variation of grid topology, extent of the computational domain, and grid resolution only show minor influence on the simulation results.

A film-cooling configuration is investigated which includes a coolant plenum and two cooling holes in an arrangement which generates the above-mentioned anti-kidney vortex pair. This vortex pair achieves a film-cooling effectiveness which is comparably high. The anti-kidney reference case is studied at a high resolution yielding results which agree reasonably well with experimental data. The flow in the coolant plenum, inside the coolant holes, and above the plate is studied in detail focussing on the vortical structures.

Finally, film-cooling parameters are altered towards engine conditions. The achieved cooling and the generated losses are studied at different coolant-to-freestream mass-flux ratios ($M = 1 \dots 2$) at an engine-like density ratio ($DR = 2$). In addition, the yaw angle ($\beta = 30^\circ \dots 60^\circ$) influence is studied to optimize the spanwise spreading of the film. The simulations show that the anti-kidney vortex configuration may locally obtain a higher cooling effectiveness for

high-momentum ratios than fan-shaped cooling, which is generally assumed to perform better at these parameters. In the vicinity of the cooling holes, however, fan-shaped holes are still superior.

Kurzfassung

Filmkühlung ist eine bedeutende Massnahme, um einen Anstieg der Gasturbinen-Eintrittstemperaturen zu ermöglichen und dadurch die Gesamteffizienz der Turbine zu verbessern. Das Kühlmittel strömt durch spannweitig angeordnete Lochreihen in den Schaufeln oder Seitenwänden aus, um einen Film aufzubauen, der das Material vor heissen Gasen schützt. Die Löcher werden häufig in Strömungsrichtung angestellt und rufen ein nierenförmiges Wirbelpaar hervor. Dieses gegenläufig rotierende Wirbelpaar zeichnet sich durch einen Drehsinn aus, der zwischen den beiden Wirbeln weg von der Wand weist, was ein Abheben der Strömung von der Oberfläche begünstigt, und befördert seitlich des Paares lokal heisse Luft zur Wand hin. Ein Umkehren des Drehsinns der Wirbel kehrt auch diese Nachteile in Vorteile um. Im in dieser Arbeit betrachteten Fall wird ein Anti-Nierenwirbelpaar durch zwei nacheinander angeordnete Lochreihen erzeugt, die beide stromab angestellt sind und deren spannweite Schiebewinkel alternieren.

Zur Validierung der Berechnungsmethoden werden Grobstruktursimulationen einer turbulenten ebenen Plattengrenzschicht durchgeführt, die den Relaxationsterm des Approximate-Deconvolution-Modells für die turbulente Feinstruktur verwenden. Ein Finite-Volumen-Strömungslöser mit bis zu vierter Ordnung genauen numerischen Schemata wird verwendet, und das Rechengebiet wird durch block-strukturierte Gitter mit maximal 38 Millionen Zellen diskretisiert. Die gewonnenen Ergebnisse stimmen gut mit direkten numerischen Simulationsdaten und dem turbulenten Wandgesetz überein. Die Variationen der Gittertopologie, der Abmasse des Rechengebiets und der Gitterauflösung zeigen lediglich geringe Auswirkungen auf die Simulationsergebnisse.

Eine Filmkühlungsanordnung mit einem Kühlmittelpenum und zwei Kühllöchern wird untersucht, die das oben erwähnte Anti-Nierenwirbelpaar erzeugt. Dieses Wirbelpaar erreicht eine vergleichbar hohe Filmkühlungseffektivität. Der Referenzfall mit Anti-Nierenwirbelpaar wird mit einer hohen Auflösung untersucht und erzielt Ergebnisse, die im Einklang mit experimentellen Daten stehen. Die Strö-

mung im Kühlmittelpenum, in den Kühllöchern und oberhalb der Platte wird detailliert mit Schwerpunkt auf den Wirbelstrukturen untersucht.

Schliesslich werden die Filmkühlungsparameter entsprechend realistischen Verhältnissen in Gasturbinen angepasst. Die erzielte Kühlung und die verursachten Verluste werden bei verschiedenen Massenflussverhältnissen von Kühlmittel zu Freistrom ($M = 1 \dots 2$) und einem praxisrelevanten Dichteverhältnis ($DR = 2$) untersucht. Zusätzlich wird der Schiebewinkeleinfluss ($\beta = 30^\circ \dots 60^\circ$) untersucht, um die spannweitige Filmausbreitung zu optimieren. Die Simulationen zeigen, dass das Anti-Nierenwirbelpaar bei hohen Impulsverhältnissen lokal eine höhere Kühleffektivität erreichen kann als das fächerförmige Kühlen, von dem bei diesen Parametern üblicherweise angenommen wird, es schneide besser ab. Im unmittelbaren Umfeld der Kühllöcher sind die fächerförmigen Löcher allerdings nach wie vor überlegen.

Acknowledgments

I would like to thank my supervisor L. Kleiser for giving me large latitude to pursue research and for fruitful discussions. Many thanks also to U. Rist (Universität Stuttgart) for acting as a co-examiner of my dissertation. Moreover, I would like to thank him for hospitality during my HPC-Europa2 visit.

I am grateful to M. Schnieder (Alstom Baden) for most helpful discussions and suggestions on aspects relevant to application in gas turbines. Furthermore, I acknowledge good discussions with Jan Vos (CFS Engineering Lausanne) on details of the flow solver NSMB and his instrumental comments on this thesis.

All simulations were conducted at HLRS Stuttgart and I am much obliged to the staff members T. Bönisch, J. Hertzner, and Alexander Schulz for essential help without red tape. In particular, I am indebted to Stefan Haberhauer (NEC Deutschland) for countless hints on performance optimization and solving issues related to the computing environment.

Further thanks to (former) staff of the Institute of Fluid Dynamics (IFD). Bianca Maspero was very obliging especially with respect to administrative issues. I am grateful to Michael John and Robert Tritarelli for proof reading. I am also thankful to Andreas Jocksch and Felix Keiderling for fruitful discussions. I learned a lot from Rolf Henniger who never got tired to explain numerics to me and did a lot of proof reading. Stimulating discussions with and careful corrections from Stefan Bühler were most helpful for my project. IFD's Beer Club is acknowledged for improving my work-life-balance.

Most importantly, I thank my friends and family. Especially my wife Caro and our son Jonathan make me incredibly happy every day.

This work was partly funded by the Swiss National Science Foundation (SNF) with the project number 200020-116310. The computing resources were granted by the DEISA Consortium, co-funded through the EU FP7 project RI-222919 within the DEISA Extreme Computing Initiative under the project acronyms FCool2 and FCool3. Further computing time as well as the research visit in Stuttgart was funded by the HPC-Europa2 project with the project number 228398 with the support of the European Commission, Capacities Area, Research Infrastructures.

Contents

Nomenclature	V
1 Introduction	1
1.1 Motivation for film cooling	1
1.2 Simple and anti-kidney vortex pair film-cooling	5
1.3 Simulations of film cooling	9
1.4 Objectives and outline	10
2 Methods	13
2.1 Governing equations	13
2.2 Finite-Volume discretization	16
2.2.1 Advective flux approximation	17
2.2.2 Diffusive flux approximation	19
2.2.3 Time integration and computer code	20
2.3 Turbulence modeling	21
2.3.1 LES approach: relaxation term model	21
2.3.2 Turbulent inflow: Synthetic-Eddy Method	24
2.4 Boundary treatment	26
2.4.1 Characteristic boundary conditions	27
2.4.2 Sponge zones	28
2.5 Postprocessing	29
2.5.1 Cooling and loss measures	29
2.5.2 Vortex identification	30
3 Turbulent flat-plate boundary layer: validation case	35
3.1 Simulation setup	36
3.1.1 SEM parameters	37
3.1.2 Boundary and initial conditions and transient	38
3.1.3 Computational grid	39
3.2 Results of non-Cartesian grid	40
3.2.1 Velocities and effect of inflow treatment	40
3.2.2 Inflow transient and effect of outflow treatment	41
3.2.3 Instantaneous flow	43
3.3 Grid and Mach number variation	44
3.4 Summary	47

4	Film cooling: reference case	49
4.1	Simulation setup	50
4.1.1	Boundary and initial conditions	52
4.1.2	Computational grid	53
4.1.3	Quasi-steady state	56
4.2	Mean flow in the plenum	57
4.3	Mean flow in the cooling holes	61
4.3.1	Flow separation and jetting region	61
4.3.2	Double counter-rotating vortex pair	64
4.3.3	Mean flow in the hole-plate orifices	65
4.4	Mean flow above the plate	67
4.4.1	Comparison of cooling film with experiment	67
4.4.2	Heat-mass transfer analogy	69
4.4.3	Anti-kidney vortex pair and effectiveness distribution	70
4.4.4	Horseshoe and degenerated vortices	75
4.5	Instantaneous flow and generalized vorticity	76
4.5.1	Frequency analysis	78
4.5.2	Generalized vorticity	82
4.6	Summary	85
5	Film cooling: application-oriented cases	87
5.1	Simulation setup	88
5.1.1	Boundary and initial conditions	89
5.1.2	Initial transient and quasi-steady state	89
5.1.3	Computational grid and effect of resolution and dimensions	90
5.2	Effect of blowing conditions	93
5.2.1	Cooling at different blowing conditions	97
5.2.2	Losses at different blowing conditions	101
5.3	Effect of yaw angle	102
5.3.1	Cooling at different yaw angles	103
5.3.2	Losses at different yaw angles	106
5.4	Summary	107
6	Conclusions and recommendations	109

A	Miscellaneous	113
A.1	Flow chart of NSMB	113
A.2	Wall-normal grid stretching	114
A.3	Fourier transform	117
B	Computational aspects	121
B.1	Sequential performance of individual code components . .	122
B.2	Overall parallel performance	123
B.3	Summary	126
	Bibliography	127
	Publications	139
	Curriculum vitae	140

Nomenclature

Roman symbols

A	area
\vec{A}	outward-pointing cell-surface vector with a length corresponding to the surface area
a	speed of sound
\mathbf{a}	Cholesky decomposition of Reynolds-stress tensor
\vec{B}	baroclinic torque, cf. Eq. (4.2)
c	coolant concentration
D	coolant diffusion rate
d	cooling-hole diameter
DR, DR_p	density ratio = ρ_c/ρ_∞ and = ρ_p/ρ_∞ , respectively
E	energy
F	high-pass filter
\underline{E}, f	flux, cf. Sec. 2.1
f	frequency
f_c	cutoff frequency of a filter
f_k	Kolmogorov frequency of a flow
f_n	(Nyquist frequency or) resolved frequency on grid
$G, G_{i,j,k,3D}$	primary filter: one-dimensional, in the i -, j -, k -direction, and three-dimensional, respectively
H	boundary-layer shape factor
h	enthalpy
I	momentum ratio = $(\rho U^2)_c/(\rho U^2)_\infty$
\mathbf{I}	identity matrix = $\begin{bmatrix} 1 & 0 & 0 \\ 0 & 1 & 0 \\ 0 & 0 & 1 \end{bmatrix}$
i	imaginary unit = $\sqrt{-1}$
i, j, k	indices in computational space
k	thermal conductivity; turbulent kinetic energy
L	cooling-hole length; amplitude of characteristic wave
L_x	streamwise domain length
L_z	spanwise domain width
Le	Lewis number
M	(blowing or) mass-flux ratio = $(\rho U)_c/(\rho U)_\infty$
\dot{m}	mass-flux
Ma	Mach number

N	deconvolution order; number of samples
N_{eddy}	number of synthetic eddies
N_K	kinematical vorticity number, vortex criterion
N_p	number of processors
$N_{x,y,z,\text{cell}}$	number of cells in the x -, y -, z -direction, and total number of cells, respectively
\vec{n}	outward-pointing unit normal-vector
P	spanwise pitch of two neighboring holes in the same row; floating-point performance
p	(static) pressure
PR_p	pressure ratio = p_p/p_∞
Pr	Prandtl number
\vec{q}	heat-flux vector
R	universal gas constant
\mathbf{R}	Reynolds-stress tensor
r	recovery factor; radial coordinate
Re	Reynolds number
S	streamwise spacing of two rows; surface of a finite volume; parallel speedup
\mathbf{S}	rate-of-strain tensor
\vec{S}	vortex stretching and tilting, cf. Eq. (4.2)
s	equivalent slot width; entropy; cell-side index
Sc	Schmidt number
t	time
T	temperature
T_r	recovery temperature
TR	temperature ratio = T_c/T_∞
U	velocity in the direction of principal flow, i.e. parallel to y , along hole axis, or parallel to x
\underline{U}	state vector in conservative variables, cf. Eq. (2.2)
\vec{u}	velocity vector = $[u \ v \ w]^T$
\vec{u}_{ind}	velocity induced by synthetic eddies
u_τ	friction velocity
u, v, w	velocities in the x -, y -, z -direction, respectively
V	volume
\underline{V}	state vector in primitive variables
V_B	volume of synthetic-eddy box
VR	velocity ratio = U_c/U_∞
\vec{x}	location vector = $[x \ y \ z]^T$
x, y, z	Cartesian coordinates in the downstream, plate-normal, and spanwise direction, respectively, cf. Figs. 3.1 and 4.3

Greek symbols

α	inclination angle, i.e. between cooling hole and plate, cf. Fig. 1.3
β	(orientation or) yaw angle, cf. Fig. 1.3
γ	(ratio of specific heats or) isentropic exponent; plenum shear angle
Δ	vortex criterion
δ	distance from synthetic eddy to grid point
$\delta_{U,99\%,95\%}$	velocity boundary-layer thickness (location where 99% and 95% of the freestream velocity is reached, respectively)
$\delta_{\Theta,95\%}$	temperature boundary-layer thickness (location where $\Theta = 0.05$)
δ_{ij}	Kronecker delta = \mathbf{I}
ε	turbulent dissipation rate
$\vec{\varepsilon}$	rotation direction of synthetic eddy = $[\pm 1 \pm 1 \pm 1]^T$
η	adiabatic film-cooling effectiveness (for brevity referred to as effectiveness), Eq. (2.34)
Θ	non-dimensional temperature, Eq. (2.34)
ϑ	boundary-layer momentum thickness
κ	wave number
λ	characteristic velocity; eigenvalue
λ_2	median eigenvalue, vortex criterion
μ	dynamic viscosity
ν	kinematic viscosity
ξ	loss coefficient, Eqs. (2.35) to (2.38)
ξ, ξ', η, ζ	additional Cartesian coordinates, cf. Fig. 4.3
ρ	density
σ	length scale of synthetic eddy; sponge strength; integration region of vorticity criterion; staggering parameter
τ	shear-stress tensor
ϕ, ψ	substitutes
χ	relaxation coefficient; substitute
Ω	finite volume
$\mathbf{\Omega}$	rate-of-rotation tensor
$\vec{\Omega}$	generalized vorticity = $\vec{\omega}/\rho$
$\vec{\omega}$	vorticity = $[\omega_x \ \omega_y \ \omega_z]^T$

Indices

∞	freestream property
1, 2	upstream and downstream cooling hole, respectively
adv	(inviscid or) advective (flux)
b	property at the boundary
c	coolant property, averaged over injection areas at $y/d = 0$
diff	(viscous or) diffusive (flux)
f	film property, averaged above the plate at $x/d = 20$
g1, g2	property in the first and second ghost cell, respectively
h	hot-gas property, averaged above the plate at $x/d = -7$
hp	high-pass filter
i1, i2, ...	property in the first, second, ... cell, respectively
NS	Navier Stokes
p	plenum property, averaged downstream of the sponge at $y/d \approx -7.3$
ref	reference state
rms	root mean square, e.g. $u'_{\text{rms}} = \sqrt{\langle u'u' \rangle_t}$
s	staggered grid
t	(stagnation or) total property

Other symbols and operators

\cdot	(inner or) scalar product, e.g. $\vec{\chi} \cdot \vec{\psi}$, $\phi = \chi \cdot \psi$, or $\vec{\phi} = \chi \cdot \vec{\psi}$
\times	cross product, e.g. $\vec{\phi} = \vec{\chi} \times \vec{\psi}$
\otimes	(dyadic or) tensor product, e.g. $\vec{\phi} = \vec{\chi} \otimes \vec{\psi}$
$\vec{\nabla}$	Cartesian divergence or gradient operator, i.e. $= [\partial/\partial x \ \partial/\partial y \ \partial/\partial z]^T$
$\vec{0}$	zero vector = $[0 \ 0 \ 0]^T$
ϕ	tensor = ϕ_{ij}
$\hat{\phi}$	amplitude of Fourier transform ϕ
$\vec{\phi}$	geometrically interpreted column vector = $[\phi_x \ \phi_y \ \phi_z]^T$
$\underline{\phi}$	list of scalars condensed in a column vector, e.g. state vector
$\vec{\underline{\phi}}$	geometrically interpreted column vector of condensed scalars = $[\underline{\phi}_x \ \underline{\phi}_y \ \underline{\phi}_z]^T$, cf. fluxes
ϕ'	Reynolds-decomposed fluctuation = $\phi - \langle \phi \rangle_t$
ϕ^+	ϕ normalized in wall units using the inflow friction velocity $u_\tau _{x/d=-14}$
ϕ^n	property ϕ at time-step n
$\langle \phi \rangle_\psi$	quantity ϕ averaged over ψ
$\phi _\psi$	quantity ϕ at position or time ψ

Abbreviations

ADM	Approximate-Deconvolution Model
CFL	Courant-Friedrichs-Lewy (condition or number)
DNS	Direct Numerical Simulation
GFLOPS	billion floating-point operations per second
LES	Large-Eddy Simulation
LIC	Line-Integral Convolution
MPI	Message Passing Interface
NSMB	Navier-Stokes multi-block (code)
RANS	Reynolds-Averaged Navier-Stokes
SEM	Synthetic-Eddy Method
URANS	Unsteady RANS

Simulation cases

1	turbulent boundary-layer flow with small, Cartesian grid
2	turbulent boundary-layer flow with large, non-Cartesian grid
3	film-cooling flow with $ \beta = 45^\circ$
31, 41, 51	cases 3, 4, and 5 with long domain, respectively
32	case 3 with long, high domain
4	film-cooling flow with $ \beta = 60^\circ$
5	film-cooling flow with $ \beta = 30^\circ$
a	grid resolution of $\Delta y_{\min}^+ = \sqrt{2}/2$
b	grid resolution of $\Delta y_{\min}^+ = 1$
c	grid resolution of $\Delta y_{\min}^+ = \sqrt{2}$
d	grid resolution of $\Delta y_{\min}^+ = 2$
α	$DR \approx 0.9, M \approx 1.0, Ma_\infty = 0.2$
β	$DR \approx 2.0, M \approx 1.5, Ma_\infty = 0.2$
γ	$DR \approx 2.0, M \approx 1.0, Ma_\infty = 0.2$
δ	$DR \approx 2.0, M \approx 2.1, Ma_\infty = 0.2$
ε	$Ma_\infty = 0.4$

Chapter 1

Introduction

Gas turbines, also referred to as gas generators, convert energy of a continuous, highly exothermic reaction of a burnable gas and an oxidizer, which usually is air. A schematic view of a gas turbine is shown in Fig. 1.1(a). In the compression section, ambient air is sucked in at position 1, compressed and transferred via position 2 into the combustor. There, the air is mixed with the burnable gas and this mixture is ignited. Beyond position 3, the burnt gas enters the turbine, propels it and expands to exit conditions at position 4. The rotation of the turbine shaft is finally converted into the desired energy. Moreover, the shaft drives the compressor, after a separate starter unit has brought the machine to design state.

Gas turbines are used in three different fields, which are air, land, and sea. Depending on the field of application, their energy is consumed differently, cf. Soares (2007). For most airplane applications, either the hot jet exclusively propels the aircraft (turbojet) or it is supplemented by the turbine shaft driving a propeller (turboprop) or a fan (turbofan). Turbines at land and sea are quite similar. Their area of application ranges from power plants and tanks to drilling rigs and naval ships. They are coupled, directly or through a gearbox, with either an electric power generator or a mechanical device, e.g. to propel a ship or to drive a pump.

1.1 Motivation for film cooling

The use of gas turbines on average kept increasing over the last decades. It can be split into two sectors being the power generation and the airplane propulsion. Attributed to the economy crisis in 2009, the first decline of global primary energy consumption since 1982 occurred implying a rise in the rest of the period, cf. BP p.l.c. (2010, p. 2). Until 2030, an annual growth of primary energy consumption by 1.6% is predicted by BP p.l.c. (2012, p. 9). Also, the passenger kilometers on international flights are expected to grow by 4.5% to 6.0% annually for the time period from 2007 to 2027, see Gillen (2009, Tab. 1). It used to increase by 3.4% to 6.2% from 1990 to 2007.

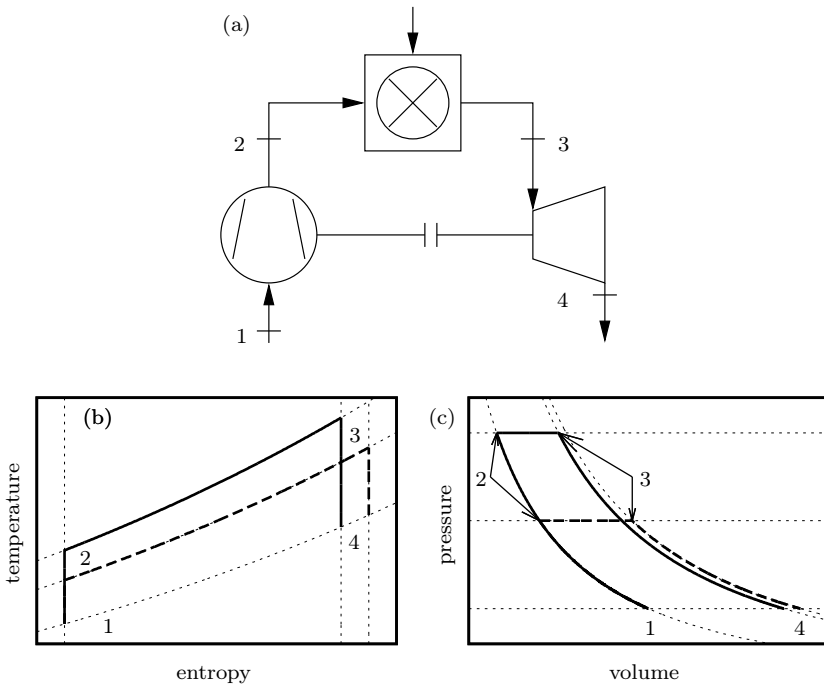


Figure 1.1: (a): Schematic of a gas turbine from Baehr & Kabelac (2009) and (b), (c): ideal Brayton cycle. (.....): Isobar and isentrop; (- - -): low pressure; (—): high pressure.

Consequently, developing more efficient gas turbines is of general and increasing interest. To achieve this, improving the turbine cooling system is one measure among many others, e.g. increasing the combustion's efficiency or developing new materials.

One may differentiate two modes of gas turbine cooling. First, as the term cooling suggests, the temperature of the cooled materials is reduced and, hence, the lifetime of the cooled section is increased. As example, a reduction of the effective material temperature by 25 K can double the turbine blade lifetime, cf. Bogard & Thole (2006, Sec. I). If one keeps the lifetime constant, other protecting measures can be reduced, depending on economic assessment, or blades might be designed lighter which is interesting for turbines in airplanes. Second, maintaining the effective temperatures of the sensitive parts while using

a more efficient cooling technique either allows for higher temperatures of the combustion or diminishes the required coolant which is used to protect or cool material and sometimes even is mixed with the burnt gas in order to reduce the effective gas temperature directly.

Both hotter combustion and less coolant increase the overall turbine efficiency. Thermodynamically, the basic gas turbine process is described by the Brayton cycle. Figures 1.1(b) and 1.1(c) show an ideal Brayton cycle, which is a strong simplification of a real gas turbine neglecting any losses due to friction, cooling, and leakage. The area enclosed by the isobars and isentrops in Fig. 1.1(b) is larger for the high pressure compared to the low pressure cycle. Consequently, the energy gain is larger for high compression rates which goes along with an increase of the combustion temperature. Second, the coolant mass-flux reduces the energy gained in the turbine, as well as the overall efficiency, since the effective temperature in the turbine is reduced. Consequently, the aim is to obtain a high level of cooling at a low coolant mass-flux.

Cooling is inevitable as the combustion temperature, ranging from 2100 to 2300 K, is beyond the maximal allowable material temperature of 1100 to 2000 K, following data from Soares (2007, Chap. 4). The coolant is usually air at 470 to 820 K, which is either taken from an intermediate stage of the compressor or put aside before it enters the combustor. The choice depends on the pressure level at which the coolant is required to cool a particular turbine stage.

Three areas are to be cooled: the combustion chamber walls, the turbine blades and the turbine endwalls. The turbine parts require intense cooling mainly in the first stages. The cooling can be achieved via convective or impingement cooling. Alternatively, the material can be shielded from the hot gas by applying a thermal barrier coating on the surface or establishing a coolant film. Each of these methods is used in all three areas and they usually appear in a hybrid manner. There is another rarely used method termed transpiration cooling: ejecting coolant through porous media. In the present work, only film cooling is studied which, according to Bunker (2007), is one of the ten remaining challenges in the hot gas path of gas turbines.

The general knowledge reproduced in parts of this introduction may be studied more deeply in Soares (2007). There are review articles concerning gas turbine cooling by Bunker (2007); Han et al. (2000), concerning film cooling by Bogard & Thole (2006); Goldstein (1971), cooling-hole exits by Bunker (2005), and blade tip cooling by

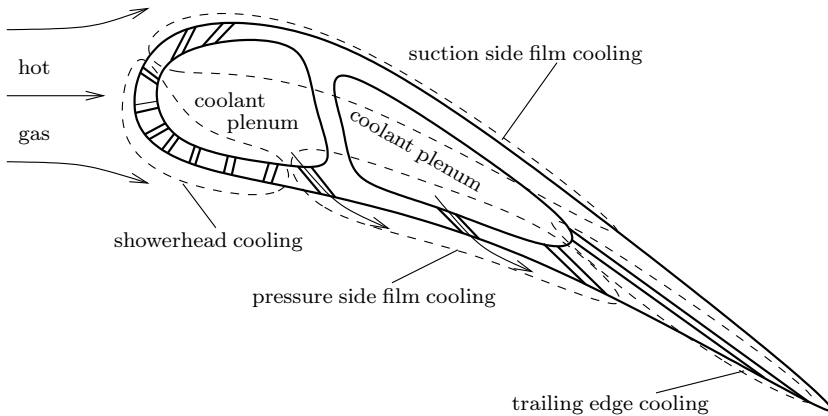


Figure 1.2: Sketch of cooled blade, adapted from Han et al. (2000, Fig. 1.10)

Sunden & Xie (2010).

Roughly speaking, a coolant film shields the blades from the hot gas arriving from the combustion chamber. This film is set up by coolant from the blade interior, which is ejected through various holes in spanwise rows to the outer surface of the blade. Figure 1.2 illustrates a state-of-art blade using shower-head cooling at the blade-tip, normal film-cooling at the pressure and suction sides, and coolant ejection at the trailing edge.

The injected coolant can be considered as a heat sink, lowering the temperature of the hot boundary layer, in addition to the shielding or insulating effect of the film. Following Goldstein (1971), both functions are effective and there is usually no perfect film structure present but considerable mixing of coolant and hot gas. Two counteracting mechanisms determine the cooling effectiveness (effectiveness, cooling effectiveness, and adiabatic film-cooling effectiveness are used as synonyms from now on). The boundary layer thickness may be increased, which decreases the heat transfer from the hot gas to the blade, on the one hand. On the other hand, the increased entrainment of hot gas into the boundary layer, due to its thickening, dilutes the coolant, which finally weakens the heat sink.

The occurring surface curvature differs notably due to the different regions at which film cooling is employed. While at endwalls and in a typically used ring combustor, mild convex and concave curvature in the spanwise direction appears, partly strong curvature, mainly in the streamwise direction, can be found at the blades. Nevertheless, the

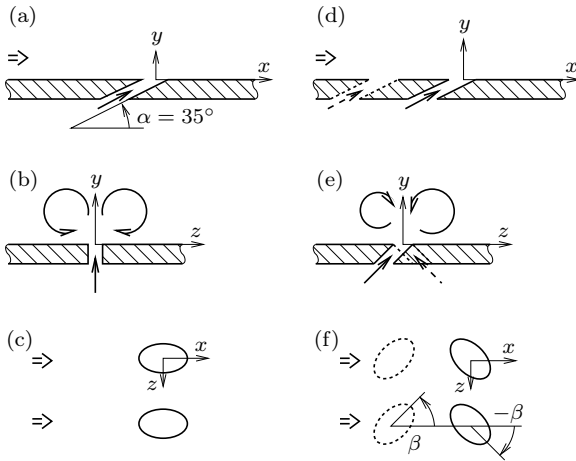


Figure 1.3: Injection geometry and resulting vortices. (a)–(c): Kidney-vortex pair from simple-angle injection; (d)–(f): anti-kidney vortex pair; (a), (d): side, (b), (e): downstream, and (c), (f): top view.

blade is simplified as a flat plate, as customary in such fundamental studies. The rotation is neglected for further simplification and also since film cooling is used in the fixed combustion chamber. Finally, we neglect the unsteadiness of the oncoming flow due to the combustion or passing blades of previous stages. From now on, we restrict our focus to turbine blade film-cooling.

1.2 Simple and anti-kidney vortex pair film-cooling

There is a vast body of literature on film cooling and we only introduce the most important forms of film cooling by citing representative papers.

In the basic case, referred to as simple-angle injection, cylindrical cooling holes are inclined towards the plate by an angle α and oriented with the hot gas, $\beta = 0^\circ$, as depicted in Fig. 1.3(a). The extreme case of $\alpha = 90^\circ$ is commonly referred to as a jet-in-crossflow scenario and has been studied by e.g. Bagheri et al. (2009); Cortelezzi & Karagozian (2001); Fric & Roshko (1994); Ziefle & Kleiser (2009). Downstream of a hole, this simple-angle injection establishes a pair of counter-rotating vortices, termed kidney vortex pair, through the interaction with the hot oncoming gas. The rotational direction of the two vortices, indicated

in Fig. 1.3(b), introduces two effects which are detrimental for the cooling effectiveness. First, the vortices feed hot gas towards the blade surface and underneath themselves. Second, the mutually induced velocities point away from the surface to be cooled. This favors the lift-off of the coolant jet, cf. Haven et al. (1997). Several experimental investigations are available for single-row, simple-angle arrangements, e.g. Lee et al. (1994); Leylek & Zerkle (1994); Pietrzyk et al. (1989); Sinha et al. (1991*a,b*).

There are three basic approaches to improve the cooling effectiveness. They might be combined but their beneficial effect does not add up necessarily. First, the cooling hole is additionally yawed in the spanwise direction by angles $\beta \neq 0^\circ$, resulting in a so-called compound-angle injection, which is depicted twice in Figs. 1.3(d) to 1.3(f). Downstream of each hole, only one principal vortex is left and the other vortex from the pair is degenerated, cf. Aga et al. (2008); Lee et al. (1997). This improves the cooling effectiveness at the price of a higher heat transfer coefficient.

Second, besides cylindrical holes, diffuser-like shaped holes, in particular fan-shaped holes, are widely used. Following Bunker (2005), shaped holes can be subdivided into four types. Fan-shaped holes with a symmetric spanwise expansion of the hole, laid-back holes with an asymmetric expansion in the direction of the hot gas, laid-back fan-shaped holes and conical holes with symmetric expansion in both the spanwise and the streamwise direction. Their main benefit is a reduction of the effective coolant momentum ratio, allowing for an attached film even for high-momentum coolant. Apparently, the improved cooling properties offset the more expensive manufacturing process.

Interestingly, Barthet & Bario (2001) found an additional vortex pair, termed anti-kidney vortex pair in a fan-shaped film-cooling flow ($\beta = 0$). It exhibits a reversed rotational direction compared to a kidney vortex pair and attenuates the jet lift-off. Moreover, Haven & Kurosaka (1997) found that an anti-kidney vortex pair appears for hole exits with a wide aspect ratio and reported a reduced tendency of the jet to lift-off in such cases. This might be a subordinate reason for the improved effectiveness of fan-shaped holes.

Sargison et al. (2002) propose a row of holes with a cylindrical opening and an exit which closely resembles a continuous slot in the spanwise direction. This configuration is promising, since the continuous-slot film-cooling is superior to the discrete hole cooling. The structural strength of the blades might be reduced, however, because of the quasi-continuous

slot at the blade surface.

Third, the interaction of multiple, closely-spaced holes can be beneficial to the cooling effectiveness. Either multiple rows, arranged from in-line to staggered by Jubran & Brown (1985); Jubran & Maitech (1999), or arrays of holes are employed by Dhungel et al. (2009); Farhadi-Azar et al. (2011); Heidmann & Ekkad (2008); Yao & Maldi (2011). The interaction of the holes modifies the dominant vortices or improves the spanwise coverage of the coolant.

Figures 1.3(d) to 1.3(f) depict two subsequent rows with row-wise alternating yaw angles, also referred to as double-jet configuration. Using this arrangement allows the creation of a counter-rotating vortex pair with a reversed rotational direction, termed anti-kidney vortex pair. Thereby, the detrimental velocity induction away from the blade is reversed into a beneficial induction towards the blade. Moreover, the detrimental suction of hot gas underneath the vortex pair is reversed into a beneficial spanwise spreading of coolant. Consequently, this vortex pair enhances the film-cooling effectiveness as shown by a simulation by Kusterer et al. (2007) and an experiment by Ahn et al. (2003). Therefore, we chose Ahn et al. (2003) as our reference case L0 on which we focus.

Table 1.1 lists a selection of experiments on different film-cooling types at conditions similar to those of our anti-kidney vortex pair reference case L0, i.e. inclination angle $\alpha = 35^\circ$, mass-flux-ratio $M \approx 1$, density ratio $DR \approx 1$. Figure 1.4 compares their mean effectiveness $\langle \eta \rangle_t$ plotted against the streamwise distance non-dimensionalized by the mass-flux ratio M and the equivalent slot width $s = \pi / (4 \langle P \rangle_{x,z})$, motivated by Bogard & Thole (2006, Fig. 5). $\langle P \rangle_{x,z}$ represents the spanwise pitch, averaged over all rows).

The effectiveness, defined more rigorously in Sec. 2.5.1, is zero for no cooling and unity for perfect cooling.

The maximum effectiveness of cases L1 and L3, using a single-row, simple-angle injection with cylindrical holes, does not reach the maximum effectiveness of case L0. Also, the spanwise-averaged effectiveness is much lower for case L5 with double-row, simple-angle injection. Introducing a yaw angle as in the single- and double-row cases L6 and L4, considerably increases both the maximum and the spanwise-averaged effectiveness, however, without catching up with the double-row, alternating yaw-angle case L0. Only the maximum effectiveness of the simple-angle, fan-shaped holes of case L2 exceeds that of our anti-kidney reference case L0.

Table 1.1: Parameters of experiments using different types of film cooling at similar conditions.

Symbol, case	shape	β	L/d	P/d	S/d	Ref.
■ L0	cyl.	$\pm 45^\circ$	4	6	4	Ahn et al. (2003)
● L1	cyl.	0°	3.5	3	0	Sinha et al. (1991a)
◆ L2	fan	0°	5.2	3	0	Goldstein et al. (1974)
▲ L3	cyl.	0°	5.2	3	0	Goldstein et al. (1974)
▼ L4	cyl.	45°	6.3	3	0	Goldstein & Jin (2001)
⊙ L5	cyl.	0°	6.3	6	4	Ligrani et al. (1994)
◆ L6	cyl.	50.5°	6.3	6	4	Ligrani et al. (1994)

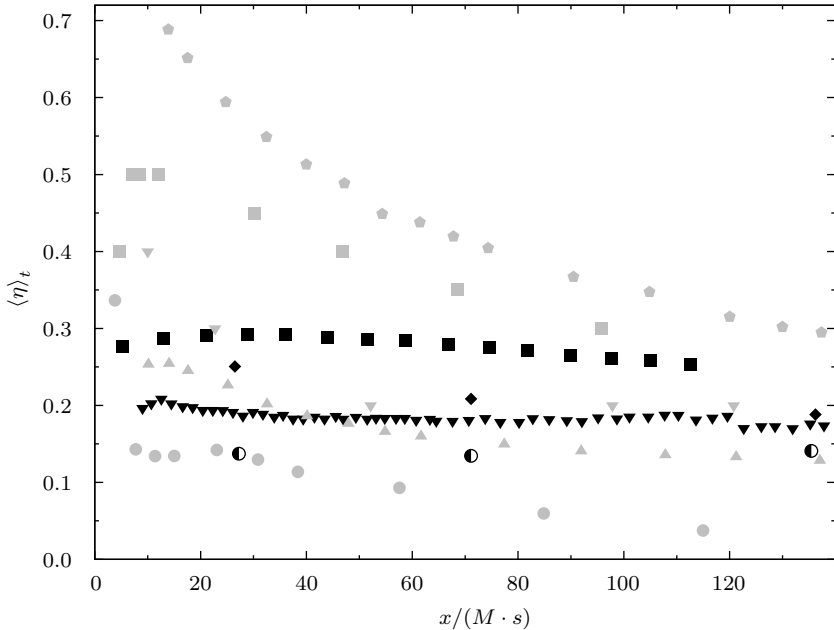


Figure 1.4: Comparison of experimental results on film-cooling types listed in Tab. 1.1. Black: spanwise-averaged effectiveness $\langle \eta \rangle_{t,z}$; gray: maximum effectiveness $\max_z \langle \eta \rangle_t$.

Measurements on a flat plate at standard conditions show that the anti-kidney vortex pair of case L0 is able to provide a higher spanwise-averaged mean effectiveness than the kidney vortex pair of case L5, Fig. 1.4.

1.3 Simulations of film cooling

Most of the literature discussed so far concerns experimental studies. However, there are also a number of simulations available. The papers referred to in Mendez & Nicoud (2008, Tab. 2) and (Renze et al., 2008, Sec. 1) can be subdivided into three groups. Most simulations, as those by Guo et al. (2006); Renze et al. (2008); Tyagi (2003); Walters & Lylek (2000); Ziefle & Kleiser (2008), deal with simple-angle film-cooling ($\beta = 0^\circ$), while some, as those by Burdet et al. (2007); McGovern & Lylek (2000), study the effect of the compound angle ($\beta \neq 0^\circ$) and some others, as those by Hyams & Lylek (2000); Kanani et al. (2008); Renze et al. (2007), consider non-cylindrically shaped hole exits. Further work has focused on the interactions of multiple closely spaced holes, as those by Heidmann & Ekkad (2008); Javadi et al. (2007); Kusterer et al. (2007).

Computational studies of film-cooling flows use either the Reynolds-Averaged Navier-Stokes (RANS) equations or Large-Eddy Simulations (LES), cf. the overviews in Mendez & Nicoud (2008, Tab. 2) and Renze et al. (2008, Sec. 1). RANS simulations have the advantage of comparably low computational expense and allow for parameters close to reality, e.g. high Reynolds number and realistic three-dimensional geometries. However, this approach is less general than LES, since it usually requires some special tuning to the considered flow case, as done e.g. in Burdet et al. (2007). In addition, standard RANS simulations provide time-averaged data and are, therefore, incapable of capturing time-dependent phenomena, like vortex breakup or periodically detaching flow structures. The breakup, however, is assumed to influence the mixture of coolant and hot gas, as noted in Ziefle & Kleiser (2008).

Today, several LES of simple-angle film cooling are available, e.g. those by Guo et al. (2006); Peet (2006); Renze et al. (2008); Tyagi (2003); Ziefle & Kleiser (2008), while fewer LES focus on shaped holes, e.g. the one by Renze et al. (2007), or multiple rows, e.g. the one by Renze et al. (2009).

1.4 Objectives and outline

As detailed in Sec. 1.2, the cooling effectiveness obtained by the anti-kidney case L0 nearly reaches that of the fan-shaped hole case L5. The relatively lower manufacturing costs of the cylindrical hole shape renders it worthwhile to investigate this special type of film cooling. We will show in Sec. 5.3.1 that the anti-kidney vortex configuration locally may obtain a higher cooling effectiveness under realistic conditions than fan-shaped cooling.

The questions arise why an additional study and why a numerical study for such a case are important. First, Ahn et al. (2003) did not present results on the flow in the plenum, located inside the blade, or in the holes. In addition, they did not show data which explain the vortex pair's subsequent assembling by the individual rows. Also, the effect of a realistic density ratio on the cooling may be interesting.

Second, numerical simulations have the advantage of providing access to all physical flow properties of interest simultaneously and usually allow a higher spatial resolution than experiments. For LES, the identification and the life-cycle of vortical structures is easier to obtain than in experimental investigations. Simulation parameters such as the temperature level can simply be set to realistic values. For experiments, this may require a totally different setup including blower, heater, and measuring devices. Furthermore, the measuring devices used in experiments may have an (although small) effect on the flow and a limited measuring range. Moreover, we are presently not aware of previous LES of anti-kidney vortex pair film-cooling using double-row alternating yaw angles.

Finally, we want to demonstrate the applicability of the Approximate-Deconvolution Model (ADM) to flows in more general geometries. ADM has been proposed at our institute by Stolz & Adams (1999). Thereafter, this sub-grid scale model was used in a series of projects showing good results for a variety of numerical discretization schemes and flow scenarios. The thesis of Stolz (2000) dealt with an incompressible channel flow computed with a spectral code as well as a shock–boundary-layer interaction using Finite-Differences. Von Kaenel (2003) adapted ADM for the Finite-Volume context, implemented it in the compressible code NSMB, and simulated a compressible channel flow as well as a shock–boundary-layer interaction. Schlatter (2005) obtained results for an incompressible channel flow and homogeneous, isotropic turbulence using spectral methods. He proposed a simplification to ADM reducing it to a relaxation

term, only. Müller (2007) and Keiderling (2008) simulated the breakup of swirling jet flows and the noise emission of non-swirling jets, respectively, using a compressible Finite-Difference code. The NSMB code was also used by Zieffe (2008) to simulate a periodic hill channel, a generic jet-in-crossflow, and a simple film-cooling scenario. He also parallelized the implementation of ADM in NSMB for multi-block grids. More recently, Henniger (2011) wrote an incompressible Finite-Difference code for massively parallel computers and simulated particle transport in estuaries.

The present work also uses the compressible Finite-Volume code NSMB. We validate our setup with a turbulent flat-plate boundary layer and simulate film-cooling flows using two interacting coolant jets, including the coolant plenum and the holes. The performed LES are at the limit of the computational resources available to us, although we optimized the parallel ADM implementation. Direct Numerical Simulations (DNS) of such flows are impossible to conduct for us, as they require even finer grids, smaller timesteps, and, therefore, much more computational time.

The thesis is structured as follows: Chapter 2 presents the simulation methods including the governing equations, discretization method, turbulence modeling, and boundary treatment in Secs. 2.1 to 2.4, respectively. Section 2.5 introduces the methods used for postprocessing the simulation data. Then, Chap. 3 validates the chosen simulation setup using a turbulent flat-plate boundary-layer flow without coolant ejection. We obtain results in good agreement with DNS, established laws, and experimental data.

The reference case L0 for film cooling is discussed in Chap. 4. We show that results of our LES compare well with the reference experiment. Then, the simulated flow is analyzed in detail, beginning in the plenum through the holes up to the mixture with the hot boundary layer. The flow regions, i.e. coolant plenum, holes, and boundary layer, are studied subsequently and linked to each other. To track the anti-kidney vortex pair throughout the boundary layer, we propose and apply two novel criteria. This enables us to associate the jet vortices with the cooling effectiveness at the plate, which is the key feature of film cooling. Furthermore, the instantaneous flow is studied.

Chapter 5 approaches realistic flow parameters by varying the blowing conditions and the yaw angle. First, the mass-flux and the temperature of the coolant are increased in Sec. 5.2. Second, Sec. 5.3 presents the flow for three different yaw angles to optimize the spanwise spreading of the coolant. For each variation, the impact on the achieved

cooling is explained in Secs. 5.2.1 and 5.3.1 and the generated losses are studied in Secs. 5.2.2 and 5.3.2. We try to isolate the driving physical mechanisms in different regions of the flow.

Remark: Previous publications related to the present work are listed at the end of this thesis.

Chapter 2

Methods

Gas consists of discrete molecules formed by atoms which in turn are composed by smaller and smaller elements. Density ρ , temperature T , pressure p , and dynamic viscosity μ define integral measures of molecules contained in some volume. Already the consideration of the individual molecules is infeasible due to their mere number of around $2.7 \cdot 10^{22}$ per liter in case of a perfect gas subject to standard conditions. Therefore, continuum mechanics considers the discrete molecules as a continuous medium, requiring that the interaction between an individual molecule and a sufficiently high number of molecules dominates the motion of the individual molecule, cf. Hirsch (1988). This requirement is fulfilled, since the present study deals with air or burnt-gas flows whose temperature roughly range from 290 to 1500 K, whose speed is sub-sonic, whose pressure is close to atmospheric conditions and whose characteristic lengthscale is on the order of millimeters. The flows considered in this study even satisfy the conditions of a Newtonian fluid, which also is the case for most engineering fluids. The flow should be considered as compressible due to average peak velocities in the holes above $2U_\infty$, cf. Fig. 4.10(m), at a boundary layer Mach number of $Ma_\infty = 0.2$.

2.1 Governing equations

The motion of Newtonian fluids is described by equations which conserve mass, momentum, and energy, together referred to as Navier-Stokes equations. An equation for the conservation of a concentration c is added here to trace the coolant fluid. This concentration does not feed back to the Navier-Stokes equations, and accordingly c is referred to as passive scalar. The governing equations in a condensed, integral form, cf. Hirsch (2007), for a volume Ω bounded by a surface S with an outward-pointing normal vector \vec{n}_S read

$$\frac{\partial}{\partial t} \int_{\Omega} \underline{U} dV = \oint_S \left(-\vec{F}_{\text{adv}} + \vec{F}_{\text{diff}} \right) \cdot \vec{n}_S dA \quad , \quad (2.1)$$

using the state vector in conservative variables \underline{U} with the three-dimensional velocity vector $\vec{u} = [u \ v \ w]^T$

$$\underline{U} = [\rho \ \rho\vec{u} \ \rho E \ \rho c]^T \quad . \quad (2.2)$$

The applied notation denotes three-dimensional geometrical vectors by arrows, tensors by bold characters, and non-geometrical vectors by underlines.

For compressible flows, the advective \vec{F}_{adv} and the diffusive flux vector \vec{F}_{diff} follow as

$$\vec{F}_{\text{adv}} = \begin{bmatrix} \rho\vec{u} \\ \rho\vec{u} \otimes \vec{u} + p\mathbf{I} \\ \vec{u}(\rho E + p) \\ \rho c\vec{u} \end{bmatrix} \quad \text{and} \quad \vec{F}_{\text{diff}} = \begin{bmatrix} \vec{0} \\ \boldsymbol{\tau} \\ \boldsymbol{\tau} \cdot \vec{u} + k\vec{\nabla}T \\ \rho D\vec{\nabla}c \end{bmatrix} \quad , \quad (2.3)$$

respectively, using the shear-stress tensor $\boldsymbol{\tau}$ and applying the Einstein summation convention

$$\boldsymbol{\tau} = \tau_{ij} = \mu \cdot (\partial u_i / \partial x_j + \partial u_j / \partial x_i - 2/3 \delta_{ij} \partial u_i / \partial x_i) \quad . \quad (2.4)$$

For the splitting, the pressure term of the momentum equations $p\mathbf{I}$ is interpreted as an advection in each spatial direction. The fluxes \vec{F} are, strictly speaking, vectors $\vec{F} = [\underline{F}_x \ \underline{F}_y \ \underline{F}_z]^T$ containing lists $\underline{F} = [f_\rho \ f_{\rho u} \ f_{\rho v} \ f_{\rho w} \ f_{\rho E} \ f_{\rho c}]^T$. As an example, the flux vectors of the momentum equation in the x -direction expand to

$$\vec{f}_{\text{adv},\rho u} = \begin{bmatrix} \rho u^2 + p \\ \rho u v \\ \rho u w \end{bmatrix} \quad \text{and} \quad \vec{f}_{\text{diff},\rho u} = \mu \begin{bmatrix} \frac{4}{3} \frac{\partial u}{\partial x} - \frac{2}{3} \frac{\partial v}{\partial y} - \frac{2}{3} \frac{\partial w}{\partial z} \\ \frac{\partial v}{\partial x} + \frac{\partial u}{\partial y} \\ \frac{\partial w}{\partial x} + \frac{\partial u}{\partial z} \end{bmatrix} \quad . \quad (2.5)$$

In the formulation of the diffusive term, Fourier's law of heat conduction $\vec{q} = k\vec{\nabla}T$ as well as Fick's law of molecular diffusion are employed and the thermal conductivity k as well as the coolant diffusion rate D are assumed to be known constants.

So far, the six equations contain nine unknowns (ρ , \vec{u} , E , c , p , T , μ). First, a power law, see Coleman et al. (1995), relates the dynamic viscosity to the temperature

$$\mu = \mu_\infty \left(\frac{T}{T_\infty} \right)^{0.7} . \quad (2.6)$$

Second, the gas is considered ideal and the associated law links pressure, density and temperature using the universal gas constant R

$$p = \rho RT . \quad (2.7)$$

The assumption of ideal gas is exact for $p \rightarrow 0$ and considered acceptable up to $p = 10^6$ Pa, Baehr & Kabelac (2009, Sec. 1.4.5). This contains the pressure found in turbine stages of approximately 3 to $9 \cdot 10^5$ Pa according to Soares (2007, Fig. 1-8).

Finally, the missing third condition is given by the total energy which can be expressed by the velocities and temperature. In addition, the gas is assumed to be perfect and using the ratio of specific heats for a diatomic gas $\gamma = 1.4$ yields

$$E = \frac{R}{\gamma - 1} T + \frac{\vec{u} \cdot \vec{u}}{2} . \quad (2.8)$$

Introducing the dimensionless Reynolds $Re_{\infty,d}$, Mach Ma_∞ , Prandtl Pr_∞ as well as Schmidt number Sc_∞ and non-dimensionalization by the cooling hole diameter d , the free-stream density ρ_∞ , velocity U_∞ as well as temperature T_∞ (and the coolant concentration c_c) yields:

$$\begin{aligned} Re_{\infty,d} = \frac{U_\infty d \rho_\infty}{\mu_\infty} &\rightarrow \mu_\infty = \frac{1}{Re_{\infty,d}} , \\ Ma_\infty = \frac{U_\infty}{\sqrt{\gamma RT_\infty}} &\rightarrow R = \frac{1}{\gamma Ma_\infty^2} , \\ Pr_\infty = \frac{\mu_\infty \gamma R}{k \cdot (\gamma - 1)} &\rightarrow k = \frac{1}{(\gamma - 1) Ma_\infty^2 Re_{\infty,d} Pr_\infty} , \\ Sc_\infty = \frac{\mu_\infty}{\rho_\infty D} &\rightarrow D = \frac{1}{Re_{\infty,d} Sc_\infty} , \\ p_\infty = \rho_\infty RT_\infty &\rightarrow p_\infty = \frac{1}{\gamma Ma_\infty^2} . \end{aligned} \quad (2.9)$$

As customary, a Prandtl number, denoting the ratio of momentum and heat diffusivity, of $Pr_\infty = 0.7$ is chosen. The Schmidt number is defined analogously to be the ratio of momentum and mass diffusivity.

The heat–mass analogy is often used in film-cooling experiments with a large density ratio between coolant and freestream, e.g. Pedersen et al. (1977). This analogy is considered valid for a unit Lewis number $Le_\infty = Pr_\infty/Sc_\infty = 1$. We choose a Schmidt number $Sc_\infty = 0.7$ to test the heat–mass analogy for the studied cases.

2.2 Finite-Volume discretization

The computational domain is discretized by cells that are arranged in a locally (on block level) structured grid to enable higher-order numerical approximations. Multiple blocks containing the cells are introduced to exploit parallel computers. The block-grid, however, is unstructured to enable for the complex geometry as necessary in film-cooling. Two layers of ghost cells surround each block surface containing either the data of adjacent blocks or data to enforce boundary conditions.

Averaging Eq. (2.1) over fixed cells i, j, k arranged in a structured grid and being hexahedra $\Omega_{i,j,k}$ bounded by six quadrilateral sides $s = 1 \dots 6$ enclosing areas A_s yields

$$\frac{\partial}{\partial t} U_{i,j,k} = \frac{1}{V_{i,j,k}} \underbrace{\sum_{s=1}^6 \left(-\vec{F}_{\text{adv}} \Big|_s + \vec{F}_{\text{diff}} \Big|_s \right)_{i,j,k}}_{= \underline{F}_{\text{NS},i,j,k}} \cdot \overbrace{(\vec{n}_s A_s)_{i,j,k}}^{= \vec{A}_{i,j,k,s}}, \quad (2.10)$$

using the cell-averaged state vector

$$\underline{U}_{i,j,k} = \frac{1}{V_{i,j,k}} \int_{\Omega_{i,j,k}} \underline{U} dV \quad . \quad (2.11)$$

A second-order error is introduced by assuming the cell-average to be located at the cell-center $\vec{x}_{i,j,k}$ for postprocessing, Hirsch (2007, Sec. 11.4.1). The location of the cell center $\vec{x}_{i,j,k}$ is calculated as the arithmetic mean of the locations of the eight cell corners given by the grid, e.g. $\vec{x}_{i-\frac{1}{2},j-\frac{1}{2},k-\frac{1}{2}}$. Likewise, the location of the surface centers, e.g. $\vec{x}_{i-\frac{1}{2},j,k}$, follow from the four surface corners. The side indices $s = 1 \dots 6$

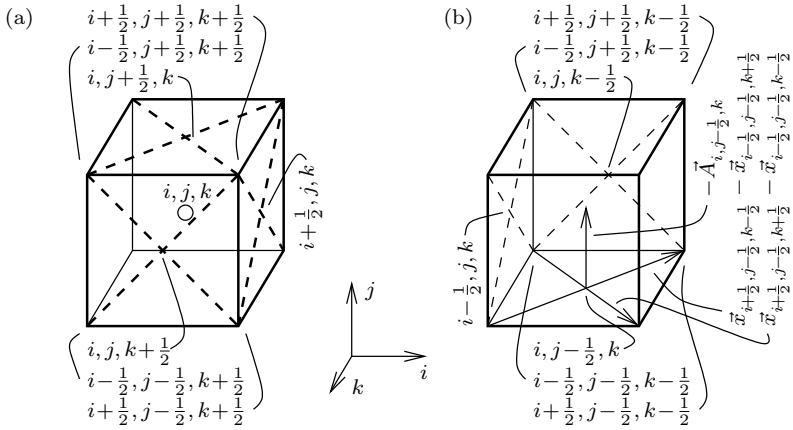


Figure 2.1: Schematic of the index notation of a Finite-Volume cell. (a), (—): visible; (b), (---): invisible parts.

correspond to the index locations $(i - \frac{1}{2}, j, k)$, $(i + \frac{1}{2}, j, k)$, $(i, j - \frac{1}{2}, k)$, $(i, j + \frac{1}{2}, k)$, $(i, j, k - \frac{1}{2})$, $(i, j, k + \frac{1}{2})$, respectively, cf. Fig. 2.1.

The cell surface is computed as the half crossproduct of the diagonals. The length of the resulting vector $-\vec{A}_s$ corresponds to the surface area and points inside the cell, e.g.

$$\begin{aligned}
 -\vec{A}_{i,j-\frac{1}{2},k} &= \frac{1}{2} \left(\vec{x}_{i+\frac{1}{2},j-\frac{1}{2},k+\frac{1}{2}} - \vec{x}_{i-\frac{1}{2},j-\frac{1}{2},k-\frac{1}{2}} \right) \\
 &\quad \times \left(\vec{x}_{i+\frac{1}{2},j-\frac{1}{2},k-\frac{1}{2}} - \vec{x}_{i-\frac{1}{2},j-\frac{1}{2},k+\frac{1}{2}} \right) .
 \end{aligned} \tag{2.12}$$

The cell volume is separately approximated in each index direction by the sum of the scalar products of surface area-vector and surface-center position-vector from opposing surfaces. Then, the approximations are arithmetically averaged

$$V_{i,j,k} = \frac{1}{3} \sum_{s=1}^6 \vec{x}_{i,j,k,s} \cdot \vec{A}_{i,j,k,s} . \tag{2.13}$$

2.2.1 Advective flux approximation

The advective fluxes are approximated by four different, explicit, centered, Finite-Difference-style schemes with up to fourth-order accuracy.

The schemes are adaptations from the one-dimensional case by direction splitting of each flux due to u , v and w .

The non-linear term of the momentum equation and the whole energy equation employ the fourth-order accurate, skew-symmetric scheme of Ducros et al. (2000, Eq. 29). For example, the flux at $i+\frac{1}{2}, j, k$ for ρv due to w is approximated as

$$\begin{aligned}
 f_{\rho v, w, i+\frac{1}{2}, j, k} = & \frac{1}{3} \left((\rho v)_{i, j, k} + (\rho v)_{i+1, j, k} \right) \cdot \left(w_{i, j, k} + w_{i+1, j, k} \right) \\
 & - \frac{1}{24} \left((\rho v)_{i-1, j, k} w_{i-1, j, k} + (\rho v)_{i-1, j, k} w_{i+1, j, k} \right. \\
 & \quad + (\rho v)_{i, j, k} w_{i, j, k} + (\rho v)_{i, j, k} w_{i+2, j, k} \quad (2.14) \\
 & \quad + (\rho v)_{i+1, j, k} w_{i+1, j, k} + (\rho v)_{i+1, j, k} w_{i-1, j, k} \\
 & \quad + (\rho v)_{i+2, j, k} w_{i, j, k} + (\rho v)_{i+2, j, k} w_{i, j, k} \\
 & \quad \left. + (\rho v)_{i+2, j, k} w_{i+2, j, k} \right).
 \end{aligned}$$

The mass conservation equation and the pressure term of the momentum equation use the divergence form of the fourth-order accurate scheme of Ducros et al. (2000, Eq. 27). For example, the flux at $i+\frac{1}{2}, j, k$ for ρ due to u is approximated as

$$\begin{aligned}
 f_{\rho, u, i+\frac{1}{2}, j, k} = & \frac{1}{12} \left(-\rho_{i+2, j, k} u_{i+2, j, k} + 7\rho_{i+1, j, k} u_{i+1, j, k} \right. \\
 & \left. -\rho_{i-1, j, k} u_{i-1, j, k} + 7\rho_{i, j, k} u_{i, j, k} \right). \quad (2.15)
 \end{aligned}$$

The accuracy is reduced to second order at walls as well as at in- and outflow boundaries. There, the skew-symmetrically approximated terms use the same approximation as the passive scalar in the whole field. For example, the flux at $i+\frac{1}{2}, j, k$ for ρv due to w is approximated as

$$\begin{aligned}
 f_{\rho v, w, i+\frac{1}{2}, j, k} = & \\
 & \frac{1}{2} \left((\rho v)_{i, j, k} + (\rho v)_{i+1, j, k} \right) \frac{(\rho w)_{i, j, k} + (\rho w)_{i+1, j, k}}{\rho_{i, j, k} + \rho_{i+1, j, k}}. \quad (2.16)
 \end{aligned}$$

This approximation is equivalent to the skew-symmetric form by Ducros et al. (2000, Eq. 21) if $\rho_i = \rho_{i+1}$, i.e. at adiabatic walls. The terms are approximated in divergence form and reduce their accuracy order following Ducros et al. (2000, Eq. 20), i.e.

$$f_{\rho, u, i+\frac{1}{2}, j, k} = \frac{1}{2} \left(\rho_{i, j, k} u_{i, j, k} + \rho_{i+1, j, k} u_{i+1, j, k} \right). \quad (2.17)$$

2.2.2 Diffusive flux approximation

The averaged gradients of velocity $\vec{\nabla}\vec{u}$, temperature $\vec{\nabla}T$ and concentration $\vec{\nabla}c$ at the cell surfaces are required to compute the diffusive fluxes \vec{F}_{diff} . Three grids, each staggered in one spatial direction, are used to determine the gradients at all six surfaces of the cells. The gradients are evaluated using Stokes' theorem on the staggered grid Peyret & Taylor (1983, Sec. 7.3). For example, the gradient at $i-\frac{1}{2}, j, k$ of \vec{u} is evaluated as

$$\vec{\nabla}\vec{u}_{i-\frac{1}{2},j,k} = \frac{1}{V_{i-\frac{1}{2},j,k}} \sum_{s,s=1}^6 \vec{u}_{i-\frac{1}{2},j,k} \Big|_{s,s} A_{s,s} \quad . \quad (2.18)$$

Here, the side indices $s_s = 1 \dots 6$ correspond to $(i-1, j, k)$, (i, j, k) , $(i-\frac{1}{2}, j-\frac{1}{2}, k)$, $(i-\frac{1}{2}, j+\frac{1}{2}, k)$, $(i-\frac{1}{2}, j, k-\frac{1}{2})$, $(i-\frac{1}{2}, j, k+\frac{1}{2})$, respectively. The surface and the volume of the staggered cell is assumed to be the average of the closest surfaces and volumes, respectively, e.g.

$$V_{i-\frac{1}{2},j,k} = \frac{1}{2} \left(V_{i-1,j,k} + V_{i,j,k} \right) \quad ,$$

$$A_{i,j,k} = \frac{1}{2} \left(A_{i-\frac{1}{2},j,k} + A_{i+\frac{1}{2},j,k} \right) \quad .$$

At the boundaries, these properties are copied from the first interior cells.

The values at the surface centers of a staggered grid are assumed equivalent to the values at the cell centers of the original grid for two surfaces, i.e. $s_s = 1, 2$ cf. Figs. 2.2(a) and 2.2(b). Each of the remaining four surface values, i.e. $s_s = 3 \dots 6$ cf. Fig. 2.2(c), is interpolated as the arithmetic mean from the known values at their four surrounding cell centers of the original grid.

Only at block edges or block corners, one or two values, respectively, are not known to the block since they reside neither inside the block nor in the ghost layers but in the ghost edges, cf. Fig. 2.2(a). In structured block-grid areas, these unknown ghost-edge values can be copied from the diagonally opposing block for the cost of diagonal communication. However, this is not done since the communication overhead caused by a large number of communication events with a small amount of data would reduce the performance of the whole simulation. In addition, for unstructured zones, e.g. O-grids, the ghost edge value is ambiguous and, therefore, is extrapolated. Analogously, for the case of two in- and outflow boundary conditions touching the same block edge, the

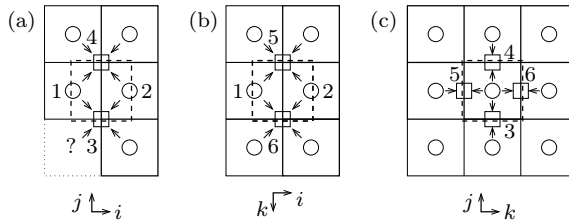


Figure 2.2: Evaluation of surface center values of a staggered grid near block edges. (—): interior cell; (—): ghost-layer cell; (- - -): staggered cell; (.....): ghost-edge cell; \circ : known value; \square : interpolated value; $?$: unknown value; $1 \dots 6$: surface index s_s of staggered cell.

unknown value is extrapolated. The extrapolation is done by setting the unknown value at the surface of the staggered cell equal to the known value at the center of the staggered cell. At the walls, however, the ghost edge is unambiguous and is obtained from the no-slip condition.

2.2.3 Time integration and computer code

The state vector \underline{U}^n from timestep n is advanced to \underline{U}^{n+1} by a time period Δt using an explicit scheme. A four-step $l = 1 \dots 4$ low-storage Runge-Kutta scheme is chosen, which requires only one additional field $\underline{U}_{i,j,k}^n$ to be stored

$$\underline{U}_{i,j,k}^{n+l/4} = \underline{U}_{i,j,k}^n + \frac{1}{5-l} \frac{\Delta t}{V_{i,j,k}} \underline{F}_{\text{NS},i,j,k} \left(\underline{U}_{i,j,k}^{n+(l-1)/4} \right) \quad . \quad (2.19)$$

This scheme is of second-order accuracy for non-linear equations Swanson & Turkel (1997, p. 35). The computation of the time-step limit is documented in von Kaenel (2003, Sec. 2.5).

The Navier-Stokes multi-block (NSMB) code is used for all simulations presented in this work, cf. Vos et al. (1997). This MPI-parallelized code has been developed by a mixed industrial-academic, European consortium. Many of the core routines are optimized for vector supercomputers thus offering high peak performance. In the course of this project, version 5.60 of NSMB was adjusted and new features were added.

NSMB subdivides the boundary conditions introduced in Sec. 2.4 into internal and external boundary conditions. Internal boundary conditions do not require communication with other blocks, i.e. inflow,

outflow, wall, periodicity within the block. External boundaries, in contrast, require communication with (periodically) adjacent blocks, i.e. block connectivity or periodicity using two blocks. This communication is done by first copying the values of the outer two layers of field-cells to a buffer, communicating them via MPI and successively copying to the ghost-layers of another block.

2.3 Turbulence modeling

Film-cooling flows in gas turbines are turbulent. Turbulent flows contain very small eddies (with an associated frequency $f \leq f_k$) relative to the considered characteristic length, i.e. d or the boundary layer thickness. This requires very fine grids for the computation of such flows which, in turn, reduces the timestep of the whole simulation. This requirement is a shortcoming of DNS limiting their application to small computational domains at given bounded computational resources.

Following Sagaut (2006, Sec. 1.4), there are four basic ways to model turbulent flows in order to avoid the strong computational requirements. RANS, Unsteady RANS (URANS), basis functions and LES. RANS does not allow to study unsteady effects but requires the least amount of computational resources. URANS comes at higher computational costs offering an unsteady solution. Still, the complete description of large eddies is not possible, since only very few frequencies are computed. Basis functions might not be suited due to the complexity of film-cooling flows.

2.3.1 LES approach: relaxation term model

We chose LES which only represent the low frequencies containing most of the energy while the high frequencies and/or small wavelengths are modeled, i.e. by a subgrid scale (SGS) model, cf. Fig. 2.3(a). The removal of the high frequencies by the grid is commonly referred to as band-pass filtering and can be represented by a convolution operation, Sagaut (2006, Sec. 2).

The Approximate-Deconvolution Model (ADM) proposed by Stolz & Adams (1999), as the name suggests, approximately reverses this removal to some extent. An explicit filter (resolved/non-resolved) with a cutoff frequency f_c lower than the cutoff frequency f_n of the implicit grid-filter (represented/non-represented) is applied to the solution. Following Stolz et al. (2001, Sec. II.), ADM models the effect of the non-resolved

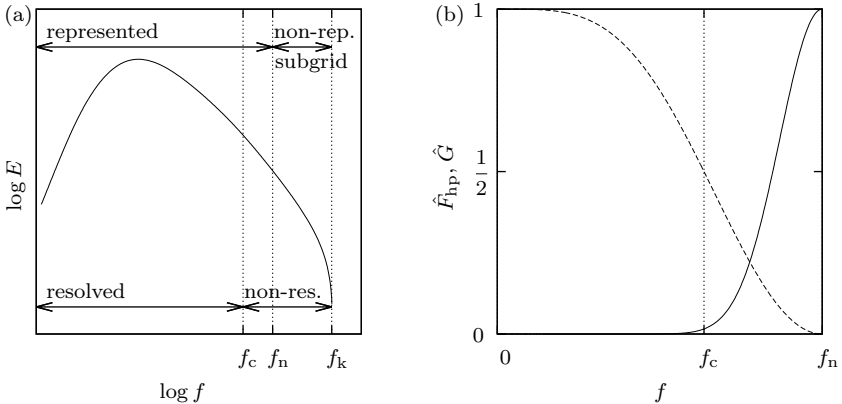


Figure 2.3: (a): Sketch of a generic energy spectrum for fully developed turbulent flows with frequencies using the terminology of Stolz et al. (2001). (b): Transfer function of (—): the high-pass filter \hat{F}_{hp} using the (---): centered, five-point primary filter \hat{G} for one dimensional uniform grids.

frequencies $f \geq f_c$ on the resolved frequencies $f < f_c$ by the represented, non-resolved frequencies $f_c < f \leq f_n$, Fig. 2.3(a). This requires the use of the approximately deconvolved state vector for the computation of the fluxes and the successive filtering of the fluxes themselves. In addition, a dissipative relaxation term is subtracted to model the drain of energy from represented to non-represented frequencies. Further details on ADM are found in Stolz et al. (2001) and Sagaut (2006, Sec. 7.2.1); an adaptation to Finite-Volume schemes is given by von Kaenel et al. (2003). ADM was implemented into NSMB by von Kaenel, parallelized for the use of multiple blocks by Ziefle, and optimized for high performance on vector supercomputers in the course of this project.

Schlatter et al. (2004, RT-3D) obtained satisfactory results without explicit filtering or deconvolution of the Navier-Stokes terms. Following this approach, only the relaxation term is subtracted from the right hand side of the discrete governing equations Eq. (2.10)

$$\frac{\partial}{\partial t} \underline{U}_{i,j,k} = \frac{1}{V_{i,j,k}} \left(\underline{F}_{\text{NS}}(\underline{U}_{i,j,k}) - \chi \cdot \underline{F}_{\text{hp}}(\underline{U}_{i,j,k}) \right) . \quad (2.20)$$

In the original version of ADM, the relaxation coefficient χ is automatically determined between two predefined bounds. The upper bound is $\chi \leq 1/\Delta t$ and ensures stable integration using an Euler forward scheme,

following Stolz et al. (2001, Sec. III). The lower bound is $\chi > 0$ and ensures a purely dissipative relaxation term.

In the present work, however, the coefficient is chosen to be constant and uniform since Ziefle & Kleiser (2009) obtained valid results for a jet-in-crossflow scenario using this simplification. The upper bound of $\chi \leq 1/\Delta t$ is honored in all simulations, although the chosen Runge-Kutta integration scheme would allow for larger χ due to its larger stability region compared to Euler forward. We chose χ as low as possible in a trial-and-error procedure to limit the energy drained by the model. The non-dimensional value of χ is, therefore, adjusted for every simulation case, cf. Sec. 3.1.

The relaxation term consists of the high-pass filtered state vector. Stolz et al. (2001) propose an explicit filter with a stencil width of $\nu_1 + \nu_r + 1 = 5$ points and a deconvolution order of $N = 5$. The high-pass filtered field is obtained by successive application of the primary filter G_{3D} , cf. Fig. 2.3(b)

$$E_{\text{hp}}(\underline{U}_{i,j,k}) = \sum_{\nu=0}^{N+1} \beta_{\nu} \cdot \underline{G}_{3D}^{\nu}(\underline{U}_{i,j,k}) \quad (2.21)$$

using the coefficients $\beta_0 = \beta_6 = 1$, $\beta_1 = \beta_5 = -6$, $\beta_2 = \beta_4 = 15$, and $\beta_3 = -20$.

The three-dimensional primary filter G_{3D} is computed by the application of a one-dimensional filter, with the cutoff frequency f_c , for each index direction $G_{3D}(U) = G_k(G_j(G_i(U)))$. The filter is defined by e.g.

$$\underline{G}_{i,i,j,k}(\underline{U}_{i,j,k}) = \sum_{l=-\nu_1}^{\nu_r} \alpha_{i,j,k,l} \cdot \underline{U}_{i+l,j,k} \quad (2.22)$$

The coefficients α_l of the symmetric filter $\nu_1 = \nu_r = 2$ for the field are derived in Stolz (2000, Eqs. (B.3) to (B.6) and (B.9)) to minimize dispersion errors and provide a vanishing moment of second order. Different coefficients are used at the boundaries of the computational domain. The cell next to the boundary cell uses a $\nu_1 + \nu_r + 1 = 4$ point asymmetric $|\nu_1 - \nu_r| = 1$ stencil defined in Stolz (2000, Eqs. (B.17) to (B.20)) providing a filter with vanishing moment of second order. The boundary cell itself is not filtered at all, Fig. 2.4.

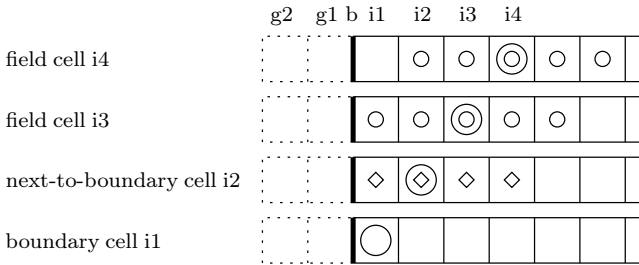


Figure 2.4: Boundary treatment of the filter. (—): Cell edge (i1, i2, ...); (---): boundary (b); (.....): ghost-cell edge (g1, g2); ○: filtered cell; ⊖: stencil elements for symmetric and ◇: asymmetric filter.

2.3.2 Turbulent inflow: Synthetic-Eddy Method

A fully turbulent flat-plate boundary layer is required for our intended simulations. Computing the laminar–turbulent transition would consume about as much time as the simulation of the film-cooling problem itself. Another, more efficient option is to employ the Synthetic-Eddy Method (SEM) by Jarrin et al. (2006) which provides a turbulent-like signal to be imposed on the inflow condition. Downstream of a relaxation length of several boundary layer thicknesses, the properties of a fully turbulent boundary layer are recovered at low computational costs.

A virtual box with a volume V_B is defined surrounding the inflow plane of the computational domain with a distance of $\max_{i,j,k}(\sigma_{i,j,k})$, Jarrin (2008, Eq. (4.2)). The SEM randomly puts synthetic eddies $l = 1 \dots N_{\text{eddy}}$ in this box and assigns random signs to them for each spatial direction $\vec{\varepsilon}_l$. These eddies are convected by the given constant, spatially-averaged velocity $\langle u \rangle_{y,z}$ at the inflow of the computational domain. After leaving the box, they are fed back in at a random position of the box inflow plane and receive new random signs. Each synthetic eddy induces a velocity according to the same shape function $f(\delta)$ which is only non-zero for $|\delta| < \sigma$. The absolute induced velocity by eddy l is the same for all spatial directions, Jarrin (2008, Eqs. (4.4) and (4.6))

$$\vec{u}_{\text{ind},i,j,k,l} = \vec{\varepsilon}_l \cdot f\left(\frac{x_{i,j,k} - x_k}{\sigma_{i,j,k}}\right) \cdot f\left(\frac{y_{i,j,k} - y_k}{\sigma_{i,j,k}}\right) \cdot f\left(\frac{z_{i,j,k} - z_k}{\sigma_{i,j,k}}\right) \quad (2.23)$$

Superimposing the induced velocities of the eddies passing by the

stationary inflow plane of the simulation domain generates a fluctuating velocity signal.

Given the Reynolds stress tensor $\mathbf{R} = R_{m,n} = \langle u'_m u'_n \rangle_{t,z}$ for the considered Reynolds number, e.g. from literature, a constant tensor $\mathbf{a} = a_{m,n}$ is computed by a Cholesky decomposition, mapping a random velocity signal with zero mean and variance of unity to the stress tensor, Jarrin (2008, Eq. (4.7))

$$\mathbf{a} = \begin{bmatrix} \sqrt{R_{11}} & 0 & 0 \\ R_{21}/a_{11} & \sqrt{R_{22} - a_{21}^2} & 0 \\ R_{31}/a_{11} & (R_{32} - a_{21} \cdot a_{31})/a_{22} & \sqrt{R_{33} - a_{31}^2 - a_{32}^2} \end{bmatrix}. \quad (2.24)$$

After mapping the induced velocities, the Reynolds stress tensor is reproduced at the position $\vec{x}_{i,j,k}$ of the inflow plane of the simulation domain. Finally the given mean velocity profile is superimposed and the synthetic turbulent inflow data adapted from Jarrin (2008, Eqs. (4.3), (4.4), and (4.6)) follows as

$$\vec{u}_{i,j,k}(t) = \langle \vec{u}_{i,j,k} \rangle_{z,t} + \sqrt{\frac{V_B}{N_{\text{eddy}} \cdot \sigma_{i,j,k}^3}} \sum_{l=1}^{N_{\text{eddy}}} \mathbf{a}_{i,j,k} \cdot \vec{u}_{\text{ind},i,j,k,l}. \quad (2.25)$$

The employed parameters are detailed in Secs. 3.1 and 3.1.1, i.e. mean velocity profile, Reynolds stresses, number of eddies, and lengthscale σ .

There is also a modification by Pamiès et al. (2009) subdividing the inflow box into multiple, wall-parallel modes. Each mode has its specific convection velocity and the eddies of different modes have different, non-isotropic shape functions as well as spatial extents. However, the Reynolds stress tensor is not perfectly reproduced at the inflow plane of the simulation domain due to the overlapping of eddies of different modes with different attributes. Nevertheless, this modified SEM provides a shorter relaxation length compared to the original version. In the current work, the original SEM is used because of the publicly available SEM-code and satisfactory relaxation length for the turbulent boundary layer obtained in Chap. 3. Additional information on the original and modified SEM are found in Jarrin (2008) and Pamiès (2008), respectively.

An adaptation of SEM to compressible flows by Magagnato et al. (2006) is used. Following Magagnato et al. (2006, Eq. (5)) and (Bradshaw, 1977, Eq. (2)), temperature fluctuations can be estimated from velocity fluctuations for subsonic flows

$$\left(\frac{T'}{\langle T \rangle_t} \right)_{i,j,k} = (1 - \gamma) \cdot Ma_\infty^2 \cdot \left(\frac{u'}{\langle u \rangle_t} \right)_{i,j,k} . \quad (2.26)$$

Following Busemann and Crocco, the mean temperature profile can be obtained from the mean velocity profile, e.g. adapted from Schlichting (1979, Eq. (13.21)),

$$\langle T \rangle_{t,i,j,k} = T_\infty + r \cdot \frac{\gamma - 1}{2 \cdot \gamma \cdot R} \left(U_\infty^2 - \langle U \rangle_{t,i,j,k}^2 \right) \quad (2.27)$$

using a recovery factor for turbulent boundary layers of $r = \sqrt[3]{Pr}$, Schlichting (1979, Eq. (23.26)). Although the Busemann-Crocco relation is derived for laminar compressible boundary layers, it represents a good approximation for turbulent cases as well, Schlichting (1979, Sec. XXXIII.b.3). Finally, the density is calculated using the ideal gas law at a given pressure, see Sec. 2.4.1.

2.4 Boundary treatment

The computational domain is chosen as small as possible to save computational resources. Putting domain boundaries in regions of intense flow activity, might cause strong modeling efforts as demonstrated in Sec. 2.3.2 or introduce major errors.

In the following, values at the domain boundaries are obtained. They are extrapolated to the first layer of ghost cells since the state vectors are located at the cell-centers and the boundaries at their surface

$$\underline{U}_{g1} = 2 \cdot \underline{U}_b - \underline{U}_{i1} . \quad (2.28)$$

(The notation of the cells and boundary is introduced in Fig. 2.4.) An exception is the periodic boundary condition which copies the values of the two inner layers of the periodically adjacent block to the ghost cells. (Boundaries between two blocks are treated likewise.) The periodic boundary condition is used in the spanwise direction assuming an infinitely wide boundary layer and infinitely long rows of equidistant cooling holes.

Adiabatic, no-slip walls are modeled by a zero wall-normal pressure gradient as also done in various simulations including film-cooling flows, von Kaenel (2003); Ziefle (2008). The implications of this modeling are discussed in Rizzi (1978) and Liu et al. (2006). Applying von Kaenel (2003, Eq. (2.41)) with a concentration, the boundary values are

$$\begin{bmatrix} \rho \\ \rho \vec{u} \\ \rho E \\ \rho c \end{bmatrix}_b = \begin{bmatrix} \rho \\ \vec{0} \\ \rho E \\ \rho c \end{bmatrix}_{i1} . \quad (2.29)$$

Dirichlet conditions for density, velocities, and concentration are applied at steady and unsteady inflow boundaries. The fifth element of the state vector, ρE , is extrapolated from the field, motivated by the following discussion of characteristics. Outflow boundaries, however, require a more involved treatment for our cases. Characteristic boundary conditions are derived from the analysis of Euler equations.

2.4.1 Characteristic boundary conditions

Five characteristics represent waves traveling at certain velocities and in particular directions. Four characteristics point outside of the computational domain for subsonic outflows and only one enters from outside (and vice versa for subsonic inflows). Waves leaving the domain are not modified while the amplitude of the wave entering the domain is set to zero to prevent reflections at least for one-dimensional waves. A more detailed discussion is found in Poinot & Lele (1992); Thompson (1987, 1990).

Characteristic, non-reflecting conditions are imposed by executing the following procedure at each boundary-cell surface. First, the conservative state vector at the boundary is extrapolated from the first and second interior cell layers $\underline{U}_b = \frac{3}{2} \cdot \underline{U}_{i1} - \frac{1}{2} \cdot \underline{U}_{i2}$. The boundary-normal differences are evaluated by $\Delta \underline{V}_b = \underline{V}_{g1} - \underline{V}_{i1}$. Then, primitive variables at the boundary \underline{V}_b and the local speed of sound a_b are computed. Next, the velocities are mapped to $[u \ v \ w]_1$ in a local coordinate system in which x_1 points outside of the field perpendicular to the boundary. This allows for the evaluation of the characteristic velocities $\lambda_1 = u_{b,1} - a_b$, $\lambda_{2..4} = u_{b,1}$ and $\lambda_5 = u_{b,1} + a_b$ as well as the variation of the amplitudes of the characteristic waves as determined by the field $L_{1..5,\text{field}}$, cf. Thompson (1990, Eq. (44) and (47))

$$\frac{L_{i,\text{field}}}{\lambda_i} \Delta x_1 = \begin{bmatrix} \Delta p - \rho \cdot a \cdot \Delta u_1 \\ a^2 \cdot \Delta \rho - \Delta p \\ \Delta v_1 \\ \Delta w_1 \\ \Delta p + \rho \cdot a \cdot \Delta u_1 \end{bmatrix}_b . \quad (2.30)$$

Incoming variations are set to zero and outgoing waves remain unaltered

$$\frac{L_i}{\lambda_i} \Delta x_1 = \begin{cases} \frac{L_{i,\text{field}}}{\lambda_i} \Delta x_1 & \text{if } \lambda_i > 0 \\ 0 & \text{else} \end{cases} . \quad (2.31)$$

The final Neumann conditions are given by solving Eq. (2.30) for the variables $\Delta u_{b,1}$, $\Delta v_{b,1}$, $\Delta w_{b,1}$, $\Delta \rho_b$, and Δp_b using L_i . After mapping back the velocities to the global system, the primitive state vector in the first ghost layer is obtained by $\underline{V}_{g1} = \Delta \underline{V}_b + \underline{V}_{i1}$.

The concentration, however is conservatively extrapolated and limited (to $0 \dots 1$) from the field in case of an outflow and kept constant in case of an inflow as

$$(\rho c)_{g1} = \begin{cases} \rho_{g1} \min \left(1, \max \left(0, \frac{2(\rho c)_{i1} - (\rho c)_{i2}}{\rho_{g1}} \right) \right) & \text{if } \lambda_2 > 0 \\ (\rho c)_{g1} & \text{else} \end{cases} . \quad (2.32)$$

2.4.2 Sponge zones

Three issues arise from this treatment of in- and outflow boundaries. First, the Dirichlet inflow condition reflects the characteristic wave which should leave the domain at the subsonic inflow unaltered. Second, non-reflective characteristic conditions have problems especially at edges and corners of the computational domain, since they are derived for one-dimensional waves. Third, the pressure may drift during the simulation since it is not fixed by the in- or outflow conditions.

These issues are handled by sponge zones, cf. e.g. Bodony (2006). Another term is added to Eq. (2.20) and the final equation reads

$$\frac{\partial}{\partial t} \underline{U}_{i,j,k} = \frac{1}{V_{i,j,k}} \left(\underline{F}_{\text{NS}}(\underline{U}_{i,j,k}) - \chi \cdot \underline{F}_{\text{hp}}(\underline{U}_{i,j,k}) - \underline{\sigma}_{i,j,k} \cdot (\underline{U}_{i,j,k} - \underline{U}_{\text{ref},i,j,k}) \right) . \quad (2.33)$$

Sponge zones drive the actual state vector \underline{U} towards a reference state $\underline{U}_{\text{ref}}$ by introducing a respective flux, instead of directly setting the state vector. $\underline{\sigma}$ controls the zones of sponge activity, the transition between sponges and inner field, the strength of the sponges, as well as the variables the sponges act on. The zones are located near in- and

outflow boundaries. The transition between them is implemented by a fifth-order polynomial that is smooth up to the second spatial derivative.

Steady inflow conditions are supplemented with sponges which act on the same variables as the boundary condition, i.e. density and velocities, to reduce reflections. No sponge is added within the boundary layer to avoid damping of the generated fluctuations of the SEM-inflow. This generates acoustic waves whose pressure fluctuations are, fortunately, small compared to those of the studied eddies. At outflow boundaries, the sponges adjust the pressure (only) to prevent a drift in the long term time-integration. To further prevent reflections, the cell spacing is stretched towards the outflow boundary of the boundary layer as detailed in Sec. 3.1.3.

2.5 Postprocessing

This section introduces to the methods used for postprocessing. For convenience, these methods are not discussed in Chap. 4 since they are used in Chap. 5 as well.

2.5.1 Cooling and loss measures

The cooling achieved in our simulations is analyzed by the non-dimensional temperature and the effectiveness following Goldstein (1971, Eq. (4))

$$\Theta = \frac{T - T_r}{T_{t,c} - T_r} \quad , \quad \eta = \Theta|_{y/d=0} = \frac{T|_{y/d=0} - T_r}{T_{t,c} - T_r} \quad . \quad (2.34)$$

The recovery temperature T_r is determined by spatial and temporal averaging of a preceding, undisturbed boundary layer LES for case 3b β and is adapted to the other cases.

The losses caused by film cooling are subdivided into aerodynamic and aerothermal influences. We use loss coefficients ξ that are zero for the case of an isentropic process and unity for complete loss with respect to the considered quantity. Aerodynamic losses are customarily indicated by the total-pressure loss. The loss related to the hot gas properties only, highlights the effects of film cooling on the flow above the plate. Adapted from Lee et al. (1997, Eq. (2)), the loss reads

$$\xi_{p,t,h} = \frac{p_{t,h} - p_{t,f}}{\rho_\infty U_\infty^2 / 2} . \quad (2.35)$$

The total-pressure loss of the coolant is included by choosing the ideal mixture of coolant and hot gas as a reference. Adapted from Aga et al. (2009, Eqs. (1), (3)), this reads

$$\xi_{p,t,mix} = \frac{\frac{\dot{m}_p}{\dot{m}_p + \dot{m}_h} p_{t,p} + \frac{\dot{m}_h}{\dot{m}_p + \dot{m}_h} p_{t,h} - p_{t,f}}{\rho_\infty U_\infty^2 / 2} . \quad (2.36)$$

Aerothermal losses are usually measured by the entropy generation. The losses due to the non-isentropic coolant flow from the plenum up to the injection at the plate surface follow from the discharge coefficient, which is adapted from Gritsch et al. (2005, Eqs. (2) to (4)) as

$$\xi_d = 1 - \frac{\dot{m}_c}{\frac{\pi}{2} d^2 p_{t,p} \left(\frac{p_c}{p_{t,p}} \right)^{\frac{\gamma+1}{2\gamma}} \sqrt{\frac{2\gamma}{(\gamma-1)R T_{t,p}} \left(\left(\frac{p_{t,p}}{p_c} \right)^{\frac{\gamma-1}{\gamma}} - 1 \right)}} . \quad (2.37)$$

(The denominator is the mass-flux of an isentropic expansion from state p to c.) The entropy generation of the whole film-cooling setup can be expressed by a film-cooling loss coefficient, which is adapted from Aga et al. (2009, Eq. (6)). It is an application of Hartsel's method, Hartsel (1972), and reads

$$\xi_{s,mix} = 1 - \frac{\dot{m}_f T_{t,f} \left(1 - \left(\frac{p_f}{p_{t,f}} \right)^{\frac{\gamma-1}{\gamma}} \right)}{\dot{m}_h T_{t,h} \left(1 - \left(\frac{p_f}{p_{t,h}} \right)^{\frac{\gamma-1}{\gamma}} \right) + \dot{m}_p T_{t,p} \left(1 - \left(\frac{p_f}{p_{t,p}} \right)^{\frac{\gamma-1}{\gamma}} \right)} . \quad (2.38)$$

2.5.2 Vortex identification

Vortex structures (also termed eddies or, simply, vortices) play an important role for this specific film-cooling arrangement. The existence of various criteria displayed in Tab. 2.1 reflects the ambiguous definition of a vortex, cf. Jeong & Hussain (1995); von Terzi et al. (2009).

The choice of number as well as origin position of the streamlines and velocity vectors substantially determines the vortex assessment. The Line-Integral Convolution introduced by Cabral & Leedom (1993) (LIC)

Table 2.1: Vortex identification criteria. Principally ordered by decreasing intuitiveness and increasing elaborateness. \mathbf{S} , $\mathbf{\Omega}$: Symmetric and anti-symmetric part of $\vec{\nabla}\vec{u}$, respectively.

2D/3D	criterion	identification
2D	Velocity vectors \vec{u}	forming closed structure
2D/3D	Streamlines	closed, helical
2D	Line-Integral Convolution, Cabral & Leedom (1993)	closed structure
2D/3D	Pressure p	lower than average
2D/3D	Pressure fluctuations $p' = p - \langle p \rangle_t$, von Terzi et al. (2009)	preferably large
2D	Normal vorticity e.g. ω_z	high magnitude
2D/3D	Vorticity magnitude $ \vec{\omega} $	high value
3D	Helicity $h := \vec{u} \cdot \vec{\omega} $	high value
3D	Normed helicity $h_0 := h / \vec{u} $	high value
3D	Kinematical vorticity number N_K , Truesdell (1954, pp. 106–111)	> 0 or > 1
3D	2nd invariant of $\vec{\nabla}\vec{u}$: Q , Hunt et al. (1988)	> 0
3D	Complex eigenvalues of $\vec{\nabla}\vec{u}$: $\Delta_{\vec{\nabla}\vec{u}}$, Chong et al. (1990)	discriminant > 0
3D	Median eigenvalue of $\mathbf{S}\mathbf{S} + \mathbf{\Omega}\mathbf{\Omega}$: λ_2 , Jeong & Hussain (1995)	< 0

by nature does not show this dependence. We choose LIC to visualize the velocity components perpendicular to a vortex axis. (We used the implementation of LIC in OpenDX by Petkov (2006) as a basis and developed it further.) Two shortcomings of LIC (and streamlines) are that it neither reveals information on the magnitude (vortex strength) nor on the rotational sense of a vortex. (Short before publishing, we got aware of the oriented LIC (OLIC) introduced by Wegenkittl et al. (1997). This extension to LIC provides information on the rotational sense of a vortex. They note that the filter-kernel length may be adapted to the local velocity magnitude to even visualize the vortex magnitude.) In contrast to the normal vorticity, LIC fails to predict the correct position of the vortex core if the vortex axis is not cut perpendicularly.

Therefore, we colorize gray-scale LIC images by the axial vorticity and add velocity vectors next to them, see Figs. 4.10 and 4.18. Furthermore, experience with the LES results revealed that a vortex which is not cut perpendicularly may appear as twins of small, co-rotating vortices.

Illustrating the vorticity or helicity uses the curl of the velocity field. Visualizing the normal vorticity is the only one among them showing the rotational direction. Besides the pressure, the vorticity magnitude is a computationally cheap method to identify vortices. However, it is known to fail at walls.

To convey an impression of the three-dimensional shape of a vortex, more elaborate criteria make use of the rate-of-deformation (or velocity gradient) tensor $\vec{\nabla}\vec{u} = \partial u_i / \partial x_j$. The associated characteristic equation in Chong et al. (1990) reads

$$0 = \lambda^3 + P\lambda^2 + Q\lambda + R \quad , \quad (2.39)$$

using

$$\begin{aligned} P &= -\text{tr} \left(\vec{\nabla}\vec{u} \right) \quad , \\ Q &= \frac{1}{2} \left(P^2 - \text{tr} \left(\left(\vec{\nabla}\vec{u} \right) \left(\vec{\nabla}\vec{u} \right) \right) \right) \quad , \\ R &= - \left| \vec{\nabla}\vec{u} \right| \quad . \end{aligned}$$

The velocity gradient tensor is split up into the symmetric rate-of-strain \mathbf{S} and skew-symmetric rate-of-rotation $\mathbf{\Omega}$ tensors

$$\mathbf{S} = s_{ij} = \frac{1}{2} \left(\frac{\partial u_i}{\partial x_j} + \frac{\partial u_j}{\partial x_i} \right) \quad , \quad \mathbf{\Omega} = \omega_{ij} = \frac{1}{2} \left(\frac{\partial u_i}{\partial x_j} - \frac{\partial u_j}{\partial x_i} \right) \quad . \quad (2.40)$$

The old-fashioned kinematic vorticity number $N_k := |\vec{\omega}| / \sqrt{2s_{ij}s_{ij}}$ of Truesdell (1954) gives information on the 'quality' of the vortex rather than on its strength. At least for incompressible flow, $N_k > 1$ is equivalent to $Q > 0$. Q represents the second invariant of $\vec{\nabla}\vec{u}$ and marks vortices, cf. Hunt et al. (1988). Another hint on a vortex is given by the existence of complex eigenvalues of the velocity gradient tensor which is equivalent to a positive discriminant of the characteristic equation given in Chong et al. (1990). For compressible flows this reads:

$$\Delta_{\vec{\nabla}\vec{u}} = \left(\frac{P^3}{27} - \frac{PQ}{6} + \frac{R}{2} \right)^2 + \left(\frac{Q}{3} - \frac{P^2}{9} \right)^3 \stackrel{!}{>} 0 \quad . \quad (2.41)$$

Finally, Jeong & Hussain (1995) propose that a negative median eigenvalue λ_2 of $\mathbf{SS} + \mathbf{\Omega\Omega}$ defines a vortex. This is the most accurate but also a computationally expensive criterion. For most cases, the Q , Δ and λ_2 criteria give similar results. Strictly speaking, every negative λ_2 value identifies a vortex. Although there is no theoretical justification, it is usually assumed that smaller λ_2 values represent stronger vortices. Since experience shows that only the laminar regions are free of negative λ_2 values in a turbulent flow, we often present iso-surfaces of negative λ_2 values in order to isolate the important vortical structures.

Although Jeong & Hussain (1995) claim that using the pressure, streamlines or vorticity magnitude is inadequate in general, they are still used in recent publications. We also use iso-surfaces of low pressure levels to emphasize yet stronger vortices.

Chapter 3

Turbulent flat-plate boundary layer: validation case

A major part of the film-cooling flow is a modified boundary-layer flow. This chapter studies a flat-plate, turbulent boundary layer, depicted in Fig. 3.1, in preparation of the film-cooling simulation presented in Chap. 4. For consistency with the later film-cooling cases, the hole diameter d is used to non-dimensionalize all length scales.

First, the simulation parameters of the six simulation cases listed in Tab. 3.1 are discussed in Sec. 3.1. (The nomenclature used for the simulation cases is detailed on p. IX.) Besides the SEM parameters shown in Sec. 3.1.1, this includes the Cartesian grids for cases $1a\alpha$ to $1d\alpha$, and $1d\epsilon$ described in Sec. 3.1.3. The non-Cartesian grid of case $2b\alpha$, however, will be shown in Sec. 4.1.2 due to its similarity with the grid of that chapter. The initial condition and the initial transient are explained in Sec. 3.1.2.

Section 3.2 presents results of the non-Cartesian case $2b\alpha$ and compares them with literature data. The effects of the grid and the Mach number are discussed in Sec. 3.3, followed by a summary of the chapter in Sec. 3.4.

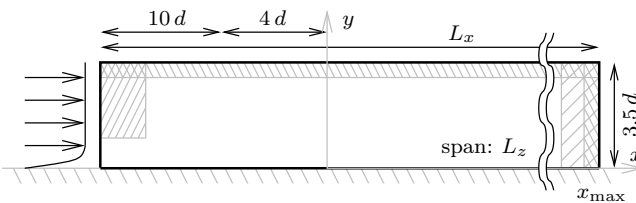


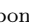


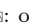
Figure 3.1: Sketch of the simulation setup for boundary-layer cases $1a\alpha$ to $1d\epsilon$ and $2b\alpha$. : Inflow sponge; : outflow sponge; : downstream grid stretching; : plate/wall.

Table 3.1: Turbulent boundary-layer cases. Dependent parameters: $x_{\max}/d = 4$ and $L_z/d = 3$ for Cartesian grids, $x_{\max}/d = 28$ and $L_z/d = 6$ for non-Cartesian grid, $T_\infty = 293$ K for $Ma_\infty = 0.2$ cases, $T_\infty = 1500$ K for $Ma_\infty = 0.4$ case.

Case	grid	Δy_{\min}^+	$\Delta t U_\infty/d$	$N_x \times N_y \times N_z$	Ma_∞
1a α	Cartesian	$\sqrt{2}/2$	0.00085	420 \times 120 \times 210	0.2
1b α	Cartesian	1	0.00120	288 \times 95 \times 149	0.2
1c α	Cartesian	$\sqrt{2}$	0.00170	207 \times 77 \times 105	0.2
1d α	Cartesian	2	0.00240	148 \times 64 \times 75	0.2
1d ε	Cartesian	2	0.00480	148 \times 64 \times 75	0.4
2b α	non-Cartesian	1	0.00075	$\prod = 26100775$	0.2

3.1 Simulation setup

The Reynolds number based on the freestream velocity U_∞ and the hole diameter d is chosen as $Re_{\infty,d} = 6570$ as in the reference experiment by Ahn et al. (2003). At $x/d = 0$, the boundary layer Reynolds number based on the displacement thickness is $Re_{\infty,\delta}|_{x/d=0} = 957$, cf. Tab. 4.1. The Mach number Ma_∞ based on the freestream data is increased from a value around 0.03 in the experiment to 0.2 to increase the timestep-limit of our compressible flow solver. The low Mach number still ensures a low level of compressibility effects.

The relaxation coefficient χ is chosen from $\{0; 0.5, 1, 2, 5, \dots, 500\}$ and as low as possible such that the model drains just enough energy for the simulation to run stably over time. This minimal relaxation coefficient χ is 0, 1, 2, and 5 for cases 1a α to 1d α , respectively. Hence, for the considered boundary layer, the *lower bound* of the relaxation coefficient seems to be proportional to the grid spacing. (The *upper bound* might scale with Δt due to the CFL limit.) This could be explained by the fact that with increasing grid spacing more energy has to be drained by the model, whose influence is determined by the relaxation coefficient χ , cf. Eq. (2.20). Consistently, $\chi = 5$ and 1 are used for cases 1d ε and 2b α since their resolutions are at least as fine as the resolutions of cases 1d α and 1b α , respectively.

The timestep Δt is kept constant for each simulation and set to $0.006 \Delta y_{\min}^+ d/U_\infty \cdot Ma_\infty$ and $7.5 \cdot 10^{-4} d/U_\infty$ to ensure around 80% of the CFL limit for cases 1a α to 1d ε and case 2b α , respectively. The statistics presented in the following are averaged over a period of 10 and 2 flow-

Table 3.2: Sponge and grid-stretching parameters, cf. Fig. 3.1 and Secs. 2.4.2 and 3.1.3

Location	range of		amplification
	transition	plateau	σ_a
inflow	$x/d = x_{\min} + 5 \dots x_{\min} + 4.5$	$\dots x_{\min}$	5
inflow	$y/d \approx 1.3 \dots 1.5$	$\dots y_{\max}$	
ambient	$y/d = y_{\max} - 1 \dots y_{\max} - 0.5$	$\dots y_{\max}$	0.25
outflow	$x/d = x_{\max} - 1 \dots x_{\max} - 0.5$	$\dots x_{\max}$	1
outflow	$x/d = x_{\max} - 3 \dots$	x_{\max}	grid stretching
plate	$y/d = 0 \dots$	≈ 1	grid stretching

through times L_x/U_∞ for cases 1a α to 1d ϵ and case 2b α , respectively. To include the highest frequencies, each timestep is sampled.

All simulations were carried out on 8 to 32 processors of a NEC SX-8 vector computer with an efficiency of 20% to 24% of the theoretical peak performance. Typical computations of cases 1a α , 1b α , 1c α , 1d α , 1d ϵ , and 2b α ran for 116, 102, 39, 15, 8, and 313 hours on 24, 24, 8, 8, 8, and 32 processors, respectively. Accordingly, the total number of processor hours (wall-clock hours times number of processors) was 2784, 2448, 312, 120, 64, and 10016, respectively. More details, such as the performance of the principal routines as well as scaling tests, are given in App. B.

The sponge parameters and the regions of grid-stretching are summarized in Tab. 3.2. The ambient and outflow sponges successfully prevent a pressure drift and the inflow sponge reasonably suppresses oscillations caused by the inflow condition.

3.1.1 SEM parameters

For the turbulent inflow condition, cf. Sec. 2.3.2, a number of parameters are required. The friction velocity $u_\tau|_{x/d=-14}$ and the mean velocity profiles at the inflow are taken from the logarithmic law of Monkewitz et al. (2007), cf. Sec. 3.1, at $x = x_{\min} + d/2$. The small shift of $+d/2$ results in the desired momentum thickness at $x = 0$ for all cases but 1d ϵ which is shifted by $-0.8d$. The root-mean-square (RMS) values of the velocity fluctuations and the Reynolds stress are taken from an incompressible flow DNS at $Re_{\infty,\vartheta} = 1000$ by Schlatter et al. (2009) and scaled by $u_{\tau,\text{in}}$. The lengthscale of the synthetic eddies depends on the plate-normal distance and is determined by the turbulence

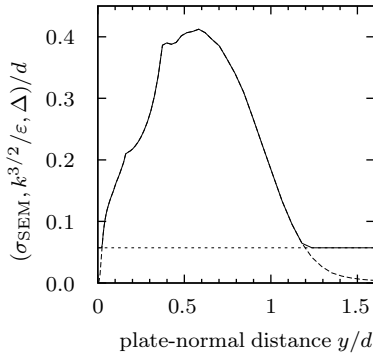


Figure 3.2: Composition of lengthscale of synthetic eddies. (—): Eddy lengthscale σ_{SEM}/d ; (- - -): turbulence lengthscale $k^{3/2}/(\varepsilon d)$; (.....): maximum of plate-normal and streamwise grid spacing Δ/d .

lengthscale $k^{3/2}/\varepsilon$ with the maximal grid-spacing at the inflow plane as the lower bound, cf. Jarrin (2008, Eq. (8.4)). The turbulent kinetic energy k follows from the RMS profiles, however, the dissipation-rate ε is obtained from an incompressible flow DNS with $Re_{\infty, v} = 1410$ by Spalart (1988) as it is not published in Schlatter et al. (2009). The eddy lengthscale obtained is depicted in Fig. 3.2; the kinks are caused by missing data which is linearly interpolated. The eddies induce velocity fluctuations following a truncated Gaussian shape function Jarrin (2008, Eq. (4.62)). A converged solution is obtained above 1000 eddies for a similar case, in terms of Reynolds number and extent of inflow plane, cf. Jarrin (2008, Figs. 8.1 to 8.3). Using 2000 eddies for cases $1a\alpha$ to $1d\alpha$ provides sufficient flatness of the velocity fluctuations while maintaining acceptable computational costs. Cases $2b\alpha$ and all film-cooling cases use 4000 eddies, since the turbulent inflow plane has twice the spanwise extent. The time-dependent SEM boundary condition is active below the plateau region of the inflow sponge $y/d \lesssim 1.5$, Tab. 3.2. In the region where the inflow-sponge is fully active, $1.5 \lesssim y/d \leq y_{\text{max}}/d$, the boundary condition switches to a steady one.

3.1.2 Boundary and initial conditions and transient

The boundary conditions are explained in Sec. 2.4. The values are the same as for the initial conditions presented in the following.

As initial condition, the downstream velocity component is set

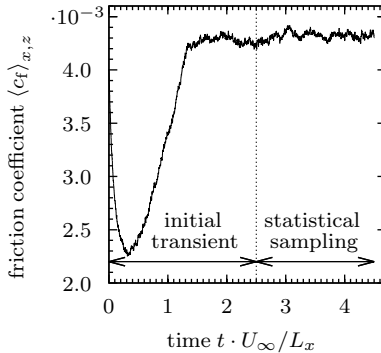


Figure 3.3: Initial transient of spatially-averaged friction coefficient of case 2b α .

according to the logarithmic law of Monkewitz et al. (2007) using constants for the flat-plate boundary layer from Monkewitz et al. (2008) and a momentum thickness $\vartheta/d \approx 0.15$ to meet the conditions, assumed to be given at $x/d = 0$, of the reference experiment by Ahn et al. (2003). The spanwise and plate-normal components of the velocity are set to zero and set in accordance to the mass-conservation law, respectively. The temperature follows from the velocity distribution, cf. Sec. 2.3.2. Finally, imposing a uniform pressure distribution yields the density using the ideal gas law. A compilation of the initial conditions is also found in the last column of Tab. 4.2.

Sampling starts after an initial transient of 2.5 flow-through times. Following Quadrio & Luchini (2003), the time for the slowest structures to reach the end of the domain corresponds to around 2.1 flow-through times of the freestream. Consequently, the spatially-averaged friction coefficient remains fluctuating around a constant level during the statistical sampling, cf. Fig. 3.3.

3.1.3 Computational grid

The Cartesian grids are generated by a custom tool. The computational domain is a cuboid with the spatial extent of $L_x/d \times L_y/d \times L_z/d = 18 \times 3.5 \times 3$. It consists of a Cartesian grid subdivided in the downstream direction into multiple blocks of (up to division remainder) equal extent in index space. In the streamwise direction, the grid is equidistant (Δx_{\min}) except for the outflow region. The grid is coarsened to

wards the outflow to damp turbulence following the explicit geometrical law of App. A.2 using a ratio of 1.05. In the plate-normal direction, the implicit hyperbolic tangent law described in App. A.2 is employed using a maximal ratio of 1.06. In the spanwise direction, the grid is equidistant across the whole domain (Δz). The grid spacings of the individual spatial directions are expressed with respect to the minimal plate-normal spacing Δy_{\min} to carry out the grid convergence study in Sec. 3.3. The minimal streamwise, maximal plate-normal, and spanwise spacing is $\Delta x_{\min} = 17 \Delta y_{\min}$, $\Delta y_{\max} = 17 \Delta y_{\min}$, and $\Delta z = 6 \Delta y_{\min}$, respectively.

3.2 Results of non-Cartesian grid

3.2.1 Velocities and effect of inflow treatment

Figure 3.4(b) shows profiles of velocity fluctuations at the first (virtual) coolant ejection position, roughly 11 inflow boundary-layer thicknesses downstream of the inflow boundary. The comparison with DNS data shows a systematic overprediction between $y^+ = 20$ and 300 with a peak deviation at $y^+ \approx 150$. This appears to be an effect of the synthetic inflow turbulence generation method, also observed by Jarrin (2008, Fig. 8.30, $x/\delta_0 = 10$) for a similar case.

Furthermore, we observe that the fluctuations do not vanish completely in the freestream (Fig. 3.4(b), insert). This is supposed to be a consequence of the inflow condition. An examination of the initial phase of the simulation reveals that pressure waves are generated by the Dirichlet inflow condition in the region where no sponge is active ($y/d \lesssim 1.5$). These waves propagate into the freestream region, causing velocity fluctuations. However, there are no spurious reflections by the inflow and outflow conditions supplemented by a sponge.

The mean velocity profile at the first (virtual) coolant ejection position $x/d = -4$ obtained compares very well with those of a DNS and the logarithmic law for similar Reynolds numbers, cf. Fig. 3.4(a). The parameters used for the logarithmic law are taken from Monkewitz et al. (2007) which has been validated against a large number of physical experiments. It should be noted that Monkewitz et al. (2007) focuses on boundary layers with Reynolds numbers higher than the present case. This might be a reason for deviations between the simulation data, including the DNS of Schlatter et al. (2009), and the logarithmic law of Monkewitz et al.

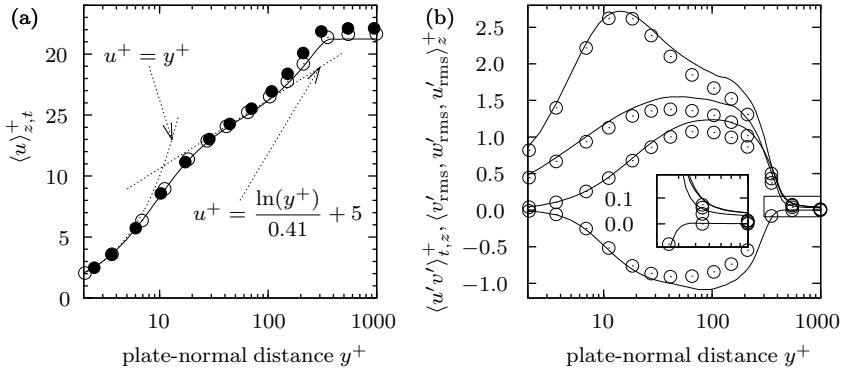


Figure 3.4: Spanwise and time-averaged field at the first (virtual) coolant ejection position $x/d = -4$. (a): Velocity $\langle u \rangle_{z,t}^+$ vs. plate distance. (—): Case 2b α , $Re_\vartheta = 924$; ●: logarithmic law of Monkewitz et al. (2007, 2008), $Re_\vartheta = 908$; ○: DNS of Schlatter et al. (2009), $Re_\vartheta = 1000$. (b): Velocity fluctuations vs. plate distance. Insert: magnification of freestream region. From top to bottom: streamwise $\langle u'_{rms} \rangle_z^+$; spanwise $\langle w'_{rms} \rangle_z^+$; plate-normal RMS $\langle v'_{rms} \rangle_z^+$; Reynolds stress $\langle u'v' \rangle_{z,t}^+$.

(2007). Nevertheless, our Reynolds number is just inside the region of validity of the Monkewitz et al. (2007) wall-law parameters.

3.2.2 Inflow transient and effect of outflow treatment

Figures 3.5(a) to 3.5(c) illustrate the downstream development of three major integral boundary-layer properties, the shape factor H , the momentum thickness ϑ , and the friction velocity u_τ . The simulation results are compared to the logarithmic law of Monkewitz et al. (2007), an approximate solution for turbulent momentum boundary layer Kays et al. (2005, Eq. (11-20)) as well as DNS data of Schlatter et al. (2009) (using the log law of Monkewitz et al. (2007) to transfer the given Re_ϑ dependency to the x/d dependency).

Beginning at the inflow, all curves show an initial transient which ends upstream of $x/d = 0$. Downstream of this transient, the curves follow the reference data with a slight shift. Towards the end of the domain, the friction velocity and the momentum thickness show bumps and bending, respectively, caused by the grid-stretching and the outflow sponge which become active in this region.

Overall, an acceptable agreement between the simulation and the

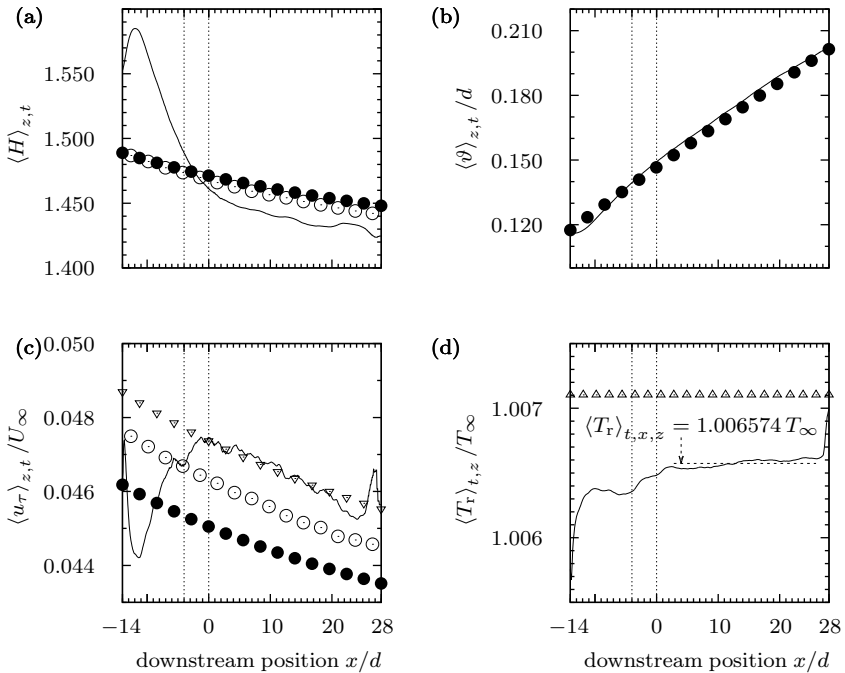


Figure 3.5: (a)–(c): Spanwise and time-averaged downstream development of integral boundary-layer properties. (a): Shape factor $\langle H \rangle_{z,t}$; (b): momentum thickness $\langle \vartheta \rangle_{z,t}/d$; (c): friction velocity $\langle u_\tau \rangle_{z,t}/U_\infty$. (.....): (virtual) positions of the coolant ejection; ∇ : $u_\tau/U_\infty = \sqrt{0.0125} Re_\vartheta^{-1/8}$ Kays et al. (2005); further line types as in Fig. 3.4. (d): Downstream development of the streamwise-averaged recovery temperature normalized by freestream temperature $\langle T_r \rangle_{z,t}/T_\infty$. Δ : recovery factor $Pr^{1/3}$ Schlichting & Gersten (2006); (.....): average simulated temperature $\langle T_r \rangle_{t,x/d=2\dots 25,z}/T_\infty$.

references is achieved. Downstream of $x/d \approx -7$, u_τ deviates from the DNS and the approximate solution by at most 3% and approaches the DNS result further downstream. The deviation seems to be related to the spatial resolution, cf. Sec. 3.3. However, the logarithmic law of Monkewitz et al. (2007) shows a smaller value than the DNS across the whole domain. A reason might be that this logarithmic law was primarily fitted for higher Reynolds numbers.

Finally, the recovery temperature T_r is evaluated, which is used later to normalize the temperature for film-cooling cases. Figure 3.5(d) depicts

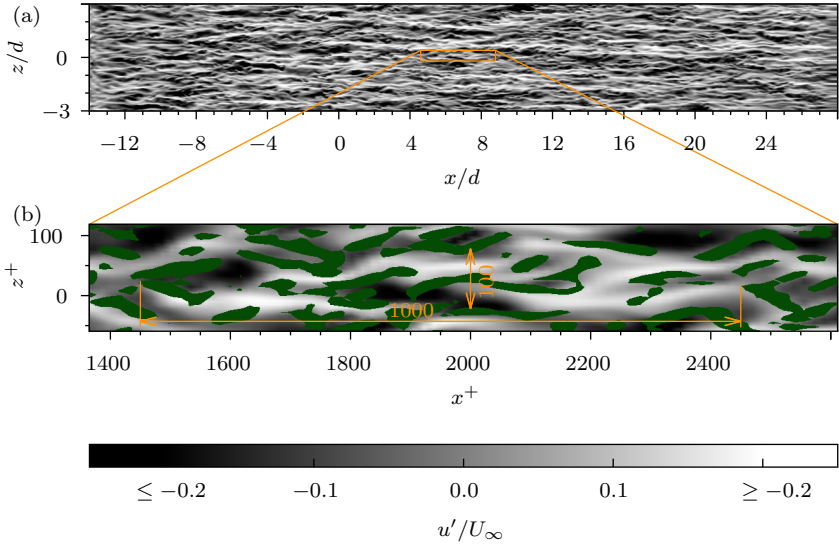


Figure 3.6: Instantaneous streaks at $t = 189 d/U_\infty$. Bottom view through the plate on the plane $y^+ = 5$ gray-scaled by the fluctuating streamwise velocity u' and on opaque, green iso-surfaces of the vortex criterion $Q = 0.5$ for $y^+ \leq 5$. (a): Total view; (b): ten-fold magnification.

the downstream evolution of the flow temperature at the plate. Besides the inflow transient and outflow effects already mentioned, a small increasing tendency is visible. This increase appears to be physically correct due to the increase in friction with growing Reynolds numbers.

3.2.3 Instantaneous flow

Streamwise streaky structures are known to exist in the viscous sub-layer of a turbulent boundary layer. Figure 3.6(a) shows high- and low-speed streaks with respect to the mean velocity. Vortical structures are visible in Fig. 3.6(b), mostly outside these streaks, in the gray area, which agrees with Kline et al. (1967). The characteristic spacing in spanwise and downstream direction agrees well with known values of 100^+ and 1000^+ , respectively.

The inflow transient and the effect of the outflow treatment are obvious in Fig. 3.6(a). Nevertheless, the velocity streaks do not show

major differences in the region of grid refinement around the virtual coolant ejection positions at $x/d = -4$ and 0.

3.3 Grid and Mach number variation

Comparing the non-Cartesian case $2b\alpha$ with the streamwise shorter, spanwise narrower Cartesian case $1b\alpha$ does not show systematic differences, cf. Fig. 3.7. Especially the velocity profile, the fluctuations and the shape factor compare very well albeit the grid regularity and dimension differs notably, Figs. 3.7(a) to 3.7(c).

The parallelism of the momentum thickness and the friction velocity is less obvious, Figs. 3.7(d) and 3.7(e), since the region between inflow transient and beginning outflow effects ($x/d > 1$) is short. Two slight bumps of the recovery temperature in the vicinity of the virtual coolant ejection positions are apparent in Fig. 3.7(f), which are attributed to numerical effects caused by the varying grid resolution and shear of the cells, visible in Fig. 4.4(b).

To show the consistency of the simulation and to investigate the required resolution, a grid convergence study is conducted. Four grids (cases $1a\alpha$ – $1d\alpha$) are tested varying the resolution denoted by Δy_{\min} (and thereby Δx and Δz accordingly) by a factor of $\sqrt{2}$ between each other, cf. Tab. 3.1. Figures 3.8(b), 3.8(d), and 3.8(f) show that the fluctuations, the momentum thickness, and the recovery temperature only weakly depend on the resolution. The shape factor shows shorter inflow transients for higher resolutions for all cases except $1b\alpha$, Fig. 3.8(c). A generally monotonic dependency of the friction velocity on the resolution is observed at the inflow transient and between $x/d = -4$ and 0, Fig. 3.8(e). As a consequence, the peak values u_{∞}^+ increase with finer resolution, Fig. 3.8(a).

Figure 3.8(e) shows that the friction velocity u_{τ} is a sensitive property with respect to the grid resolution. The velocity is averaged downstream over the region $x/d = -4 \dots 0$ in which neither the inflow transient nor the outflow treatment is present. Figure 3.9 shows the improvement of the solution with finer resolution. For case $1b\alpha$, the LES result deviates from the reference DNS by roughly 3%. We consider this deviation acceptable and use this resolution for case $3b\alpha$ (using the resolution of case $1a\alpha$ for film-cooling cases would be infeasible due to the high computational costs).

The Mach number of $Ma_{\infty} = 0.2$ used for the basic cases, i.e.

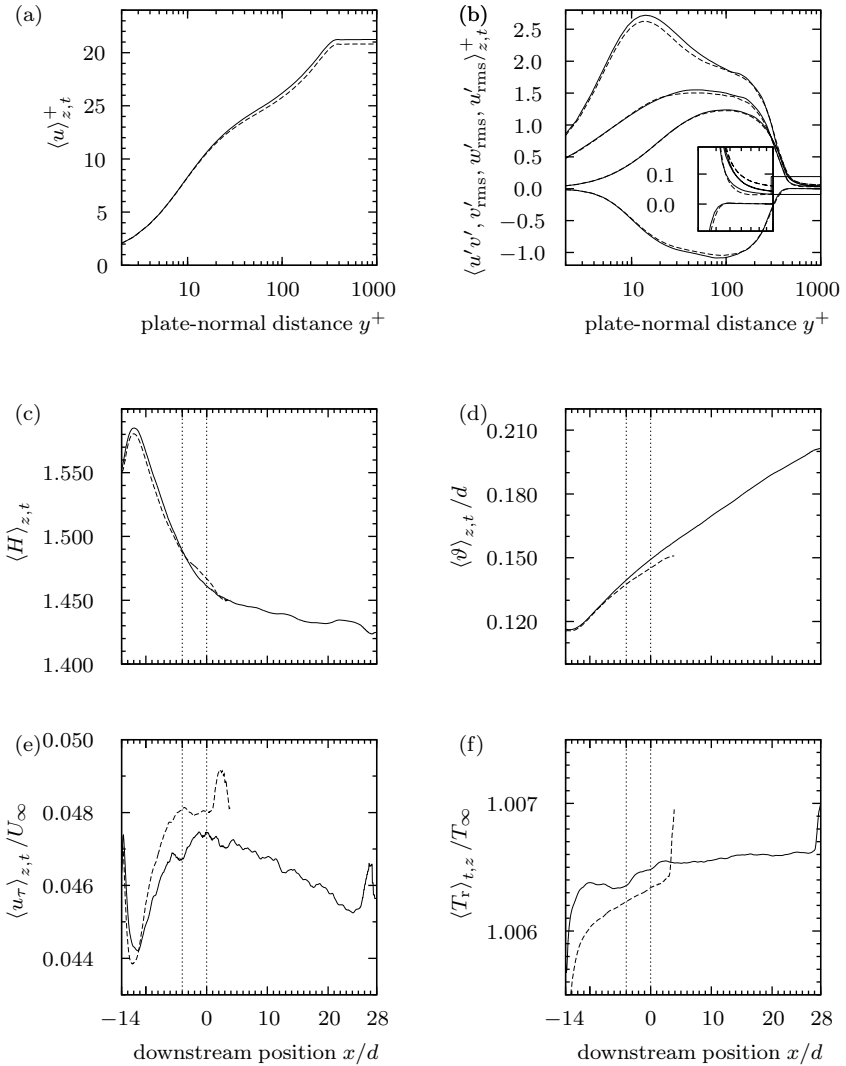


Figure 3.7: Effect of grid regularity and dimension. (a), (b): Analogous to Fig. 3.4; (c)–(f): analogous to Fig. 3.5. (—): Non-Cartesian, large dimension case 2b α ; (---): Cartesian, small dimension case 1b α .

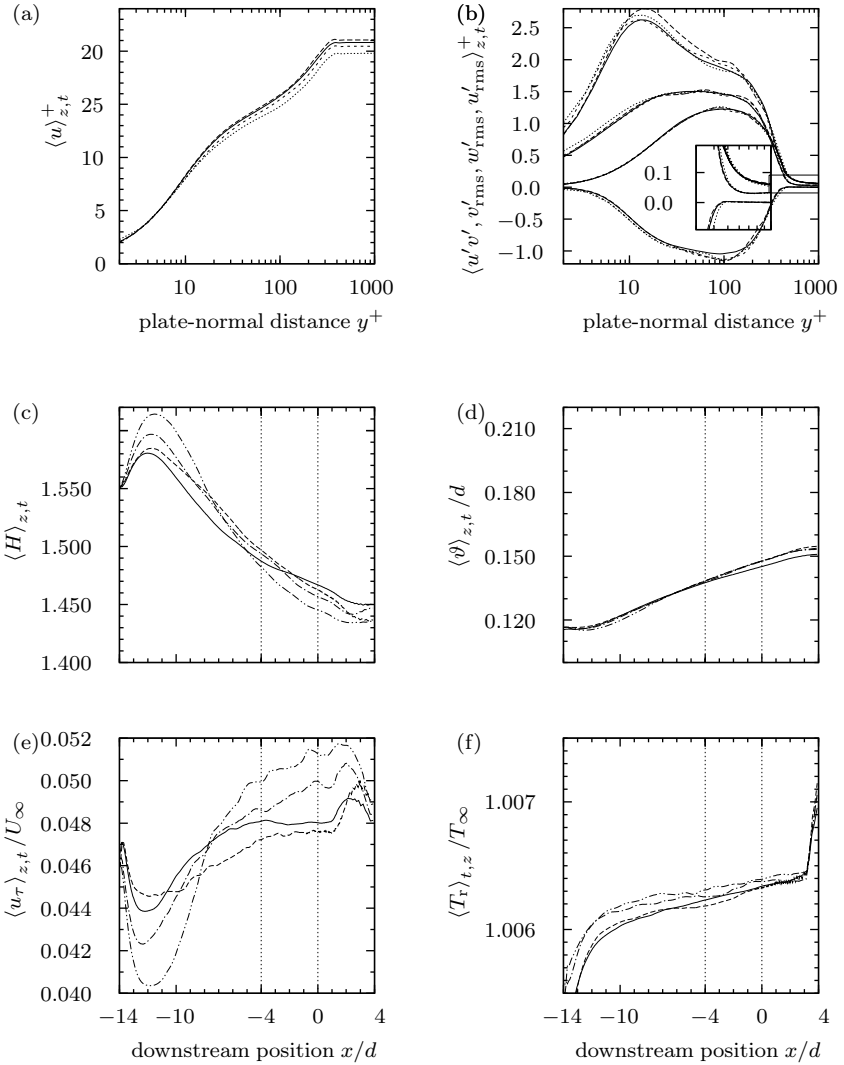


Figure 3.8: Effect of grid resolution, analogous to Fig. 3.7. (---): $\Delta y_{\min}^+ = \sqrt{2}/2$ case 1a α , (—): = 1 case 1b α , (-.-): = $\sqrt{2}$ case 1b α , (-.-.-): = 2 case 1b δ .

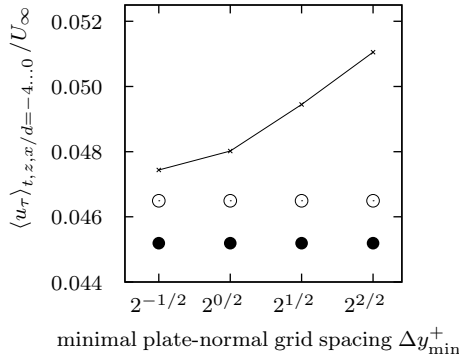


Figure 3.9: Spanwise-, downstream- (over $x/d = -4 \dots 0$), and time-averaged friction velocity $\langle u_\tau \rangle_{t,z,x/d=-4\dots 0} / U_\infty$ vs. minimal plate-normal grid spacing Δy_{\min}^+ . (—): Cases 1a to 1d α ; ●: logarithmic law with parameters by Monkewitz et al. (2007, 2008); ○: DNS by Schlatter et al. (2009).

1d α , represents an essentially incompressible flow. Comparing this case to 1d ϵ with $Ma_\infty = 0.4$ allows for judging the effects of slight compressibility. Figures 3.10(a), 3.10(b), and 3.10(d) illustrate minor differences. The shape factor and the friction velocity show shorter inflow transients, Figs. 3.10(c) and 3.10(e) and nearly the same values as they approach the outflow. The recovery temperature increases by roughly 2% for the slightly compressible case.

3.4 Summary

From the boundary-layer simulations using the non-Cartesian case 2b α we conclude that the basic simulation setup including boundary treatment and modeling parameters is able to produce results in good agreement with DNS data from literature and the logarithmic law of the wall.

The effect of the grid regularity, the domain extent, the grid resolution, and the Mach number on the physical quantities are small. The grid convergence study shows a monotonic behavior of the most sensitive quantity u_τ with the resolution.

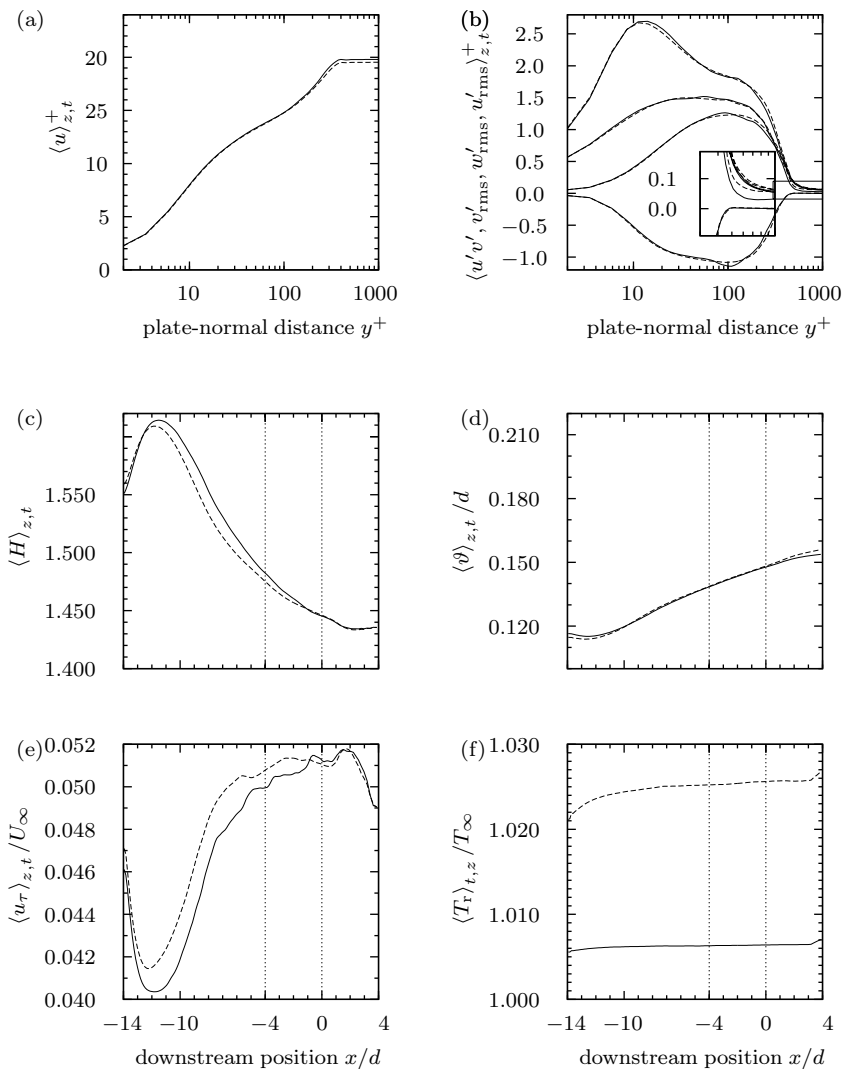


Figure 3.10: Effect of slight compressibility, analogous to Fig. 3.7. (—): $Ma_\infty = 0.2$ case 1d α ; (---): = 0.4 case 1d ϵ .

Chapter 4

Film cooling: reference case

This chapter deals with the numerical simulation of case $3b\alpha$ which is similar to the reference experiment by Ahn et al. (2003, conf. 1). The computational domain is depicted in Fig. 4.1 including a plenum which feeds coolant through two cooling holes into the flat-plate boundary layer of Chap. 3. According to Schlüter & Schönfeld (2000), plenum and holes should be included in the simulation domain due to their effect on the coolant jet trajectories. Figure 4.2 illustrates some streamlines and contours to convey an impression of the mean flow and cooling, respectively.

Section 4.1 presents the simulation setup including the non-Cartesian grid discussed in Sec. 4.1.2. The initial and boundary conditions are explained in Sec. 4.1.1 followed by showing the quasi-steady state during statistical sampling in Sec. 4.1.3. Starting from the plenum (Sec. 4.2) over the cooling holes (Sec. 4.3) to the boundary layer and film above the plate (Sec. 4.4), the mean flow is studied in detail. Section 4.4.1 also presents the film-cooling effectiveness and compares it with the refer-

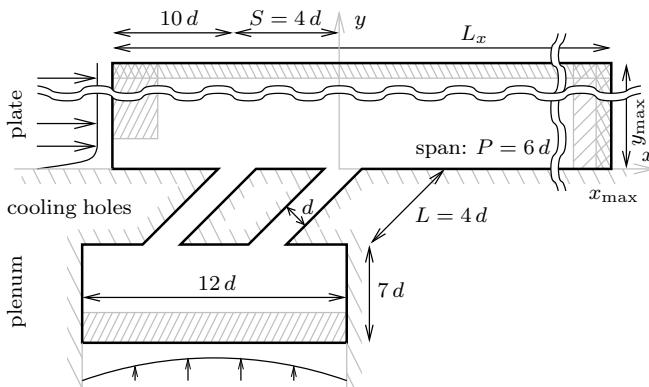


Figure 4.1: Sketch of simulation setup for film-cooling cases $3b\alpha$ to $51d\delta$, analogous to Fig. 3.1.

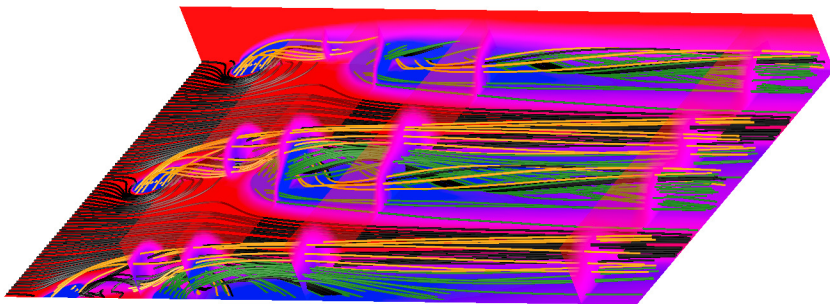


Figure 4.2: Mean flow above the plate ($-6 \leq x/d \leq 17$, $0 \leq y/d \leq 2$) visualized by streamlines of two spanwise periods ($-6 \leq z/d \leq 6$) of the computational domain. Coolant ejected through the upstream holes (—), through the downstream holes (—), and hot gas (—). High (blue) and low (red) amount of cooling at the plate, in the center plane, and in (partly opaque) transversal planes at $x/d = -1, 1, 5, 15$.

ence experiment as well as with the coolant concentration in Sec. 4.4.2. After the instantaneous flow features and the vorticity production are discussed in Sec. 4.5, the chapter is summarized in Sec. 4.6.

4.1 Simulation setup

First, several reference regions are defined in Fig. 4.3(a) and indices are assigned to them. Freestream properties (index ∞) are found in the freestream region of the turbulent plate boundary-layer and recovery properties (index r) of a turbulent boundary layer without coolant injection are measured at the plate. With coolant ejection, the hot-gas (index h) and film (index f) properties are averaged along transversal planes above the plate at $x/d = -7$ and 20, respectively. Coolant (index c) and plenum (index p) properties are averaged along plate-parallel planes over both sub-plena or cooling holes at the injection at $y/d = 0$ and downstream of the sponge at $y/d \approx -7.3$. The sponge's size of plateau and transition is $1d$.

Next, a number of right-handed Cartesian auxiliary coordinate systems are introduced in Figs. 4.3(b) and 4.3(c) to keep track of the position of the various views and cross-sections that will be presented in the following. The principal system $[x, y, z]$ has its origin at the downstream hole, associated with the index 2. By first translating it to the upstream hole, associated with the index 1, and then yawing around the y -axis by

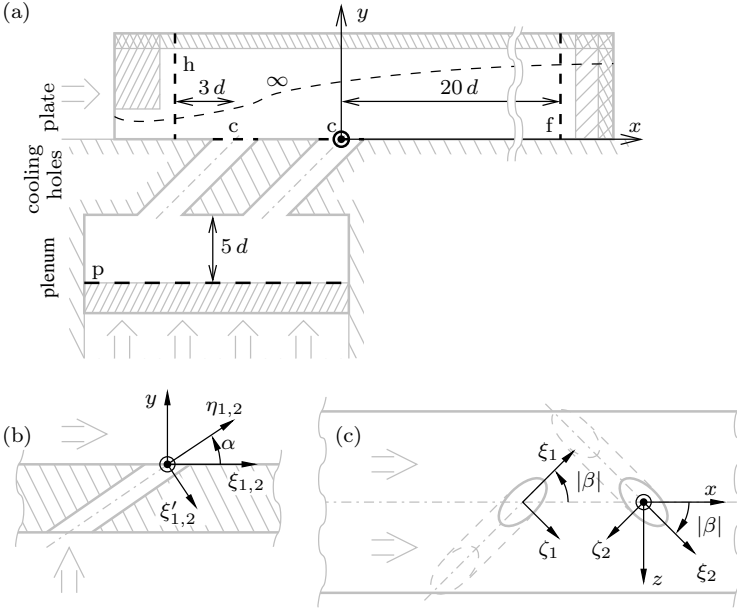


Figure 4.3: (a): Reference regions and (b), (c): coordinate systems.

an angle β , an additional system $[\xi_1, y, \zeta_1]$ is obtained. Another rotation by $90^\circ - \alpha$ around ζ_1 yields the coordinate system $[\xi'_1, \eta_1, \zeta_1]$ that is aligned with the hole axis. (Depending on the context, η also denotes the cooling effectiveness.) Likewise, the systems $[\xi_2, y, \zeta_2]$ and $[\xi'_2, \eta_2, \zeta_2]$ are introduced; both share their origin with the $[x, y, z]$ system.

The plate boundary-layer parameters are the same as for case 2b α which was described in Sec. 3.2. Table 4.1 compares the simulated parameters to the film-cooling reference experiment. From this reference, the blowing ratio $M = (\rho U)_c / (\rho U)_\infty = 1$ and the temperature ratio $TR = T_c / T_\infty \approx 1.068$ are chosen. Because the temperature ratio is greater than one, we actually simulate a case of film heating, nevertheless, the small difference between the injection and freestream temperature renders buoyancy effects negligible.

The inclination α and magnitude of the yaw angle $|\beta|$ of the two in-line holes are 35° and 45° , respectively. The length L , the spanwise

Table 4.1: Physical parameters of non-Cartesian plate boundary-layer case 2b α compared to reference film-cooling experiment. †: Assumed to be given at $x/d = 0$; ‡: assumed to indicate the 99% U_∞ value.

Property	present case 2b α	Ahn et al. (2003)
Ma_∞	0.2	0.03
$Re_{\infty,d}$	6570	6570
$Re_{\infty,\vartheta} _{x/d=0}$	980	957†
$Re_{\infty,x} _{x/d=0}$	379372	n/a
$\delta_{U,99\%} _{x/d=0}/d$	1.18	1.50†,‡
$H _{x/d=0}$	1.46	1.36†

pitch P , and the streamwise spacing S of the holes as well as all further geometrical parameters are sketched in Fig. 4.1.

The timestep is set to $\Delta t \cdot U_\infty / d = 5.5 \cdot 10^{-4}$, corresponding to approximately 80% of the stability limit, and is, therefore, smaller than for case 2b α which uses nearly the same grid above the plate. The timestep decrease is due to the coolant penetrating the closely-spaced plate-parallel grid planes in the vicinity of the plate. The lowest possible value (from the interval given in Sec. 3.1) of $\chi = 20$ is used for the relaxation coefficient. The computation ran for roughly 1000 hours (6 weeks on dedicated compute nodes) on 32 NEC SX-8 processors (32000 processor hours).

4.1.1 Boundary and initial conditions

The boundary conditions match the initial conditions at the boundaries. This means that the respective density and velocities of the initial conditions (i.e. mean turbulent boundary layer profile and Poiseuille channel flow) are set at the inflow planes at $x/d = -14$ and $y/d \approx -9.3$. (Within the turbulent boundary layer, the instantaneous SEM signal is used.) The reference states of the inflow sponges are equal to the initial conditions at the respective locations. The outflow boundary conditions are non-reflecting and do not impose a prescribed physical quantity, cf. Sec. 2.4.1. The outflow sponges only drive the pressure towards p_∞ , cf. Sec. 2.4.2.

The initial conditions are presented in the following and summarized in Tab. 4.2. The uniformly distributed density in the plenum is adjusted in preparatory tests to ensure the desired coolant temperature at the

ejection positions. For case $3b\alpha$, the injection density is set to $0.982 \rho_\infty$.

A velocity profile of a laminar Poiseuille flow is imposed up to the upper end of the plenum. The channel flow Reynolds number in the plenum is about 1300 which is well below the critical stability limit of 5772, cf. Criminale et al. (2003). In the holes, however, the flow neither will be laminar nor will it resemble a fully developed turbulent pipe flow. For simplicity, we use the velocity profiles of a laminar Poiseuille pipe flow as initial condition. The velocity profile is scaled to match the desired mass-flux defined by the blowing ratio M .

In order to shorten the initial transient, a meaningful value of the initial plenum-pressure is beneficial which is set to $1.069 p_\infty$, as obtained from previous test runs. In the holes, the initial pressure is set to ambient conditions and the desired coolant temperature is assigned. The density in the holes and the temperature in the plenum are evaluated using the ideal gas law. Finally, the coolant concentration in the holes and plenum are set to unity.

4.1.2 Computational grid

Similar to cases $1a\alpha$ to $1d\epsilon$, the grid is refined towards the inner (plenum-side) and outer ($y/d > 0$) plate surfaces. The three-dimensional grid consists of the extruded, plane, two-dimensional grids on the inner and outer surfaces of the plate, see Fig. 4.4(a).

The round holes call for a special block structure. Figure 4.4(b) shows two surrounding O-grids that are used to refine the grid in the hole-radial direction. Since the two holes have opposite yaw angles, the spanwise distance of their origins at the plenum is large. Therefore, the plenum is split into two fully staggered sub-plena, cf. Fig. 4.5. The blocks of the sub-plena are periodically connected to represent one coherent physical plenum. (There are also other possibilities like partly staggered sub-plena or one plenum, but this would impose additional restrictions on the number of cells in the z -direction in the plenum or stronger shear-angles of the cells for the grid generator used, cf. Sec. 5.1.3.)

Above the plate, the grid resolution is at least as fine as for case $1b\alpha$. In the vicinity of the holes, the streamwise and spanwise resolution has to be refined to allow for smooth transitions from the O-grids to the neighboring grid regions, cf. Fig. 4.4(b). The hole-radial resolution in the xz -plane and the resolution in the y -direction at the orifice between plenum and holes are $\Delta r_{xz}/d \approx 5 \cdot 10^{-3}$ and $\Delta y_{p,\min}/d \approx 70 \cdot 10^{-3}$, respectively.

Table 4.2: Initial condition in primitive variables.

Property	plenum	holes	plate boundary-layer
density	$DR_p \rho_\infty$	$1/TR \rho_\infty$ (ideal gas law)	$\left(2(\gamma - 1)Ma_\infty^2 / \sqrt[3]{Pr} \dots 1\right) \cdot \rho_\infty$ (ideal gas law)
velocities in local coordinate system			
averaged streamwise	$U_p = M \pi / (2 \cdot 6 \cdot 12 DR_p) U_\infty$	$U_c = 2 M TR / \pi U_\infty$	$< U_\infty$
streamwise	$(0 \dots 3/2) U_p$ (Poiseuille channel flow)	$(0 \dots 2) U_c$ (Poiseuille pipe flow)	$(0 \dots 1) U_\infty$ (log-law Monkewitz et al. (2007))
wallnormal / radial	$0 U_\infty$ (fully developed)	$0 U_\infty$ (fully developed)	$(0 \dots \ll 1) U_\infty$ (from thickening)
spanwise / circumferential	$0 U_\infty$ (2D flow)	$0 U_\infty$ (2D flow)	$0 U_\infty$ (2D flow)
temperature	$PR_p / DR_p T_\infty$ (ideal gas law)	$TR T_\infty$	$\left(1 \dots \sqrt[3]{Pr} / (2(\gamma - 1)Ma_\infty^2)\right) T_\infty$ (Busemann-Crocco)
pressure	$PR_p \rho_\infty T_\infty$	$1 / (\gamma Ma_\infty^2) \rho_\infty T_\infty$	$1 / (\gamma Ma_\infty^2) \rho_\infty T_\infty$
concentration	c_c	c_c	$0 c_c$

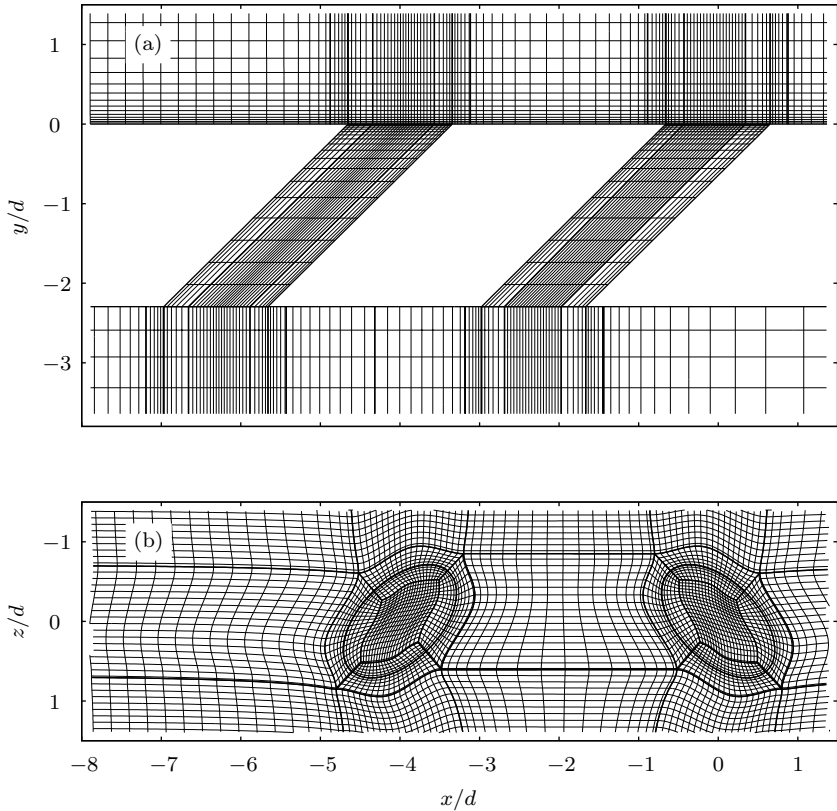


Figure 4.4: Grid planes near ejection holes used for cases $3b\alpha$ and $2b\alpha$. (a): Center plane at $z/d = 0$; (b): plate plane at $y/d = 0$. (—): Every fourth grid line; (—): block edges.

In the plenum, the resolution is coarsened with a constant stretching of around 6% in all spatial directions, cf. Fig. 5.3, following the explicit geometrical law described in App. A.2. The computational domain contains about 33, 1.5, and 3.2 million cells grouped in 46, 10, and 34 blocks above the plate, inside the holes, and in the plenum, respectively.

Due to geometrical restrictions, the individual blocks differ in their number of cells. Also, the number of surface cells cannot be minimized to the theoretical minimum (being that of a cube). Both facts are disadvantageous for the parallelization because they cause load

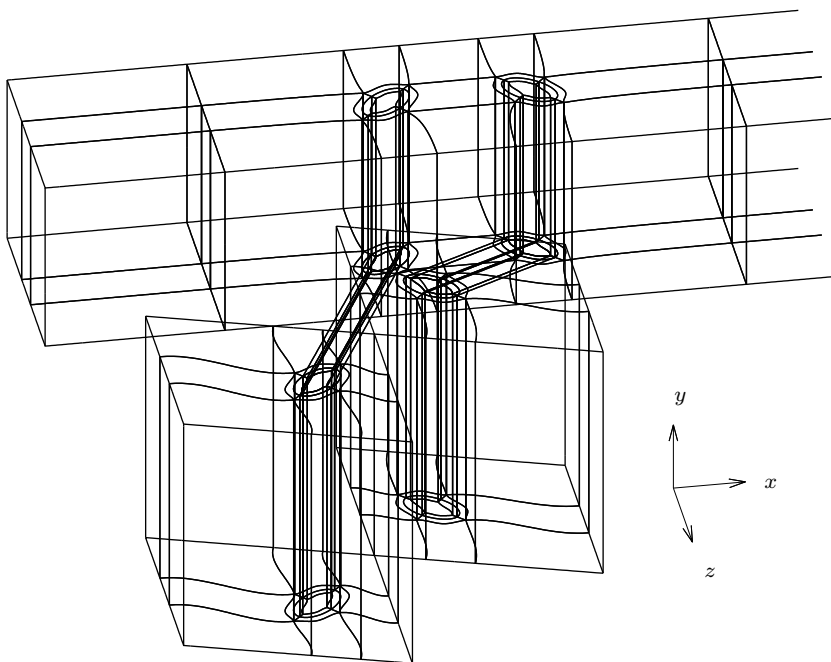


Figure 4.5: Unstructured block-grid.

imbalances or unnecessary communication. The imbalances would make most processors standing idle while only few were working. Therefore, the grid is optimized for a certain number of processing units, here 32.

4.1.3 Quasi-steady state

The sampling of the statistics starts after the temperature and mass-flux at the ejection positions keep fluctuating around a constant mean. Figure 4.6 shows the blowing ratio M and the temperature $T_{t,c}/T_r$ averaged over the coolant ejection areas individually. The temperature is normalized by the coolant's total temperature $T_{c,t}$ and the plate boundary-layer recovery temperature T_r for better comparison with the low Mach number experiments with $T_r \approx 1$. First, it can be seen from the figure that the values deviate less than 1% from their mean values. The blowing ratio M fluctuates around the desired value

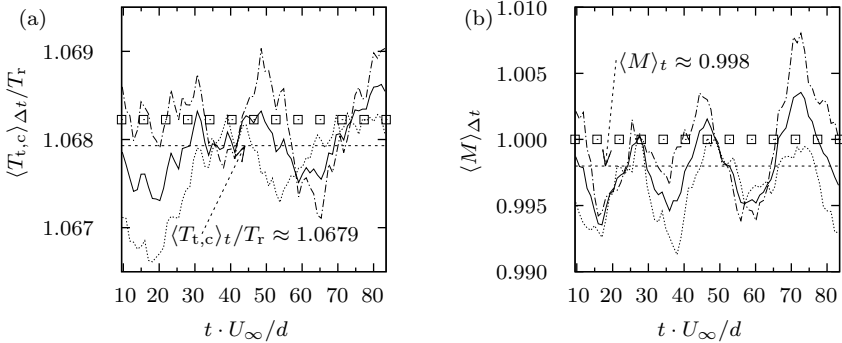


Figure 4.6: Temporal development of integral coolant properties averaged over the ejection area and window-averaged over the time period $10.5 d/U_\infty$ using a sampling step of $\Delta t \cdot U_\infty / d = 1.05$. (a): Temperature ratio $\langle T_{t,c} \rangle_{\Delta t} / T_r$; (b): blowing ratio $\langle M \rangle_{\Delta t}$. (—): Average over both ejection positions; (---): averaged over first ejection position $x/d = -4$; (···): averaged over second ejection position $x/d = 0$; (·····): mean; \square : reference experiment by Ahn et al. (2003).

with a relative amplitude larger than that of the temperature. The mass-flux oscillations might be caused by low-frequent wagging of the jet trajectories as observed in Zieffle & Kleiser (2009). Overall, the data of the individual holes do not deviate systematically from their common mean values. Finally, the maximum deviation between the simulated averages and the reference experiment is 0.2%.

4.2 Mean flow in the plenum

Table 4.3 summarizes the various vortices that will be discussed in the following sections.

The simulation of the coolant flow starts with a fictive laminar channel flow in the y -direction, as illustrated by the velocity vectors shown at the bottom of Fig. 4.7(a). Inside a real turbine blade, the coolant supply-flow in general follows the $\pm z$ -direction modified by rotational effects which deflect the flow mainly in the $\pm x$ -direction. However, as the flow approaches the holes, it is oriented towards the blade surface, in the y -direction. At this point, the presented simulation begins.

The primary flow in the plenum is characterized by the sudden contraction of a wide channel to a narrow pipe flow. In general, the field is oriented in the y -direction and is accelerated while approaching the

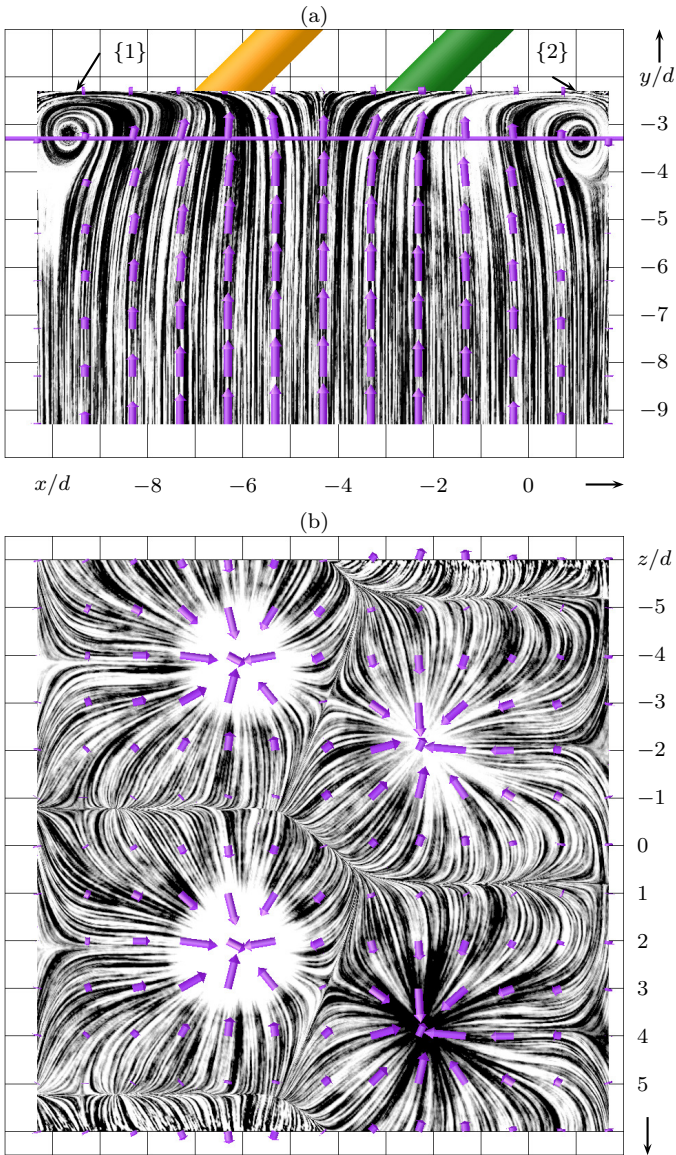


Figure 4.7: Mean primary flow in the plenum. Cross-sections at (a): $z/d = 0$; (b): $y/d \approx -3.3$ (through the corner vortex cores) periodically repeated in the z -direction. Gray-scale: LIC; (\rightarrow): velocity; (---): position of cross-section.

Table 4.3: Table of vortices. Number (No.); sense of rotation in viewing direction (dir.): clockwise (cw) or counter-clockwise (ccw).

No.	dir.	associated with	note	cf.
{1}	ccw	upstream hole	corner	Sec. 4.2
{2}	cw	downstream hole	corner	Sec. 4.2
{3}	n/a	plenum, both holes	torus	Sec. 4.2
{4}	cw	both holes	separation	Sec. 4.3.1
{5}	cw	upstream hole	principal	Secs. 4.3.2 and 4.4
{6}	ccw	downstream hole	principal	Secs. 4.3.2 and 4.4
{7}	ccw	upstream hole	degenerated	Secs. 4.3.2 and 4.4.4
{8}	cw	downstream hole	degenerated	Secs. 4.3.2 and 4.4.4
{9}	cw	upstream hole	secondary	Secs. 4.3.2 and 4.4.4
{10}	ccw	downstream hole	secondary	Secs. 4.3.2 and 4.4.4
{11}	ccw	upstream hole	secondary	Secs. 4.3.2 and 4.4.4
{12}	cw	downstream hole	secondary	Secs. 4.3.2 and 4.4.4
{13}	cw	upstream hole	horseshoe	Sec. 4.4.4
{14}	ccw	downstream hole	horseshoe	Sec. 4.4.4
{15}	n/a	both holes	streak	Sec. 4.5
{16}	n/a	both holes	roll up	Sec. 4.5

plenum–hole orifice, cf. Fig. 4.7. As expected intuitively, the flow is distributed in a regular fashion among the individual holes, see Fig. 4.7(b).

The secondary flow reveals two different systems of structures: the corner {1,2} and the torus {3} vortices, see Figs. 4.7 and 4.8. (There are also some numerical artefacts such as the crescent {*} and the block-edge {#} structures.) In most channel contractions, a pair of counter-rotating corner vortices appears, cf. Wilcox (2000, Fig. 7.10). For the present case, these vortices are identified as {1,2} and revolve slowly. In Fig. 4.8(a), these corner vortices are sucked in towards the nearest hole following the principal flow. The velocity vectors in Fig. 4.7(b) show the acceleration of the primary flow which transports the corner vortex towards the plenum–hole orifice where it breaks up. A link to the counter-rotating vortex pair {5,6} cannot be made due to the large spatial distance. The downstream view in Fig. 4.8(b) shows that the corner vortex near the downstream hole occupies more space than the other one. This asymmetry can be explained by the inclination of the holes. The acute angle of the downstream hole causes the flow to detach earlier from the plenum

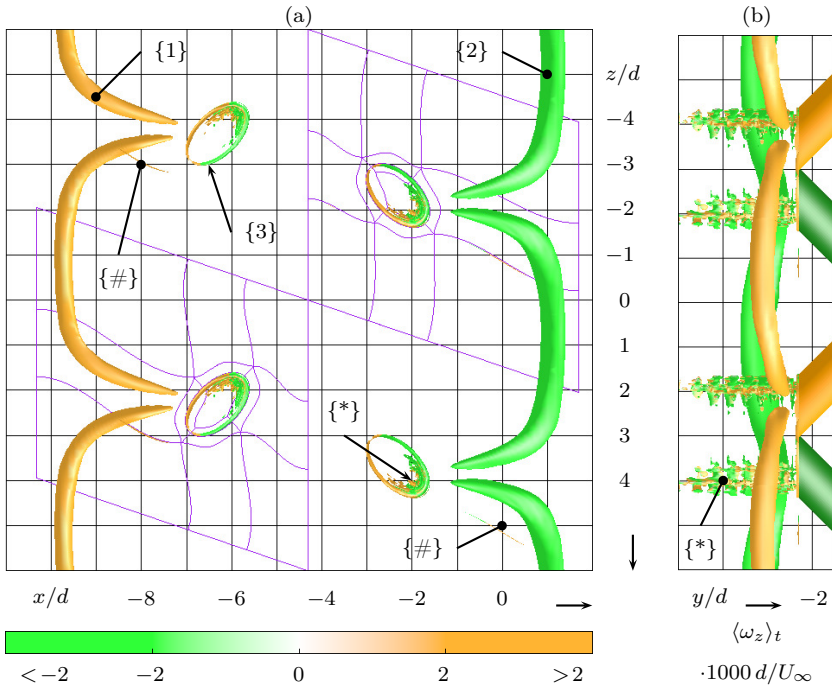


Figure 4.8: Corner vortices in the plenum. (a): Top view; (b): front view on $\langle \lambda_2 \rangle_t = -2 \cdot 10^{-4}$ surfaces colored by the spanwise vorticity $\langle \omega_z \rangle_t d/U_\infty$. (—): Block grid.

wall at $x/d \approx 1.7$, thus increasing the space available for the corner vortex.

At the plenum–hole orifices, relatively thin torus-shaped structures {3} establish themselves. The major part of them is located inside the hole. They are also reported in Ziefle & Kleiser (2008) for a simple-angle film cooling flow.

These rings partly block the view on to the crescent artefacts {*} located at the acute-angled section of the orifice ellipsis. Together with the thin structures {#} in Fig. 4.8, we consider them as numerical artefacts. They are likely caused either by locally insufficient resolution or lacking smoothness of the computational grid. The small $|\lambda_2|$ level at which the artefacts become visible suggests a small effect on the flow.

4.3 Mean flow in the cooling holes

Following the coolant flow, we first consider the upstream hole and subsequently highlight the differences to the downstream hole.

4.3.1 Flow separation and jetting region

As expected downstream of a sharp-edged inlet Wilcox (2000, Fig. 7.10), a contraction of the flow is observed in Fig. 4.9(c) which reaches its maximum in the lateral ζ -direction around $\eta_1/d = -3.75$. One might expect the largest axial velocity at the same location. This is not the case, however, (see also Figs. 4.10(m) and 4.10(q)) because the walls are not yet closed in circumferential direction, see Fig. 4.9(a). In the ξ' -direction, the strongest constriction is located around $\eta_1/d = -2$, see Fig. 4.9(a). The strongest total constriction is found at the location of the highest axial velocity around $\eta_1/d = -2.6$, see Fig. 4.10(i). In addition, the flow is asymmetric, cf. Fig. 4.9(c), which is attributed to the yaw angle. Downstream of $\eta_1/d \approx -1.5$, the flow is oriented in the ζ_1 -direction which is a consequence of the strong cross-flow momentum in the x -direction.

In the axial cross-section of Fig. 4.9(a), a large separation bubble $\{4\}$ with a recirculation zone is visible downstream of the acute-angled edge at positive ξ'_1 . At the opposite wall at negative ξ'_1 , the axial velocity is maximal, which is commonly referred to as jetting region. The flow asymmetry is caused by the inclination of the hole and the inertia of the fluid. The qualitative behavior in the downstream hole is the same as is obvious in Figs. 4.9(b), 4.9(d), and 4.10(t). Consistently, the flow is bend towards the $-\zeta_2$ -direction due to the opposite yaw angle.

Deeper insight into the flow is gained from studying transversal cross-sections as depicted in Fig. 4.10. Surprisingly, the separation bubble is not exactly located at the acute-angled boundary at $\xi'_1/d = 0.5$ but is revolved counter-clockwise by roughly 30° towards positive ζ_1 , cf. Fig. 4.10(m). Figures 4.10(e) and 4.10(i) show that this revolved state continues as we move downstream and is addressed in Sec. 4.3.2. Nevertheless, the axial velocity-field is approximately symmetric to $\zeta_1/d = 0$ close to the coolant ejection and is revolved clockwise, cf. Fig. 4.10(a). The latter revolution is caused by the strong cross-flow momentum in the x -direction.

The flow in the downstream hole, illustrated in Figs. 4.10(h), 4.10(l), and 4.10(p), shows the same revolved tendency, surprisingly also towards

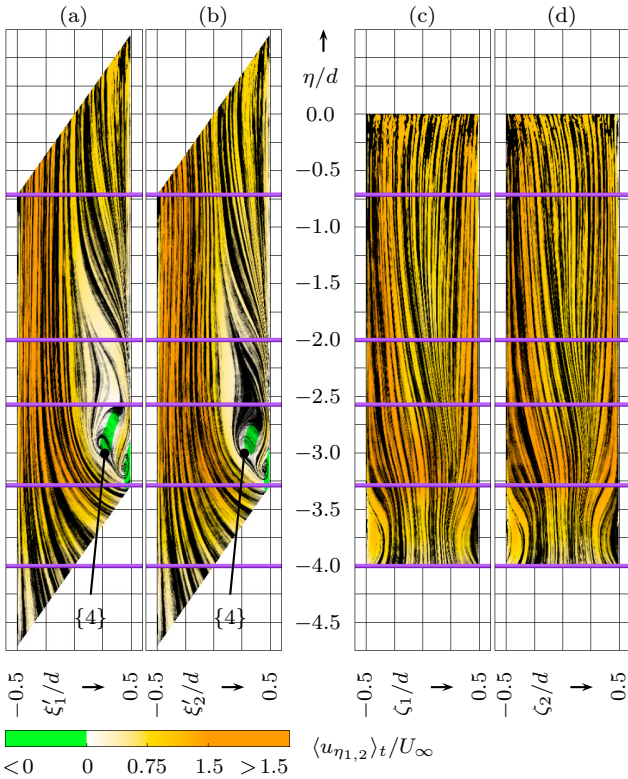


Figure 4.9: Mean velocities in the holes. LIC of (a), (b): $\langle u_{\xi'_{1,2}}, u_{\eta_{1,2}} \rangle t / U_\infty$; (c), (d): $\langle u_{\zeta_{1,2}}, u_{\eta_{1,2}} \rangle t / U_\infty$ colored by axial velocity $\langle u_{\eta_{1,2}} \rangle t / U_\infty$ in cross-sections at (a), (b): $\zeta_{1,2}/d=0$; (c), (d): $\xi'_{1,2}/d=0$. (a), (c): Upstream; (b), (d): downstream hole. (—): Positions of cross-section in Fig. 4.10.

the counter-clockwise direction. The reason may be located further upstream as explained in the discussion of Fig. 4.10(r) in Sec. 4.3.2. As expected, the downstream cross-sections of the holes exhibit mirror-symmetric tendencies depicted in Figs. 4.10(a) and 4.10(d), due to the opposite yaw angle $-\beta$.

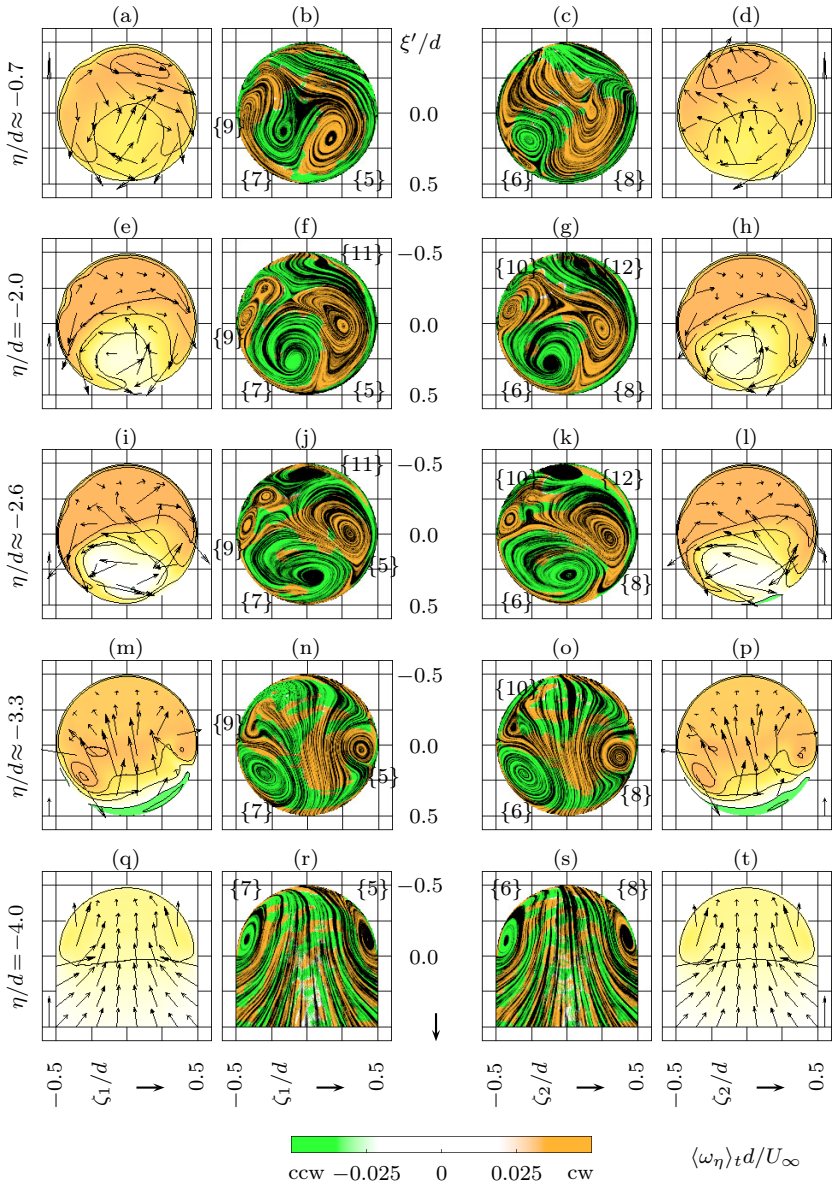


Figure 4.10: (Caption on next page)

Figure 4.10: Development of mean velocities along the hole axis. Outer columns: iso-contours of the axial velocity $\langle u_{\eta 1,2} \rangle_t / U_\infty$ (iso-levels at $-0.5, 0.0 \dots 2.0$, colorbar in Fig. 4.9) and vectors of normal velocities $\langle u_{\xi' 1,2}, u_{\zeta 1,2} \rangle_t / U_\infty$ (row-specific reference arrow at the outer side equals $0.4U_\infty$); center columns: LIC of normal velocities colored by axial vorticity $\langle \omega_{\eta 1,2} \rangle_t d / U_\infty$. Left columns: upstream hole; right columns: downstream hole.

4.3.2 Double counter-rotating vortex pair

Vortices at the edges {5,7} are clearly visible in the transversal flow inside the upstream hole in Fig. 4.10(r). They are driven by the flow entering the hole and, consequently, show opposite senses of rotation. Following the flow in the hole, a system of four vortices develops, which exhibit alternating rotational directions shown in Figs. 4.10(f), 4.10(j), and 4.10(n). This is also observed in Ziefle & Kleiser (2008, Fig. 9.d). The second counter-clockwise rotating vortex {9} (appearing as twins in Figs. 4.10(f) and 4.10(j), see Sec. 2.5.2) is stronger than its counter-part {11}. The second vortex pair {9,11} might establish itself due to the deflection of the turbulent flow as in a 90° pipe elbow, cf. Wilcox (2000, Fig. 7.14). The clockwise rotating vortex of the initial pair {5} is linked to the principal vortex of the upstream hole, due to its spatial position and rotational sense, see Figs. 4.18(k) and 4.19(b). Moreover, Ziefle & Kleiser (2008) show for a simple-angle ejection case that the origin of the kidney vortex pair is at the hole-plenum orifice.

The revolved flow, described in Sec. 4.3.1, is visible more clearly in Figs. 4.10(b), 4.10(f), 4.10(j), 4.10(n), and 4.10(r). Moreover, the LIC plots in Fig. 4.10(r) suggests that the initial negative $u_{\zeta 1}$ velocity component near $\xi'_1/d = -0.5$ causes the overall counter-clockwise revolution of the flow.

In the downstream hole, the transversal flow is similar up to $\eta_2/d = -2$, cf. Figs. 4.10(c), 4.10(g), 4.10(j), 4.10(k), 4.10(n), 4.10(o), 4.10(r), and 4.10(s). This suggests that the flow up to $\eta/d = 2$ is not affected by the opposite yaw angles β . However at $\eta_2/d = -0.7$ in Fig. 4.10(c), the counter-clockwise vortex {6} is the most intense.

To assess the importance of the secondary flow, we compare the maxima of the transversal flow to those of the axial flow. Figures 4.10(m), 4.10(p), 4.10(q), and 4.10(t) show that primary and secondary flows are at the same order of magnitude for $\eta/d \lesssim -3.3$. Further downstream, the secondary flow loses its strength which is indicated by the increas-

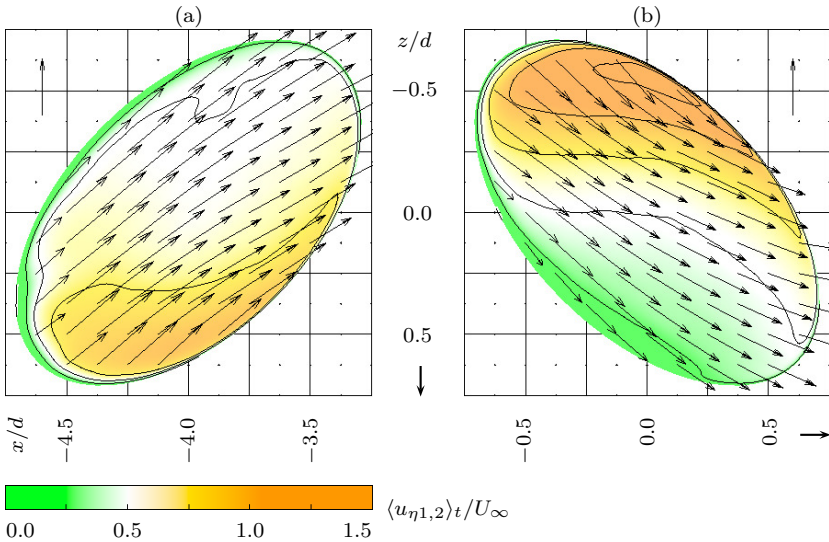


Figure 4.11: Mean velocities in the hole–plenum orifices. Iso-contours of the plate-normal velocity $\langle v \rangle_t / U_\infty$ (iso-levels at 0.25, 0.50 . . . 1.25) and vectors of plate-parallel velocities $\langle u_{1,2}, w_{1,2} \rangle_t / U_\infty$ (reference arrow at the outer side equals U_∞). (a): Upstream hole; (b): downstream hole.

ing length of the reference velocity-vectors in Fig. 4.10 with reducing η . At $\eta/d \approx -0.7$, the secondary flow is roughly one order of magnitude weaker than the axial flow, Figs. 4.10(a) and 4.10(d).

4.3.3 Mean flow in the hole–plate orifices

The mean flow at the hole–plate orifice is of special interest to some simulation approaches that neither include holes nor plenum in the computational domain. They rather use a flat plate boundary layer and generate jets by a boundary condition at the plate, cf. e.g. Bagheri et al. (2009); Linn & Kloker (2008). Figure 4.11 shows the velocities in the two hole–plate orifices.

More systematic statements can be educed from Fig. 4.12 showing velocity profiles relative to the hole axes against the orifice semiaxes ξ and ζ . The axial velocity u_η is the dominant component with a plug-like profile with an additional peak. This peak stems from the jetting region inside the holes due to its location at $+\zeta_1$, $-\zeta_2$, and

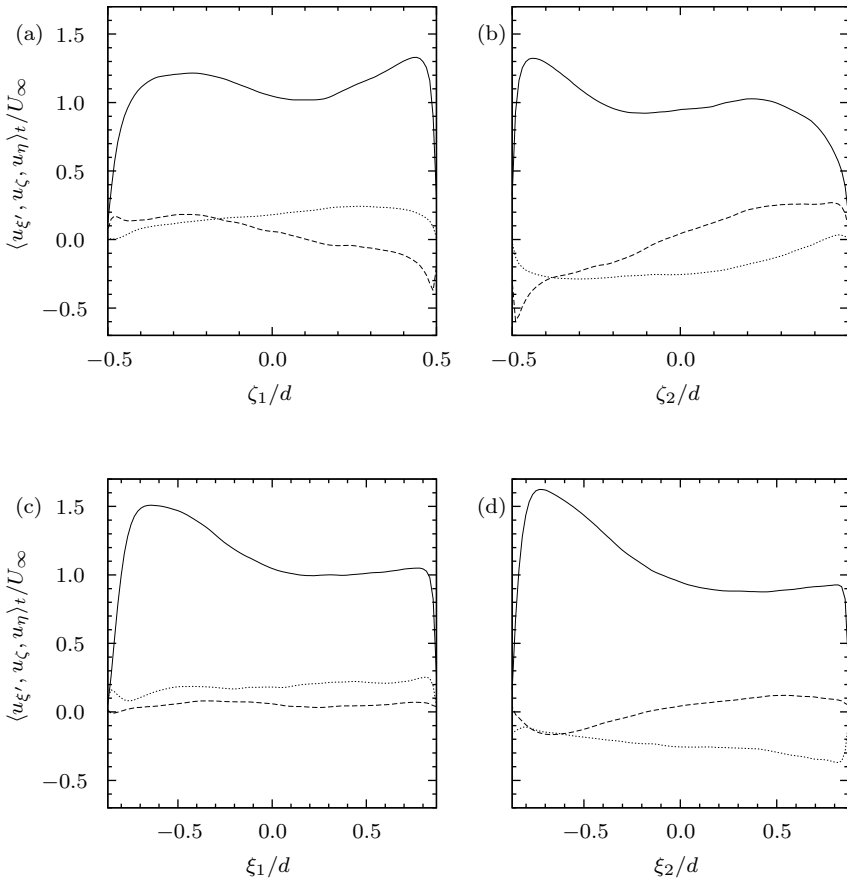


Figure 4.12: Mean velocity profiles in the hole-plate orifices against the hole-exit semiaxes. (a), (c): Upstream hole at $x/d = -4$; (b), (d): downstream hole at $x/d = 0$. Velocities relative to the hole axes (—): u_{η} , (.....): u_{ζ} , (- - -): u_{ξ}' .

— ξ . The velocities in the direction of the semiminor axes u_{ζ} are about one order of magnitude lower than the axial components. The former quantify the bending of the coolant flow in the direction of the hot gas cross-flow that is visible more clearly in Fig. 4.11. The other transverse velocity component u'_{ξ} hardly causes an overall flux in ξ' .

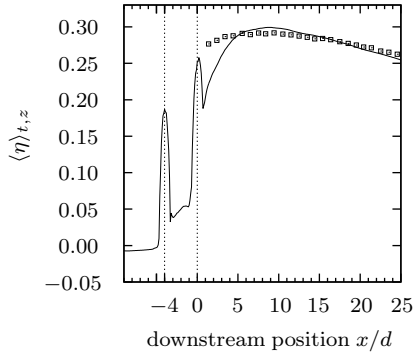


Figure 4.13: Spanwise-averaged mean adiabatic film-cooling effectiveness $\langle \eta \rangle_{z,t}$. (—): Simulation case 3b α ; □: reference experiment of Ahn et al. (2003).

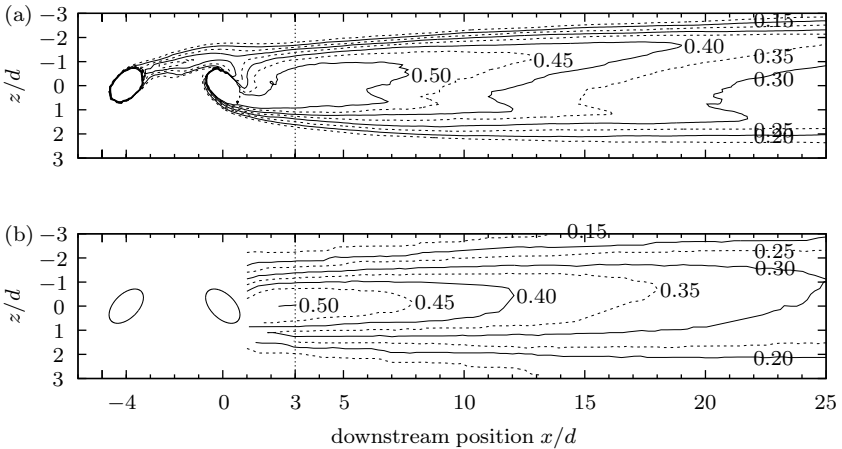


Figure 4.14: Iso-lines of mean effectiveness $\langle \eta \rangle_t$. (a): Simulation case 3b α ; (b): reference experiment of Ahn et al. (2003); (—): position of cross section of Fig. 4.15.

4.4 Mean flow above the plate

4.4.1 Comparison of cooling film with experiment

The coolant temperature for the simulation is defined to be the total temperature averaged over the cross-section area and sampling time $\langle T_{t,c} \rangle_{t,x,z} \approx 1.0749 T_\infty$.

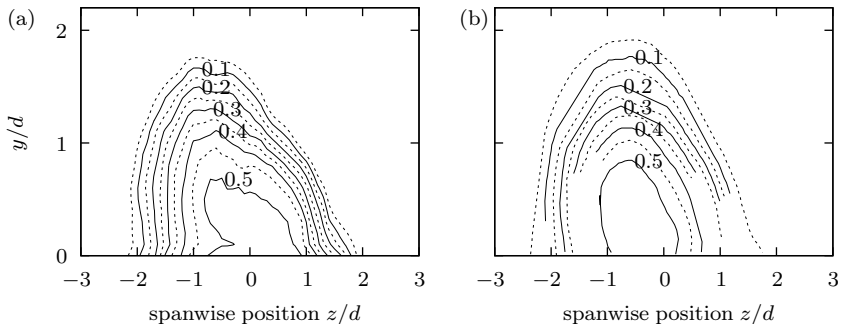


Figure 4.15: Iso-lines of mean non-dimensional temperature $\langle \theta \rangle_t$ at $x/d = 3$. Analogous to Fig. 4.14.

The spanwise-averaged effectiveness is the most important quantity indicating the achieved cooling. Figure 4.13 shows that the trend measured in the experiment downstream of the ejection can be recovered quite well by the simulation. This particular configuration shows a rather high level of effectiveness with a peak around $x/d = 7$ and a slow decrease in the downstream direction. With a maximal deviation compared to experiments of roughly 4% downstream of $x/d = 4$, the level is well predicted by the simulation. Note that the uncertainty of the experimental data for the dimensionless temperature and effectiveness is given as 5.7% and 6.8%, respectively, see Ahn et al. (2003). Larger differences are visible further upstream and for the maximum effectiveness, see Fig. 5.5. They may be attributed to different plate boundary-layer parameters, cf. Tab. 4.1.

Comparing the effectiveness distribution, the iso-contour lines of simulation and experiment illustrated in Fig. 4.14 exhibit quite similar shapes. (Note that the shapes of the effectiveness iso-lines slightly vary from one hole-couple to the next in the experiment.) Consistently, the contour lines are all bent towards the negative z -direction. Furthermore, the gradient $\partial\eta/\partial z$ obviously is larger in the simulation than observed in the experiment. This is partly compensated by the higher peak levels yielding a well-captured spanwise average.

A comparison of the non-dimensional temperature θ in a transversal yz -plane at $x/d = 3$ is presented in Fig. 4.15. The overall tilted shape of the iso-lines of simulation and experiment compare quite well. In accordance with the effectiveness, the core of the coolant ($\eta > 0.35$) shows

a larger spanwise extent and, additionally, is shifted in the positive z -direction. Also, the plate-normal extent of the iso-lines is slightly bigger in the experiment. The deviations might be attributed to the different temperature profiles due to different Mach numbers of simulation and experiment. Nevertheless, the spanwise extent of the simulated cooling film at the plate at $y/d = 0$ matches the measurement very well.

4.4.2 Heat–mass transfer analogy

The equations for heat transfer and mass transfer, described in Sec. 2.1, are similar. The selected Lewis number of unity makes the temperature and concentration quantitatively comparable. In many experiments, a different gas is chosen as coolant to generate realistic density ratios for gases at similar temperatures. The generation of large density ratios by temperature differences is usually more complicated.

The simulations presented here include the coolant concentration c . By comparison of temperature and concentration, regions of validity of the heat–mass transfer analogy may be identified. Clearly, temperature variations due to (non-)isentropic flow effects, e.g. the recovery temperature, are not present for the coolant concentration.

At first glance, the qualitative agreement of the coolant concentration and the effectiveness or non-dimensionalized temperature depicted in Fig. 4.16 is reasonable. Quantitatively, the coolant concentration underpredicts the obtained effectiveness. One reason may be the normalization procedure of the temperature, discussed in Sec. 2.5.1, which takes compressibility effects into account.

The quantitative differences are investigated at the wall and in the center-plane. For the effectiveness illustrated in Fig. 4.16(a), the underprediction by the concentration is strongest near the local peaks. The largest deviation is observed near higher peaks on the $-z$ -side, e.g. the 0.4 iso-line. The difference between the concentration in the center plane at $z/d = 0$ and the non-dimensionalized temperature is depicted in Fig. 4.16(b). The underprediction by the concentration is most evident some distance downstream the ejections and towards the freestream region of the hot gas. Effectively, the concentration seems to diffuse faster.

In the case considered here, the heat–mass transfer analogy only holds qualitatively. Quantitatively, the concentration c underpredicts the non-dimensionalized temperature. This is an extreme case, since the compressibility effects are on the order of the temperature difference.

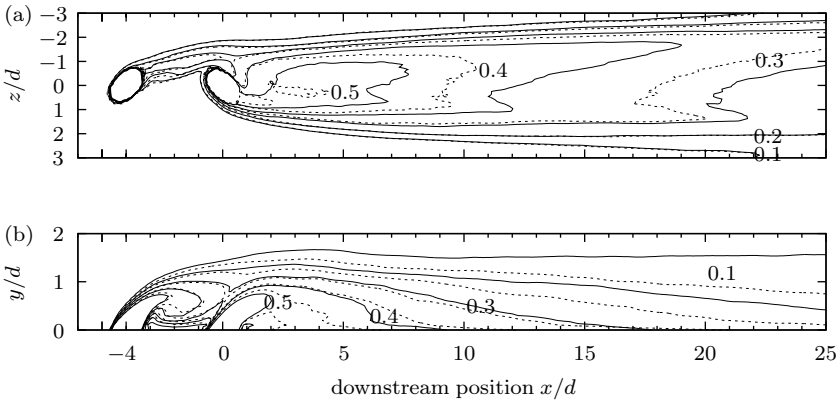


Figure 4.16: Iso-lines of (—): effectiveness $\langle \eta \rangle_t$ in (a), non-dimensionalized temperature $\langle \Theta \rangle_t$ in (b), and (---): coolant concentration $\langle c \rangle_t / c_c$. Iso-levels: 0.1, 0.2, ..., 0.5.

Therefore, the analogy is supposed to hold better for higher density ratios because the importance of the compressibility effects diminishes.

4.4.3 Anti-kidney vortex pair and effectiveness distribution

The spanwise-averaged velocity thickness $\delta_{U,95\%}$ is one characteristic measure of a boundary layer. The non-monotonic behavior of the thickness upstream of $x/d \approx 10$ in Fig. 4.17(a) clearly is a consequence of the strongly, three-dimensionally disturbed flow. Farther downstream, the thickening of the film-cooled plate boundary-layer, also reported in Bogard & Thole (2006), appears to be steady and the thickening is more intense compared to the undisturbed, turbulent plate boundary-layer of case $2b\alpha$.

Besides the thickness, tracking the trajectories of the coolant jets is of interest. Yuan & Street (1998) identified the trajectories of a generic jet-in-crossflow by different measures: streamlines, velocity maximum, and scalar-concentration maximum. For the latter two, they monitored the location of the maxima in transversal planes. First, from the streamlines, e.g. in Fig. 4.2, it is hard to choose a representative line which characterizes the path of one coolant jet. Second, the maximum velocity criterion cannot distinguish the two jets. Since the two jets stem from the same plenum, the concentration criterion also fails.

Moving on to identify the jet trajectories, the vortices come into

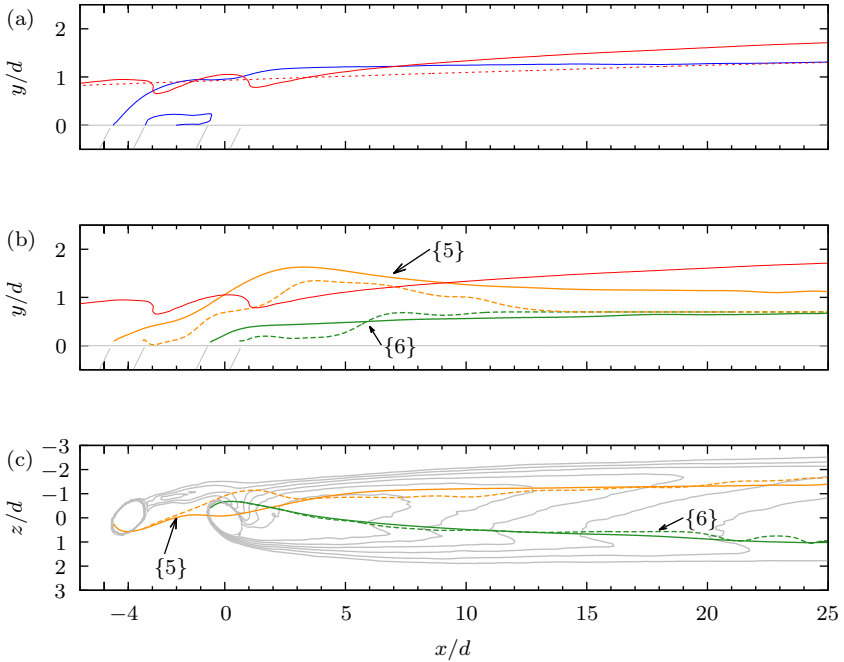


Figure 4.17: Downstream development of the mean film. (a): Spanwise-averaged plate boundary-layer thicknesses based on velocity $\delta_{U,95\%} : \langle u \rangle_{z,t} / U_\infty = 0.95$ with coolant ejection (—, case $3b\alpha$); without ejection (⋯, case $2b\alpha$); (—): based on temperature $\delta_{\theta,5\%} : \langle \theta \rangle_{z,t} = 0.05$. (b), (c): Smoothed coolant-jet trajectories of the upstream (brown) and the downstream hole (green); (—): LIC trajectory; (---): vorticity trajectory; (—): iso-lines (levels 0.25, 0.30 . . . 0.50) of effectiveness $\langle \eta \rangle_t$.

play. As introduced in Sec. 1.2, the cooling profits from the presence of an anti-kidney vortex pair. Therefore, the vortex trajectories are supposed to be congruent with the jet trajectories. The question arises, how to identify the vortices throughout the domain. In the preceding sections, the vortex identification is done using LIC, vorticity, and λ_2 criteria. Figure 4.19 shows that iso-surfaces of λ_2 quickly loose track of the vortex as it diffuses downstream.

Determining a maximum λ_2 curve in the sense of Yuan & Street (1998) does not help to distinguish the jets. However, a characteristic feature is the rotational sense, which can be identified by the downstream vorticity ω_x . Since the peak of positive or negative ω_x is

not necessarily located in the vortex core and there are some smaller vortices around, the field is integrated following

$$\omega_{x,\text{int}}(\vec{x}) = \frac{1}{\sigma^2} \int_{-\sigma}^{\sigma} \int \omega_{x,\text{clip}}(\vec{x} + \vec{x}') dy' dz', \quad (4.1)$$

$$\vec{x} = [x, y, z],$$

$$\vec{x}' = [0, y', z'],$$

using $\sigma/d = 0.4$. Between each principal vortex {5,6} and the plate, an area of strong opposite vorticity is present in Figs. 4.18(a), 4.18(c), and 4.18(k). There, the vorticity ω_x is very strong and exhibits the opposite sign due to the no-slip boundary condition. To clip this zone, the vorticity $\omega_{x,\text{clip}}$ is set to zero below the arbitrarily chosen threshold $y_{\text{clip}}/d = 0.2$.

As a second criterion, the centers of the vortex pair visualized using LIC as in Figs. 4.18(a), 4.18(c), 4.18(e), 4.18(g), 4.18(i), and 4.18(k) are determined manually. In the vicinity of the downstream ejection, the LIC does not show a circular structure for vortex {5} in Figs. 4.18(g) and 4.18(i). Most probably, the reason is that the cross-section does not cut the vortex axis perpendicularly. In such cases, the center is estimated to be at the strongest curved structure exhibiting the expected sign of the vorticity.

Figures 4.17(b) and 4.17(c) compare the results of the two above-mentioned criteria to identify the vortex trajectories. The projection in the $-y$ -direction in Fig. 4.17(c) shows larger differences only for the upstream-jet trajectories {5} in the vicinity of the downstream ejection, which might be due to the ambiguous results of the vortex core, identified by LIC in Figs. 4.18(g) and 4.18(i). The projection in the $-z$ -direction in Fig. 4.17(b) reveals that the vorticity criterion results in a trajectory closer to the plate compared to the LIC criterion. Especially for $x/d > 15$, the y -value of the vorticity criterion is the same for both jets, whereas LIC identifies the vortex core of the upstream jet {5} farther away from the plate. Figure 4.18(a) shows that both vortices are elongated in y -direction above their cores. Below the cores, this results in stronger velocity gradients and thus vorticities. The elongation of the clockwise vortex is more intense which results in a bigger disagreement between both criteria.

Interestingly, the upstream vortex {5} penetrates into the free-stream area, identified by $\delta_{U,95\%}$ in Fig. 4.17(b), only for a short

distance downstream of the coolant ejection. The downstream vortex {6} never leaves the plate boundary-layer and downstream of $x/d = 18$ both {5,6} are parallel to the plate.

The spanwise-averaged coolant film, identified by $\delta_{\theta,5\%}$, starts right at the upstream edge of the upstream ejection. After a small separation bubble downstream of $x/d \approx 0.7$, the boundary layer thicknesses based on temperature slightly overshoots $\delta_{U,95\%}$, swings back, and becomes parallel to the velocity thickness for $x/d > 20$.

Following the plate boundary-layer flow, the approaching hot gas is slightly displaced away from the plate, which is illustrated by $\delta_{U,95\%}$ in Fig. 4.17(a), due to the partial blockage caused by the upstream coolant hole. Then, coolant is ejected in the $-z$ -direction (Fig. 4.18(l)) generating a clockwise vortex {5} at the leeward edge of the orifice, cf. Figs. 4.18(i) and 4.18(k). This vortex transports hot gas towards the plate. The spanwise trajectory in Figs. 4.17(c) and 4.19(b) is tilted by $20^\circ \dots 25^\circ$ in the direction of the yaw angle β due to the effective momentum (meaning the momentum which results from the superposition of the coolant jet and the hot cross-flow). Slightly upstream of the downstream ejection, the vortex is initially displaced away from the plate, similar to the cross-flow at the upstream hole. The blockage effect by the downstream coolant widens the clockwise vortex in the spanwise direction, cf. Figs. 4.18(e), 4.18(g), and 4.18(h).

The downstream jet faces this disturbed flow field. The effective momentum causes the counter-clockwise vortex {6} to be tilted by roughly -10° with respect to the cross-flow (Figs. 4.17(c) and 4.19(b)). The magnitude of the deflection of the downstream vortex is smaller due to the already positively tilted disturbed flow.

Farther downstream, the clockwise (when viewing in the $+x$ -direction) vortex {5} is revolved around the counter-clockwise vortex {6} due to the induced velocity of the latter (Figs. 4.18(c), 4.18(e), and 4.18(g)). Finally, they come to rest side by side (Fig. 4.18(a)) still exhibiting a slightly asymmetric transversal coverage, as already observed in Fig. 4.2.

Considering the coolant distribution perpendicular to the cross-flow, Figs. 4.18(d), 4.18(f), and 4.18(j) show that the temperature gradient flattens with increasing distance to the ejection. This generates a strongly asymmetric distribution in Fig. 4.18(i). The increasing reference velocity arrow in Figs. 4.18(b), 4.18(d), and 4.18(f) shows the weakening of the vortices with the downstream coordinate x . As

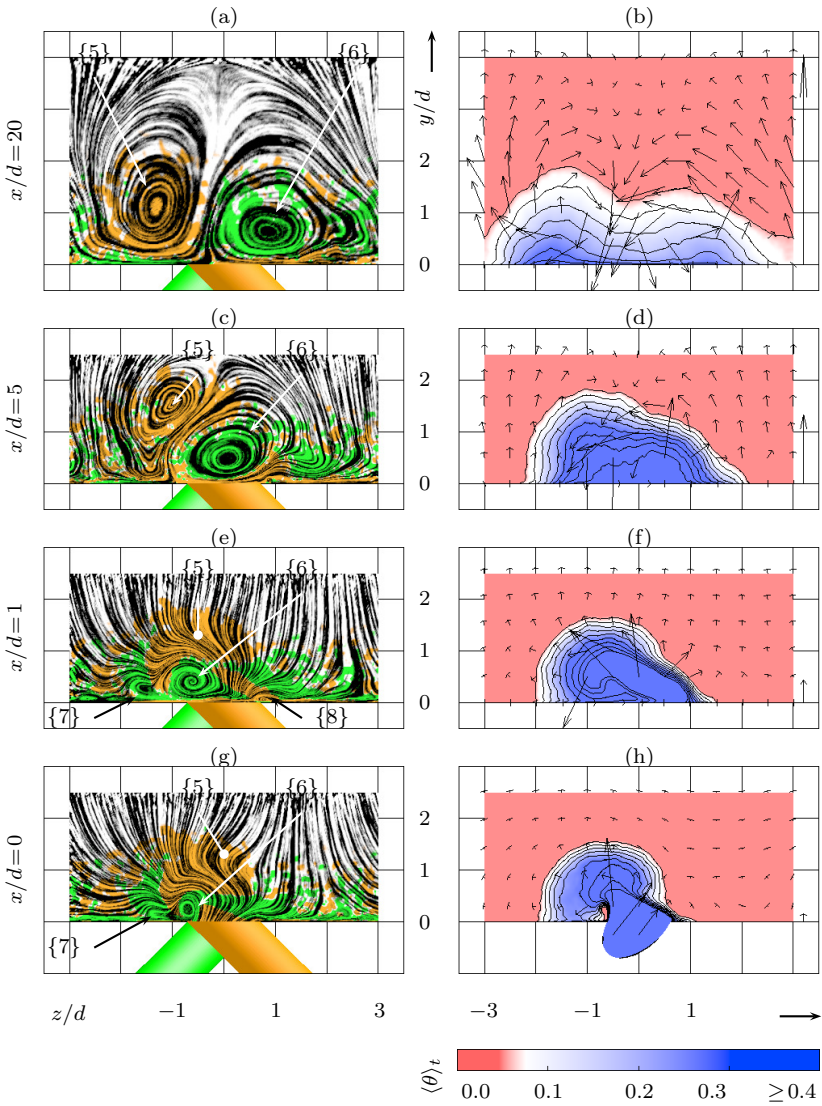


Figure 4.18: (Continued on next page)

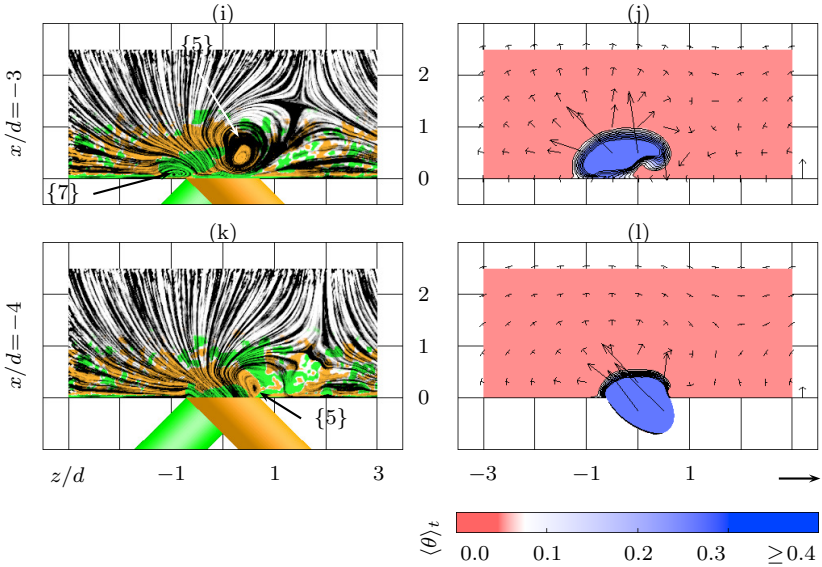


Figure 4.18: Development of the mean transversal velocities $\langle v, w \rangle_t / U_\infty$ and temperature $\langle \theta \rangle_t$. Left column: LIC colored by the downstream vorticity $\langle \omega_x \rangle_t d / U_\infty$ (colorbar in Fig. 4.10); right column: iso-contours (at levels 0.05, 0.10... 0.50) of the temperature with velocity vectors (the section-specific velocity arrow reference at outer side equals $0.15 U_\infty$).

intended, the spanwise growth of the film is more pronounced than the plate-normal one (Figs. 4.18(b), 4.18(d), and 4.18(f)). This is attributed to the rotational sense of the anti-kidney vortex pair. Close to the plate, cold fluid from the pair-interior is driven outside. This is confirmed by Fig. 4.17(c) showing cooling peaks mostly outside of the cores. Away from the plate, however, the vortex pair entrains hot fluid which creates a local minimum of cooling between the two vortices.

4.4.4 Horseshoe and degenerated vortices

Besides the anti-kidney vortex pair {5,6}, additional vortices can be identified in Figs. 4.18(g), 4.18(i), 4.18(k), and 4.19(b). One leg of the horseshoe vortex at each hole {13,14} is visible. As one moves around the leeward side of the upstream hole, four vortices with alternating rotational direction are distinguishable. The symmetric picture (spanwise broad-

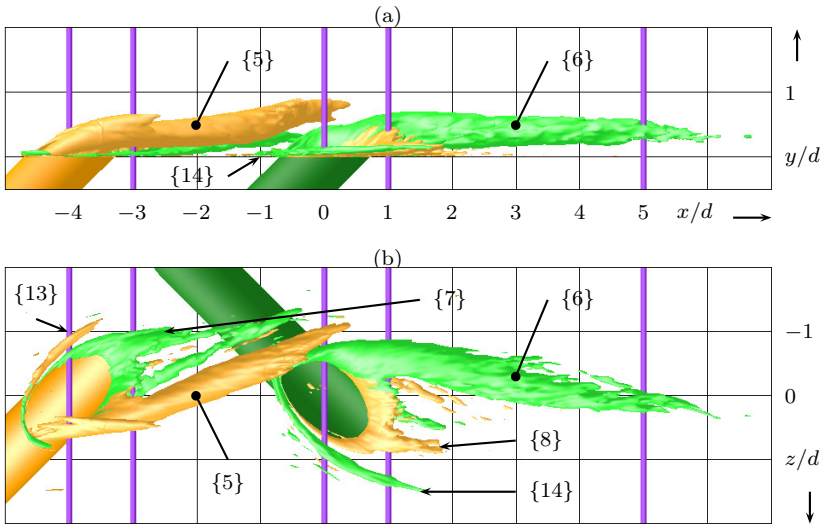


Figure 4.19: Time-averaged iso-surfaces of $\langle \lambda_2 \rangle_t = -0.5$ colored by downstream vorticity $\langle \omega_x \rangle_t d / U_\infty$ (colorbar see Fig. 4.8). (a): Side view; (b): top view. (—): Positions of cross-sections in Fig. 4.18.

ened) is obvious at the downstream hole. All four vortices are clearly visible in Fig. 4.19(b), and some can also be suspected in Figs. 4.18(e), 4.18(g), and 4.18(i); they are marked with their respective numbers.

The two small vortices (the outer one is assumed to be the degenerated one, since it is the strongest among the three weak ones) with the same rotational sense merge into one {7,8} while the remaining third small structure quickly diffuses. This scenario is more obvious for the upstream hole and, probably, develops in a more elongated manner at the downstream hole. While the principal vortices detach from the plate, the degenerated one remains attached, as observed in experiments of single-row compound-angle cooling by Aga et al. (2008).

4.5 Instantaneous flow and generalized vorticity

Figure 4.20 depicts instantaneous vortical structures. Starting just downstream of the inflow sponge, the bottom view of Fig. 4.20(a) shows streaky structures, whereas the side view of Fig. 4.20(b) reveals

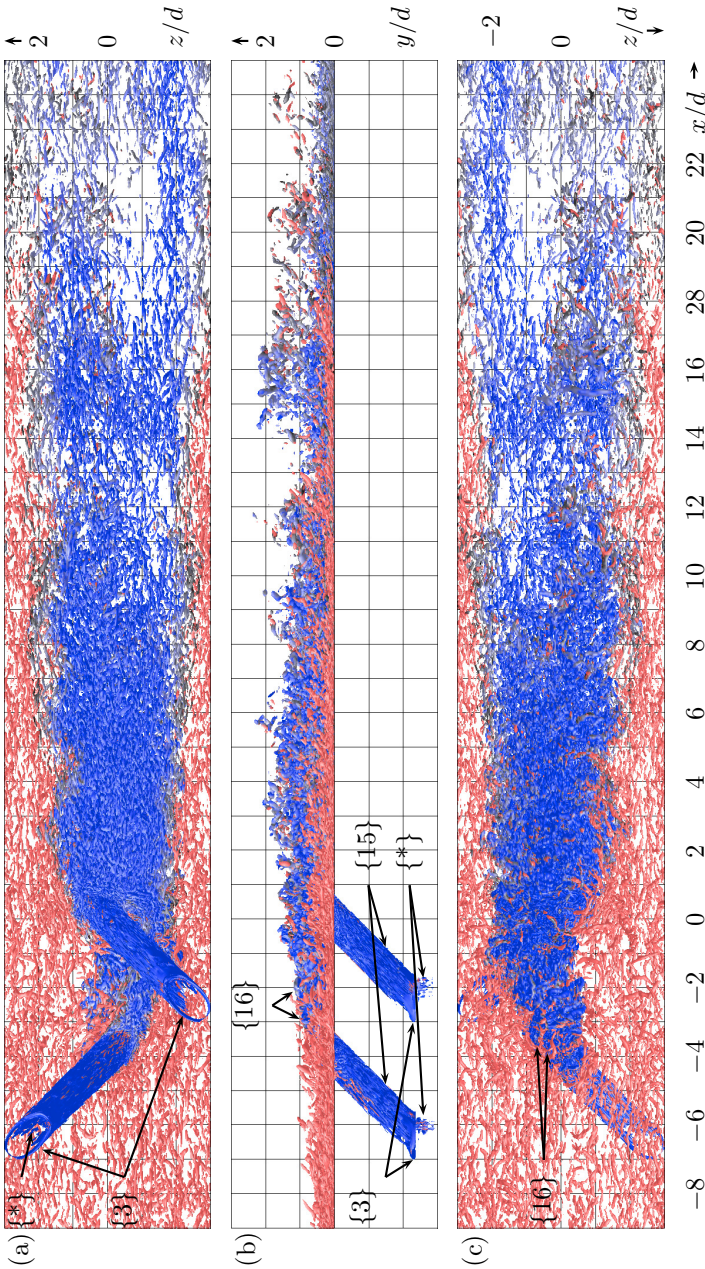


Figure 4.20: Instantaneous flow. Iso-surfaces of $\lambda_2 = -1.5$ colored by temperature Θ (colorbar in Fig. 4.18, using black instead of white). (a): Bottom view; (b): side view; (c): top view. Zones showing no instantaneous activity ($|y|/d > 3$) and sponges were clipped.

hairpin-like vortices. Both are characteristic for turbulent boundary layers, see Robinson (1991). The plate boundary-layer vortices seem to pile up on the $-z$ -side upstream of the upstream hole due to the partial blockage by the coolant, cf. Fig. 4.20(c). On the other side, they are transported underneath the coolant jet as can be seen in Fig. 4.20(a).

Figure 4.21 shows the stronger and strongest vortices identified by the λ_2 criterion and by pressure iso-surfaces, respectively, emphasizing the vortices in the area of the coolant ejection. Just upstream of the plenum–hole orifices, the weak crescent artefacts $\{*\}$ (see Fig. 4.8) and torus $\{3\}$ vortices emerge, cf. Fig. 4.20(b) and Sec. 4.2. Downstream of the orifice, the separation bubble appears as a zone of depression. Next, strong (Fig. 4.21(c)) and weak (Figs. 4.20(a) and 4.20(c)) streaky structures $\{15\}$ develop and break up near the hole–plate orifice. At the origin of the shear-layer between the approaching flow and the coolant, roll-ups $\{16\}$ develop which are characteristic to jets-in-crossflow, cf. Bagheri et al. (2009); Fric & Roshko (1994). The roll-ups follow the shear-layer being attached to the principal vortex at one side and getting weaker at the other. Downstream of roughly $1.5d$, they detach from the principal vortex and diffuse, cf. Fig. 4.21(b). Repetitious accumulations $\{16\}$ which are probably a result of the roll-ups can be suspected in Fig. 4.20(c). However, hairpin vortices stemming from the detaching legs of the horseshoe vortex, as shown in Ziefle & Kleiser (2008, Sec. 3.1), are not found. A reason for that may be the lacking second leg of the horseshoe. The vortical structures in the vicinity of the two hole–plate orifices are similar although they showed distinct peculiarities due to a different effective approaching flow.

The plate-normal region filled with vortical structures in Fig. 4.20(b) thickens considerably due to the coolant ejections up to $x/d \approx 5$. Downstream of $x/d \approx 10$, the coolant vortices become streakier due to weaker principal vortices. In the same region, the vortical structures show gaps at $x/d \approx 13$ and 21 as well as accumulations at $x/d \approx 16$ which may be a result of the roll-up merging into bigger, less intense spanwise packages which travel downstream. Moreover, the package heights indicate an increasing thickness of the plate boundary-layer.

4.5.1 Frequency analysis

The roll-ups $\{16\}$ obviously appear periodically which may be further investigated by a frequency analysis, as discussed in App. A.3.

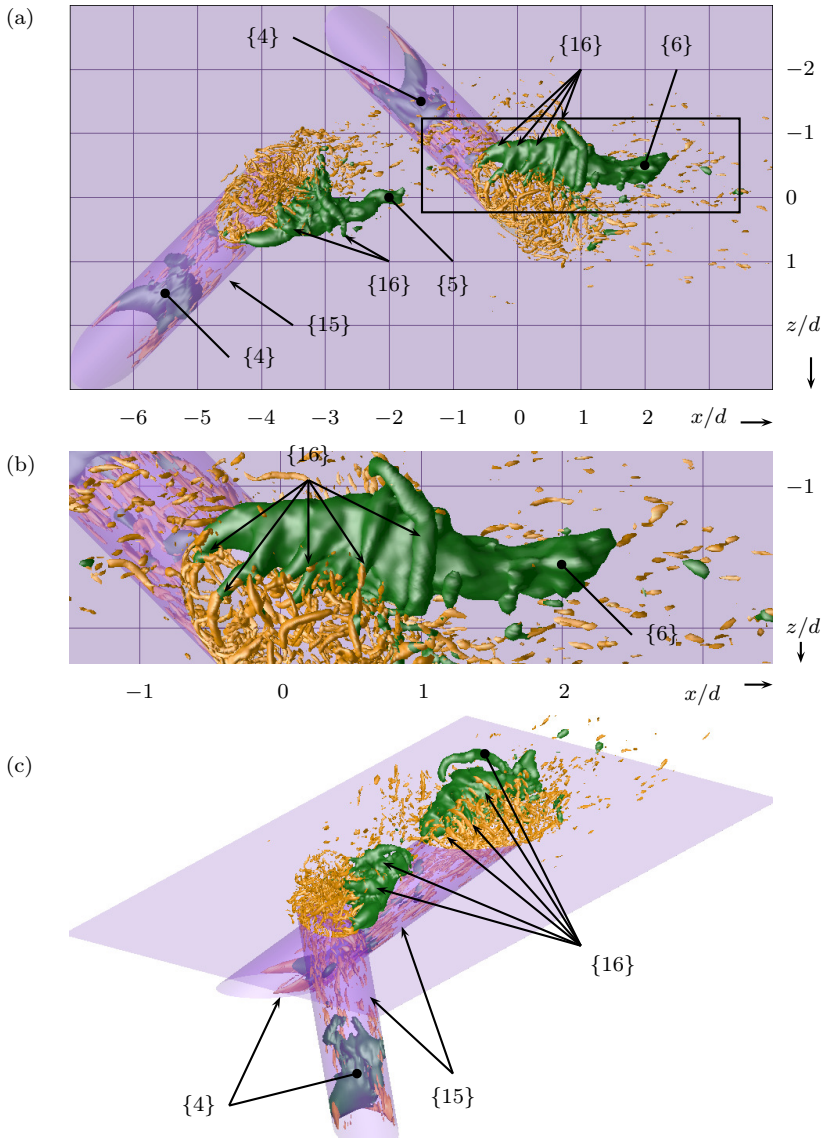


Figure 4.21: Instantaneous flow in the vicinity of the coolant ejection positions. **Brown:** iso-surfaces of $\lambda_2 = -30$; **green:** of $p/p_\infty = 0.9828$. (a): Top view; (b): magnification; (c): oblique view. Opaque purple: holes and plate.

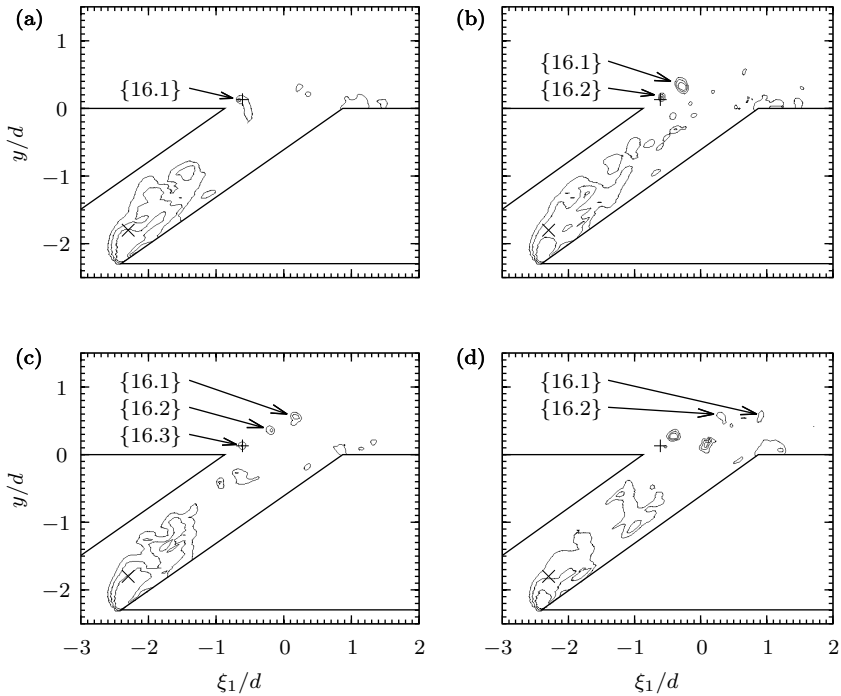


Figure 4.22: Snapshots of pressure iso-lines with a temporal spacing of $0.65065 d/U_\infty$ as marked in Fig. 4.23(a). Iso-levels: $p/p_\infty = 0.976, 0.983, 0.990$. +: Sampling position of Figs. 4.23(a) and 4.23(b) and \times : Figs. 4.24(a) and 4.24(b).

The boundary layer inside the holes is modified by the hot crossflow when the coolant is ejected. The resulting shear layer creates periodically detaching vortical structures termed roll-ups. These comparably strong vortices are identified by pressure iso-values in Fig. 4.21 {16}. Accordingly, pressure iso-lines are shown in Fig. 4.22 in four snapshots with constant time offset. The birth and transport of three roll-ups, {16.1} to {16.3}, near the upstream hole injection is depicted. The third structure {16.3} is not visible in Fig. 4.22(d) since it moved out of the section plane at $\zeta_1/d = 0$. The birth frequency estimated by the time offset of the snapshots is approximately $1.54 U_\infty/d$.

The pressure signal is sampled at the just identified birth positions of the roll-ups. A somewhat regular signal surrounding the time instances of the snapshots is obvious in Fig. 4.23(a). The Fourier transform of this

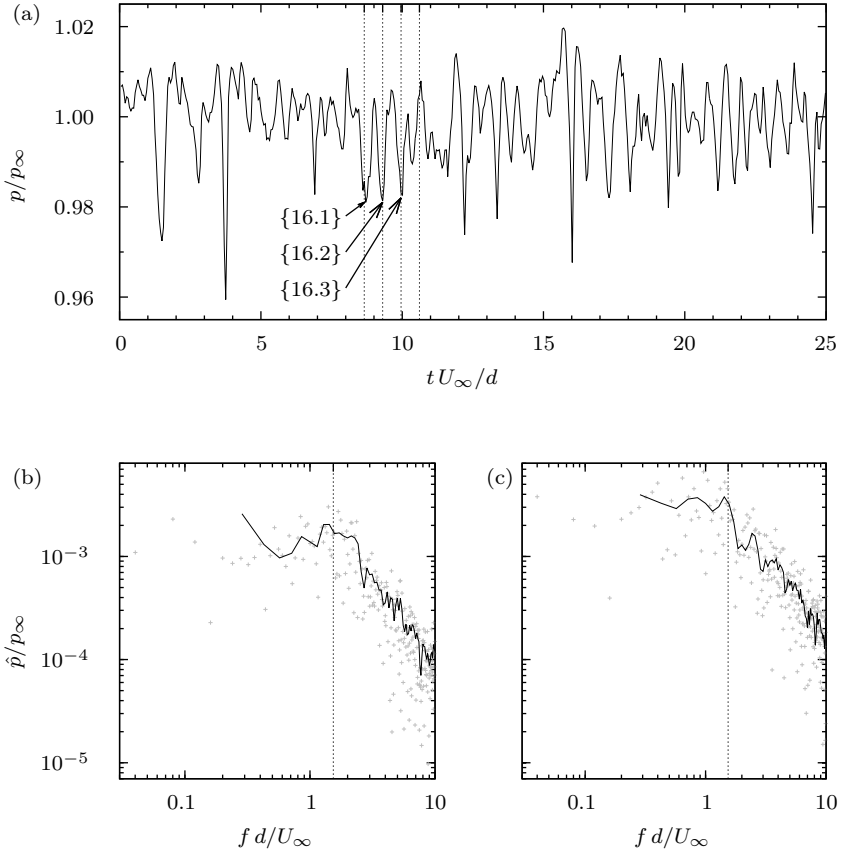


Figure 4.23: Instantaneous pressure, sampled every $0.05005 d/U_\infty$. (a): Original signal p near upstream hole injection at $[\xi_1, y, \zeta_1]/d = [-0.61, 0.13, 0]$ as indicated in Fig. 4.22. (b), (c): Discrete Fourier transform \hat{p} and (—): transformation averaged $\langle \hat{p} \rangle_{\text{Hann}}$ over 37 overlapping Hann windows with a width of $7.007 d/U_\infty$. (b): Near upstream hole injection; (c): near downstream hole injection at $[\xi_2, y, \zeta_2]/d = [-0.61, 0.13, 0]$.

signal in Fig. 4.23(b) (see caption) shows a peak close to the frequency estimated by the snapshots. A comparison with the analogous results at the downstream hole does not show qualitative differences.

There is another periodic process which is the inflating and deflating of the separation bubble [4]. Repeating the same procedure as for the roll-ups reveals a dominant frequency of roughly $1 U_\infty/d$ as is obvious

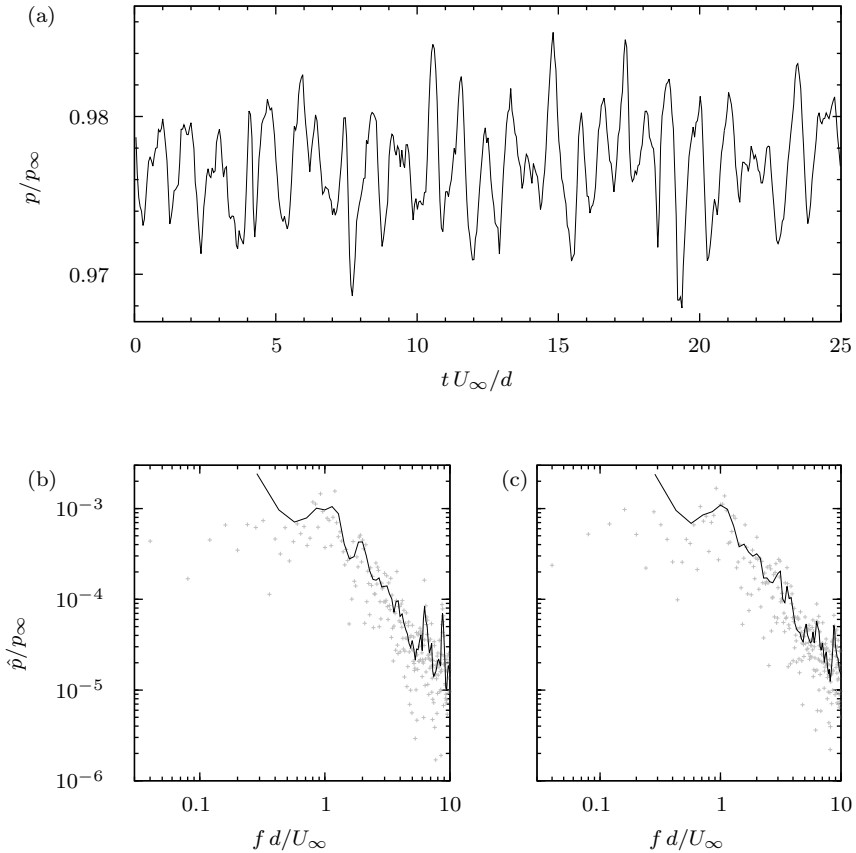


Figure 4.24: Instantaneous pressure in the separation bubble at $[\xi_{1,2}, y, \zeta_{1,2}]/d = [-2.3, -1.8, 0]$, analog to Fig. 4.23.

from Fig. 4.24. This frequency is confirmed by comparing Figs. 4.22(a) and 4.22(c) vs. Figs. 4.22(b) and 4.22(d) exhibiting a time offset of around $1.3 d/U_\infty$. The former two illustrations show an inflated and the latter two a deflated bubble.

4.5.2 Generalized vorticity

The transport equation for the generalized vorticity $\vec{\Omega}$, neglecting diffusive terms, reads

$$\frac{D}{Dt} \underbrace{\begin{pmatrix} \vec{\omega} \\ \rho \end{pmatrix}}_{:=\vec{S}} = \underbrace{\begin{pmatrix} \vec{\omega} \\ \rho \end{pmatrix} \cdot \vec{\nabla}}_{:=\vec{S}} \vec{u} + \frac{1}{\rho^3} \underbrace{\left(\vec{\nabla} \rho \times \vec{\nabla} p \right)}_{:=\vec{B}} . \quad (4.2)$$

The production terms are denoted as \vec{S} for the vortex stretching and tilting as well as \vec{B} for the baroclinic torque.

First, the mean field is studied to identify zones of large vorticity production, which are considered based on snapshots, in a second step. The quasi-mean quantities $|\langle \vec{S} \rangle_t|$ and $|\langle \vec{B} \rangle_t|$ are computed using the mean flow field rather than computed at every timestep and averaged afterwards. Due to the non-linearity of \vec{S} and \vec{B} , $|\langle \vec{S} \rangle_t|$ and $|\langle \vec{B} \rangle_t|$ do not represent the temporal averages of the production terms, e.g. $\langle \vec{S} \rangle_t = f(\langle \phi_i \rangle_t) \neq \langle f(\phi_i) \rangle_t$.

The generation of vorticity due to baroclinic torque is negligible, since this term is more than one order of magnitude smaller than the stretching and tilting term Fig. 4.25(a). The regions of maximum baroclinic torque are found around the separation bubble, between the jetting region and hole wall and in the shear layer from the hole around the hole-plate orifice.

Most vorticity is produced in the separation bubble {4}, and between the hole walls and counter-rotating vortex pairs {5} to {8} near the separation bubble Fig. 4.25(c). The hole boundary-layer generates around one order of magnitude more vorticity than the plate boundary layer, Figs. 4.25(a) and 4.25(d). Intermediate amounts of vorticity are visualized in Fig. 4.25(b) inside the principal vortices {5,6} and in the shear-layers emerging from the holes. Maybe some more vorticity is generated between the plate and principal vortices {5,6} as well as the degenerated vortices {7,8}. The vorticity production inside the mixing region of coolant jets and hot gas is as strong as inside the viscous sublayer of the plate boundary-layer.

In a second step, the instantaneous vorticity production due to vortex stretching and tilting is examined at the location of the roll-ups {16}. Figure 4.26 shows high production at the location of the roll-ups identified in Figs. 4.22(b) and 4.22(c). We conclude that most instantaneous vorticity of the film-cooled flow is generated by the roll-ups in the shear layer. This periodic production still plays a considerable role in the mean field, although the separation bubble dominates there.

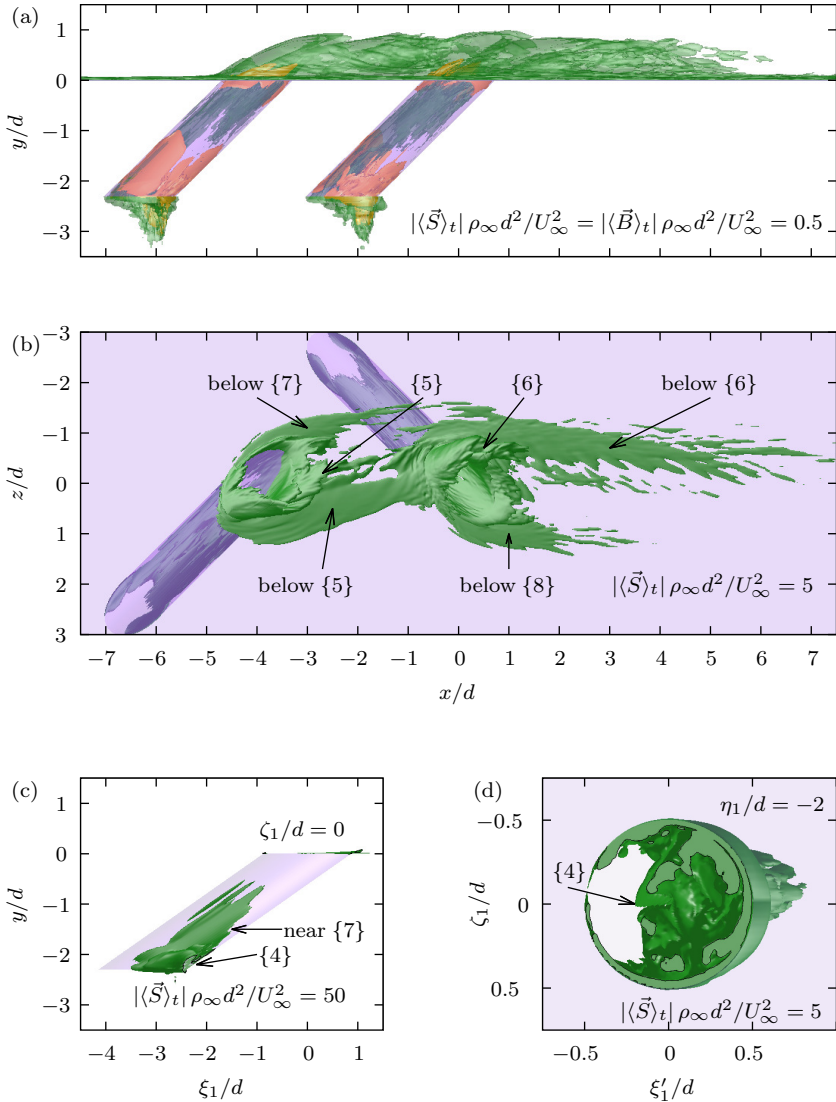


Figure 4.25: Iso-surfaces of generalized vorticity production of mean flow. Opaque purple: holes and plate; brown: $|\langle \vec{S} \rangle_t|$; (opaque) green: $|\langle \vec{B} \rangle_t|$. Iso-levels and position of cross-sections are mentioned in the figures.

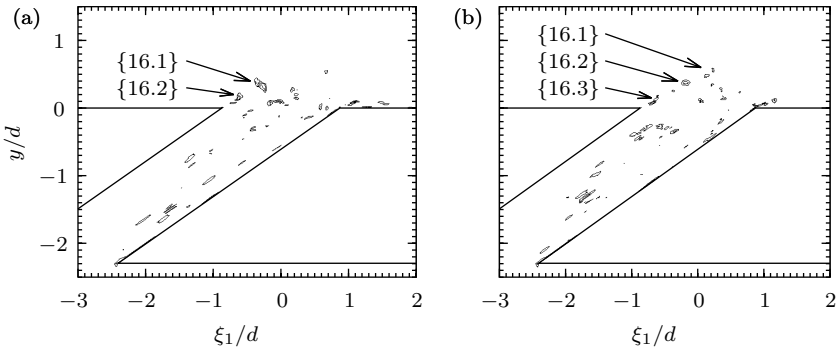


Figure 4.26: Instantaneous generalized vorticity production due to vortex stretching and tilting. Iso-levels: $|\bar{S}| \rho_\infty d^2 / U_\infty^2 = 100, 200, 500$. Same temporal and spatial positions as in Figs. 4.22(b) and 4.22(c).

4.6 Summary

A setup for LES of a double-row compound-angle film cooling configuration has been developed and validated. Case 3b β uses parameters which closely follow the reference experiment Ahn et al. (2003, conf. 1). The LES shows that the plenum inflow condition provides a mean steady state at the coolant ejection positions, and that a good match of the key quantity of film cooling, the effectiveness, as well as the non-dimensional temperature distribution in transversal planes is obtained between simulation and experiment.

In the (design-specific) edges of the plenum, we observe slowly revolving vortices which are sucked towards the nearest hole. Inside each of the holes, a system of four vortices develops: a primary and a secondary pair of counter-rotating structures. In addition, streaky instantaneous structures develop downstream of the separation bubble at the plenum–hole orifice. The streaks disappear as the coolant enters the fully turbulent plate boundary-layer. Well-known vortices of single-row compound-angle film-cooling flows are identified in the present double-row case as well.

We showed how the kidney vortex pair arises by combination of two subsequent compound-angle vortices. These strong vortices are associated with the vortex system in the holes. Two novel techniques to identify their trajectories above the plate were applied. It was shown how the resulting distribution of the film cooling effectiveness is linked

to the trajectories and properties of the vortex pair.

Most of the vorticity of the film cooling flow is produced by the separation bubble inside the holes, by the hole boundary-layers, and by the periodic shear layer roll-ups between coolant and hot gas. The heat–mass transfer analogy only holds qualitatively in this particular case, but is supposed to hold better for higher density ratios.

Chapter 5

Film cooling: application-oriented cases

This chapter approaches realistic flow parameters by increasing the density ratio to $DR \approx 2$, the mass-flux ratio up to $M \approx 2$, and the temperature level (from $T_\infty = 293\text{K}$ to $T_\infty = 1500\text{K}$). (Typical engine conditions include density ratios from 1.7 to 2.0, according to Colban et al. (2011).) We attempt to isolate the driving physical mechanisms in the different flow regions sketched in Fig. 5.1. Table 5.1 lists important parameters of all film cooling cases, whose setup is explained in Sec. 5.1. The explanation includes the boundary and initial conditions in Sec. 5.1.1 as well as the initial transient and the quasi-steady state studied in Sec. 5.1.2. Furthermore, Sec. 5.1.3 presents the computational grid along with the effect of grid resolution and grid dimensions by comparing cases $3b\alpha$, $3d\alpha$, and $3d\delta$ to $32d\delta$. From the results of Sec. 5.1.3, we conclude that the coarse resolution used is sufficient to study the effect of the parameter variation in this chapter.

Section 5.2 describes four cases $3d\alpha$, $3d\beta$, $3d\gamma$, and $31d\delta$ with varying blowing conditions. Moreover, Sec. 5.3 presents cases $31d\delta$ to $51d\delta$ with three different yaw angles to optimize the spanwise spreading of the

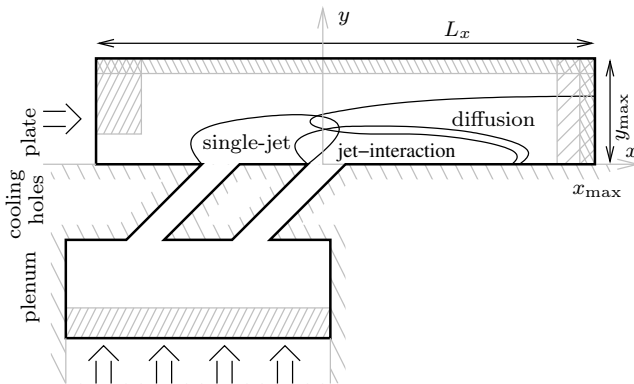


Figure 5.1: Flow regions, hatching as in Fig. 3.1.

Table 5.1: Film-cooling cases. Common parameters: non-Cartesian grid, $L_z/d = P/d = 6$, $S/d = 4$, $L/d = 4$, $\alpha = 35^\circ$. Dependent parameters: $T_\infty = 293$ K and $T_c = 313$ K for $DR = 0.9$ cases, $T_\infty = 1500$ K and $T_c = 750$ K for $DR = 2.0$ cases, 90 blocks for streamwise short grids with $x_{\max}/d = 28$, 108 blocks for streamwise long grids with $x_{\max}/d = 103$.

Symbol, case	Δy_{\min}^+	x_{\max}/d	y_{\max}/d	N_{cell}	DR	M	$ \beta $
▣ 3b α	1	28	5	$38 \cdot 10^6$	0.9	1.0	45°
□ 3d α	2	28	5	$7 \cdot 10^6$	0.9	1.0	45°
◇ 3d β	2	28	5	$7 \cdot 10^6$	2.0	1.5	45°
◇ 3d γ	2	28	5	$7 \cdot 10^6$	2.0	1.0	45°
3d δ	2	28	5	$7 \cdot 10^6$	2.0	2.1	45°
○ 31d δ	2	103	5	$14 \cdot 10^6$	2.0	2.1	45°
32d δ	2	103	10	$22 \cdot 10^6$	2.0	2.1	45°
△ 41d δ	2	103	5	$14 \cdot 10^6$	2.0	2.1	60°
▽ 51d δ	2	103	5	$14 \cdot 10^6$	2.0	2.1	30°

coolant. The impact on the achieved cooling is explained in Secs. 5.2.1 and 5.3.1 and the generated losses are studied in Secs. 5.2.2 and 5.3.2

5.1 Simulation setup

The hot gas Reynolds number displayed in Tab. 4.1 is the same for all cases, $Re_{\infty,d} = 6570$. The parameters chosen for cases 3b α and 3d α resemble the reference experiment L0 (Tab. 1.1) as closely as possible.

We choose a constant, uniform relaxation coefficient χ as small as possible for the different resolutions, so that the model drains just enough energy from the represented scales. Consequently, a fine resolution requires less energy to be drained by the model, cf. Sec. 3.1. Hence, for the fine grid used in case 3b α , a value of $\chi = 20$ is sufficient, whereas the coarse grids, used in the other cases, require $\chi = 200$.

The timestep size Δt , which is constant in each simulation, is chosen below 80% of the stability limit. The fine grid of case 3b α runs at a timestep of $\Delta t U_\infty/d = 0.00055$, whereas the coarsening by a factor of two in case 3d α doubles the timestep which is governed by the turbulent plate-normal motions in the plate boundary-layer. For the cases 3d β to 3d δ and 31d δ to 51d δ , a timestep of $\Delta t U_\infty/d = 0.0009$ is used. Typical computations of cases 3d α , 3d β , 3d γ , 31d δ , 41d δ , and 51d δ ran

Table 5.2: Initial conditions in the plenum.

Case(s)	$PR_p = p_p/p_\infty$	$DR_p = \rho_p/\rho_\infty$	T_p/T_∞
3b α , 3d α	1.069	0.982	1.089
3d β	1.060	2.149	0.493
3d γ	1.034	2.070	0.500
3d δ to 51d δ	1.128	2.224	0.507

for 111, 126, 126, 382, 280, and 280 hours on 32 NEC SX-8 processors (3552, 4032, 4032, 12224, 8960, and 8960 processor hours), respectively. Changing the blowing conditions requires an adjustment of the initial conditions and the relaxation coefficient which typically uses as many processor time as the final production run.

5.1.1 Boundary and initial conditions

The boundaries are treated in the same way as presented in Secs. 3.1.2 and 4.1.1 for cases 2b α and 3b α , respectively.

The inflow conditions to the plenum are varied to obtain different blowing conditions at the coolant injection plane at $y/d = 0$. The correct mass-flux at the injection is determined by the velocities and density at the plenum inflow. However, the temperature at $y/d = 0$, determined by the density and the pressure arising at the plenum inflow, is subject to a non-isentropic change of state due to the losses that are discussed in Secs. 5.2.2 and 5.3.2. Since the amount of these losses is unknown a-priori, the inflow data to the plenum that results in the desired data at the hole-plate orifices is also unknown. Hence, the density at the plenum inflow (that, together with the arising pressure, sets the inflow temperature) is iteratively adjusted. The initial transient is shortened by setting a meaningful pressure, which also is not known a-priori, inside the plenum. The finally used initial pressure and density values in the plenum are listed in Tab. 5.2.

5.1.2 Initial transient and quasi-steady state

The duration of the initial transient is at least 2.5 flow-through times L_x/U_∞ for all cases except for 41d δ and 51d δ . For the latter two, the quasi-steady state is reached already before 1.5 L_x/U_∞ . This is verified

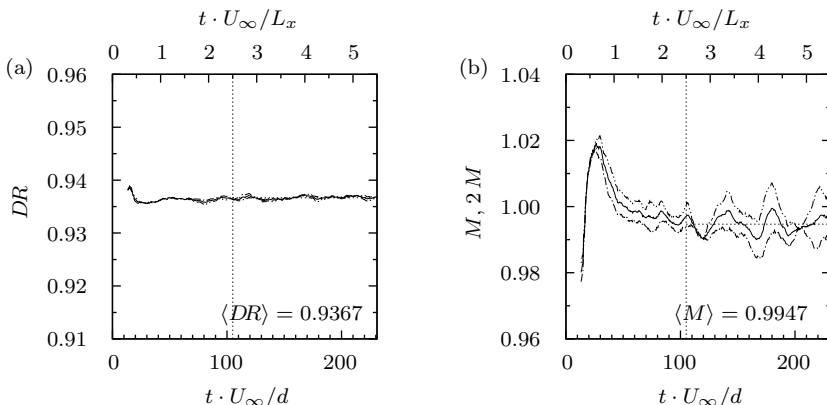


Figure 5.2: Initial transient and quasi-steady state, similar to Fig. 4.6. (a), (b): Case $3d\alpha$; (c), (d): case $3d\beta$; (e), (f): case $3d\gamma$; (g), (h): case $31d\delta$; (i), (j): case $41d\delta$; (k), (l): case $51d\delta$. (—): Average over both ejection positions; (---): averaged over first ejection position $x/d = -4$; (-·-·): averaged over second ejection position $x/d = 0$; (·····, horizontal): mean value; (·····, vertical): start of time averaging.

by case $31d\delta$ with the same domain length and a sampling time of $2.5 L_x/U_\infty$. For the time-averaged solution, every timestep is sampled for a duration of 84, 126, 109, 109, 202, 202, and 202 d/U_∞ for cases $3b\alpha$, $3d\alpha$, $3d\beta$, $3d\gamma$, $31d\delta$, $41d\delta$, and $51d\delta$, respectively, see Fig. 5.2. Case $3d\alpha$ obtained converged statistics already before $84 d/U_\infty$, so shorter periods are chosen for some other cases.

5.1.3 Computational grid and effect of resolution and dimensions

The geometrical parameters of the computational domain are depicted in Fig. 4.1. Cases $31d\delta$ to $51d\delta$ feature a long domain $x_{\max}/d = 103$ with 108 blocks and approximately $14 \cdot 10^6$ cells, compared to 90 blocks for the short domain with $x_{\max}/d = 28$. Upstream of $x/d = 25$, the grids of the short domain are nearly identical to those of the long domain.

Both cooling hole centerlines originate at the same z -position at the plate. Due to their row-wise alternating yaw angle β , the holes end up at the plenum with a notable offset in the z -direction, see Figs. 4.3(c) and 4.5, of $\Delta z_p = 2L \cos \alpha \cdot \sin \beta$. For $|\beta| = 60^\circ$, this results in $\Delta z_p/d \approx 5.7$ which is nearly as large as the spanwise pitch P . Using

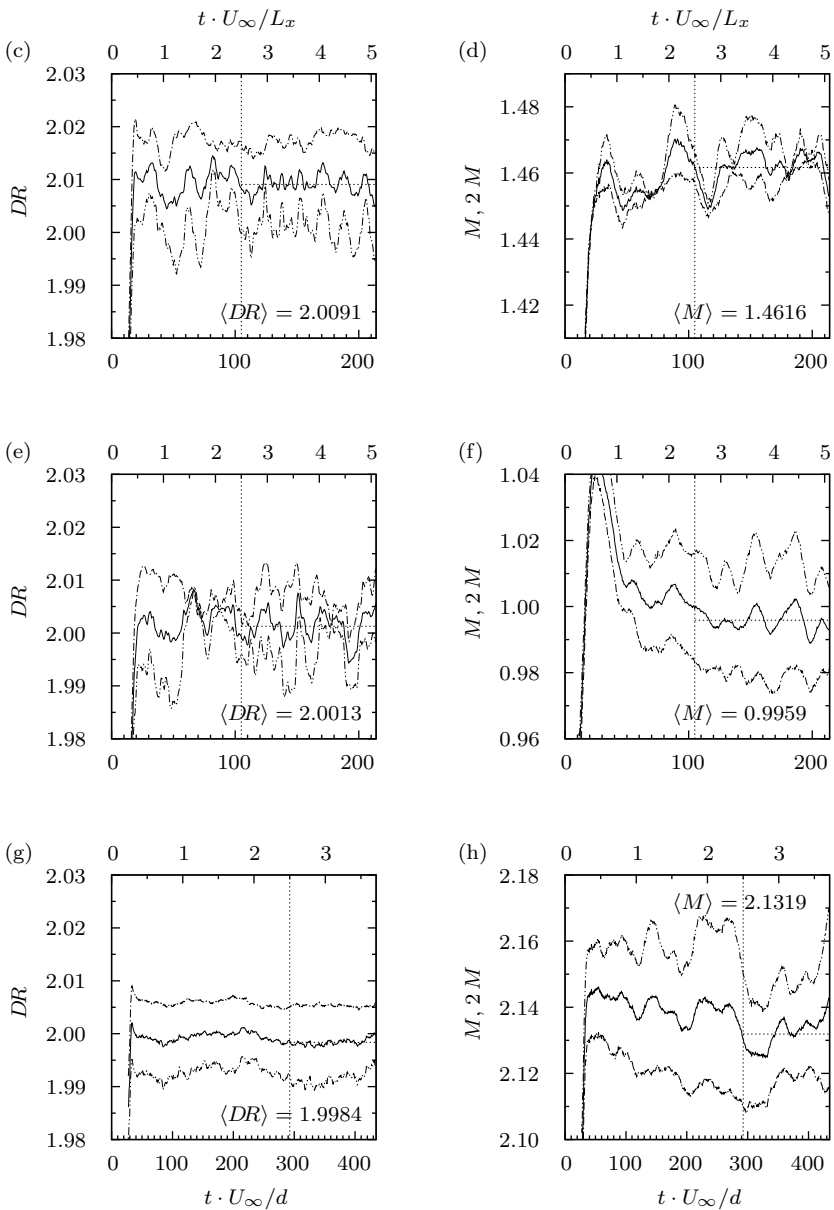


Figure 5.2: (Continued I)

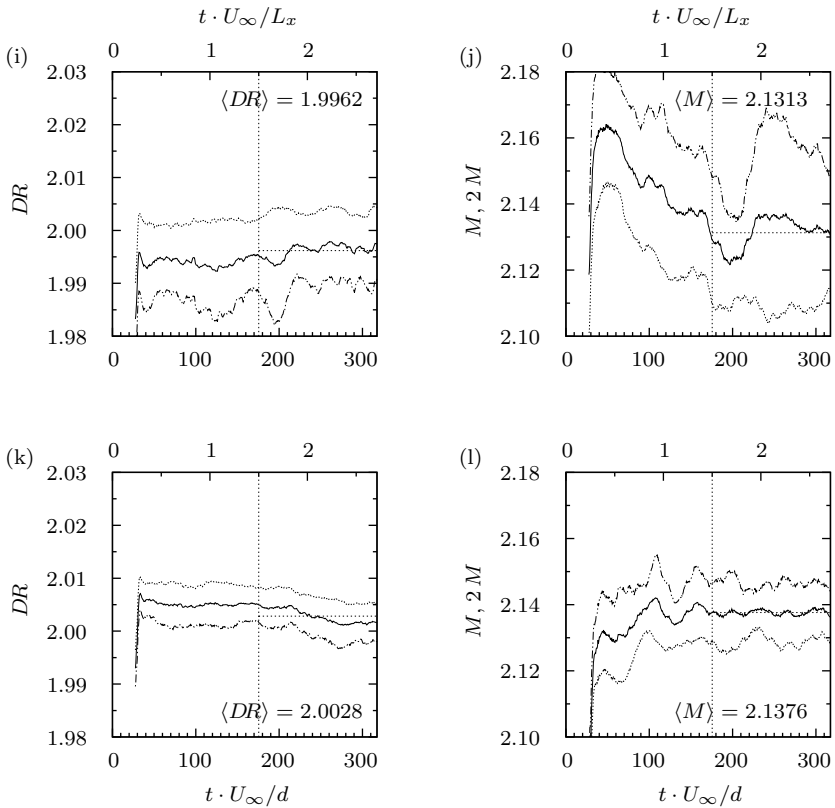


Figure 5.2: (Continued II)

one continuous, parallelogram-shaped plenum in which both holes end up would impose a large shear angle γ . This angle is depicted in Fig. 5.3 and can be expressed as

$$\tan \gamma = 2 \frac{L}{S} \cos \alpha \cdot \sin \beta - \sigma \frac{P}{S} \quad . \quad (5.1)$$

σ is the staggering parameter ranging from $\sigma = 0$ for one continuous plenum over $\sigma = 1/3$ and $2/3$ for partly staggered sub-plena, cf. Fig. 5.3(d), to $\sigma = 1$ for fully staggered sub-plena, cf. Figs. 5.3(a) to 5.3(c). These sub-plena are reconnected by block connectivity associations to represent one continuous physical plenum with infinite

Table 5.3: Cases with varying resolution; common parameters: $DR \approx 1.0$, $M \approx 1.0$, $I \approx 1.1$, $VR \approx 1.1$, $\beta = \pm 45^\circ$.

Symbol, case	cells / 10^6	Δy_{\min}^+
\square 3b α	38	1
\square 3d α	7	2

extent in the z -direction, see Fig. 5.3.

The fully staggered sub-plena for $|\beta| = 45^\circ$ result in $\gamma = -19^\circ$ as opposed to approximately 49° for one continuous plenum. Using $\sigma = 2/3$ even would result in $\gamma \approx 9^\circ$ but also imposes more restrictions on the cell numbers. For $|\beta| = 30^\circ$ and 60° , the smallest absolute shrinkage angle of $\gamma = -10^\circ$ and -5° is obtained using $\sigma = 2/3$ and 1, respectively.

We use coarsely resolved grids for parametric studies because the fine-grid simulation case 3b α is computationally very expensive. For the coarse grid, the resolution is regularly reduced above the plate by a factor of 2 in all spatial directions, cf. Δy_{\min}^+ in Tab. 5.3 and Fig. 5.4. In the cooling holes, the resolution in the xz -planes is reduced from 11044 to 2876 cells for cases 3d α to 3d δ . The resolution in the y -direction inside the plenum is not reduced, due to numerical artefacts, shown in Sec. 4.2 { $*$ }, appearing already at the fine resolution. Inside the cooling holes, the y -distribution of the cell-planes is adapted towards the coarsened resolution above the plate, retaining 69 cell-planes.

As a result, lower levels of the spanwise-averaged, minimum, and maximum effectiveness are apparent in Fig. 5.5. Nevertheless, the qualitative downstream development of these properties is independent of this grid coarsening.

Next, we checked the effect of the domain size above the plate and downstream of the coolant injections for the coarse-grid case 31d δ , cf. Tab. 5.4. Figure 5.5(b) shows little difference for the varied extents. Therefore, an above-plate extent of $5d$ is confirmed to be sufficient. Moreover, the outflow treatment does not show a significant upstream effect on the flow development.

5.2 Effect of blowing conditions

In this section, the blowing parameters are altered to approach realistic conditions, cf. Tab. 5.5. It is known, e.g. from Bogard & Thole (2006), that the interaction between coolant and hot gas scales with three

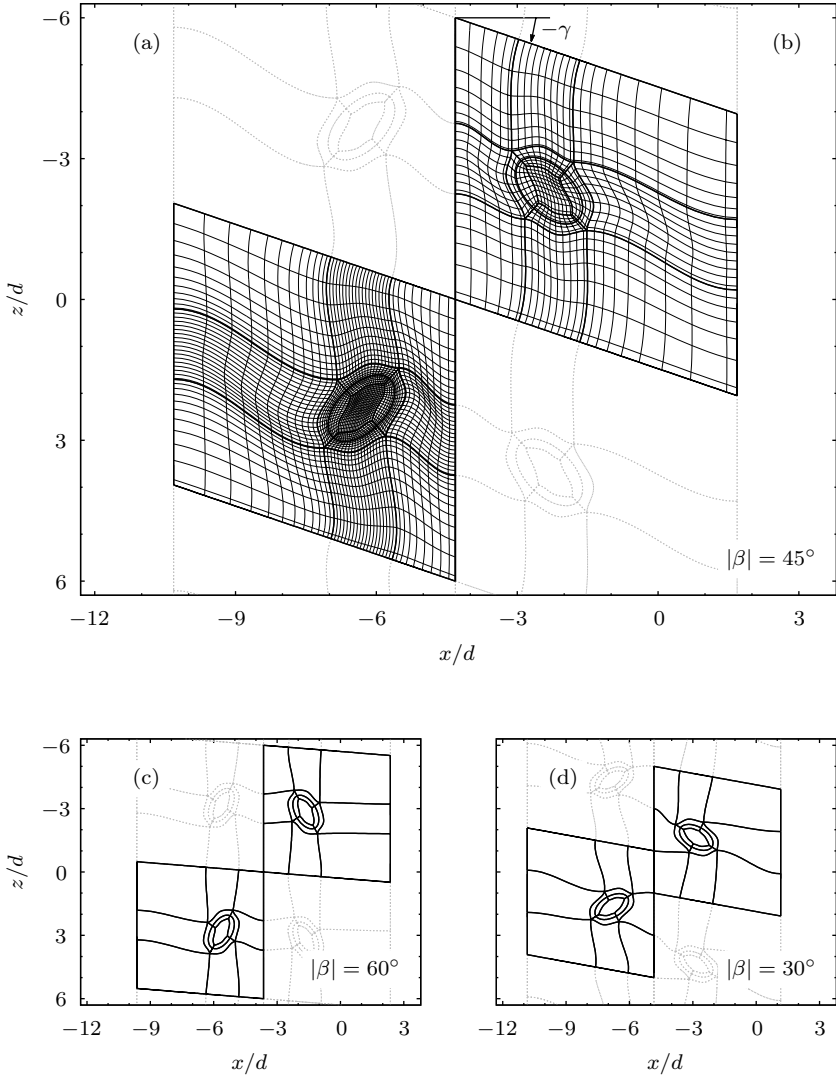


Figure 5.3: Design of sub-plena for different yaw angles. Top view on (a): case 3b α ; (b): cases 3d α to 3d δ , 31d δ , and 32d δ ; (c): case 41d δ ; (d): case 51d δ . (.....): Periodically repeated block edge; further lines as in Fig. 4.4.

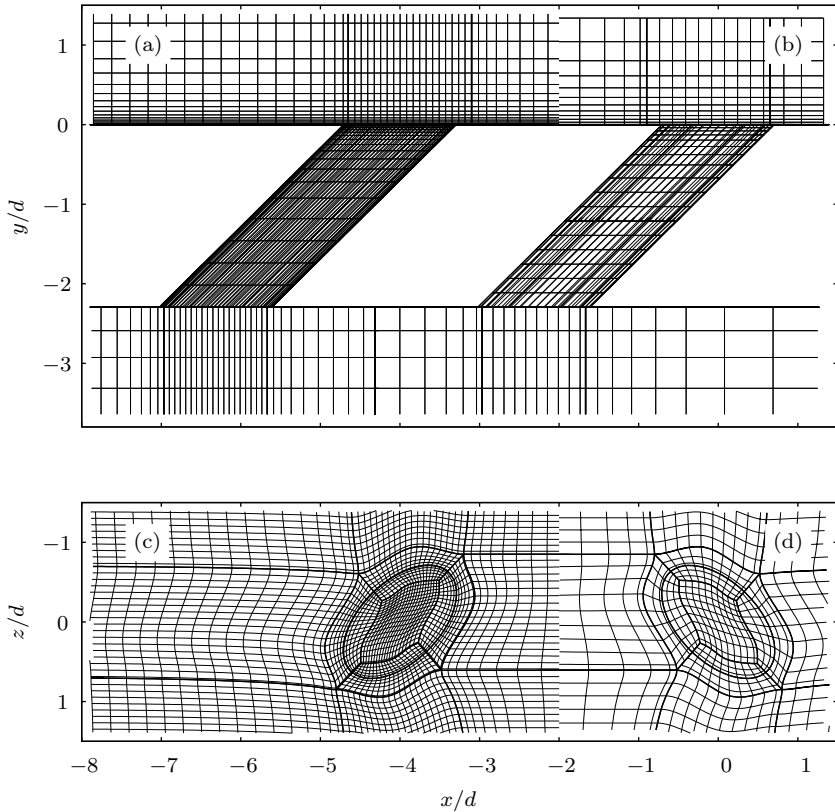


Figure 5.4: Grids for different resolutions, analog to Fig. 4.4. (a), (c): Case $3b\alpha$; (b), (d): cases $3d\alpha$ to $3d\delta$ and $31d\delta$ to $51d\delta$.

Table 5.4: Cases with varying dimensions; common parameters: $DR \approx 2.0$, $M \approx 2.1$, $I \approx 2.3$, $VR \approx 1.1$, $\beta = \pm 45^\circ$, $\Delta y_{\min}^+ = 2$.

Symbol, case	x_{\max}	y_{\max}
	28	5
○ 31dδ	103	5
	103	10

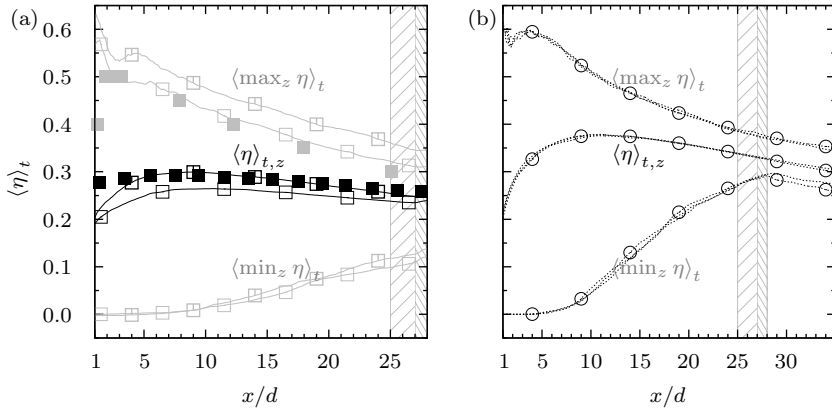


Figure 5.5: Effectiveness for different (a): resolutions and (b): domain extents. ■: Reference experiment L0 $DR = 1$, $M = 1$; □: fine LES 3b α $DR = 1$, $M = 1$; □: coarse LES 3d α $DR = 1$, $M = 1$; (·····), ○: coarse LES $DR = 2$, $M = 2.1$ 31d δ , 3d δ with $x_{\max}/d = 28$, and 32d δ with $y_{\max}/d = 10$. Analog to Fig. 5.6(a); hatching see Fig. 3.1.

Table 5.5: Cases with varying blowing conditions; common parameters $\Delta y_{\min}^+ = 2$, $\beta = \pm 45^\circ$.

Symbol, case	DR	M	I	VR
□ 3d α	1.0	1.0	1.1	1.1
◇ 3d γ	2.0	1.0	0.5	0.5
◇ 3d β	2.0	1.5	1.1	0.7
○ 31d δ	2.0	2.1	2.3	1.1

parameters: The thermal transport capacity scales with the mass-flux ratio M , the dynamic interaction with the momentum flux ratio I , and the shear layer (between hot gas and coolant) with the velocity ratio VR . Therefore, case 3d γ retains M , 3d β retains I , and 31d δ retains VR compared to cases 3b α and 3d α .

We subdivide the flow above the plate into three partially overlapping regions, sketched in Fig. 4.1, based on the presumed dominant physical mechanism: The single-jet region, where the first jet and the hot gas mix, the jet-interaction region, where the two jets mix with one another as well as with the hot gas, and the diffusion region where the coolant and the vortices diffuse.

5.2.1 Cooling at different blowing conditions

In the single-jet region downstream of the first ejection, the spanwise-averaged effectiveness shows a relationship inversely proportional to the velocity ratio, Fig. 5.6(a). The $\langle \eta \rangle_{t,z}/VR$ curves, which are not shown explicitly, even collapse in that region. The same holds just downstream of the second ejection, for all cases except $3d\gamma$. The physical reason gets clear by looking at the efficiency $\langle \eta \rangle_{t,z}/M$ in Fig. 5.6(b) where the scaling parameter is the momentum ratio. The higher the coolant momentum is, the more the coolant jet detaches from the plate, Figs. 5.7(i), 5.7(m), 5.7(q), and 5.7(u), and the lower the efficiency becomes. Such a link between momentum ratio and jet trajectory is also observed in Fric & Roshko (1994). This effect is partly compensated for by an increased coolant mass-flux, increasing the effectiveness, Fig. 5.7(a) vs. Fig. 5.7(d). Since the effectiveness scales with the velocity ratio $VR = I/M$, it hides the physical reason.

Further downstream in the jet-interaction and the diffusion regions, we exclude case $3d\gamma$ from the comparison since it does not exhibit a persistent anti-kidney vortex pair for the following reasons: First, there is a somewhat monotonic decrease of the spanwise-averaged effectiveness downstream of the second ejection of $3d\gamma$, as opposed to all other cases that show a local maximum in that region, Figs. 5.6(a) and 5.6(b). Second, the effectiveness iso-lines in Fig. 5.7(b) exhibit a more narrow, single-peak shape, since the second vortex is not strong enough to move the first towards the plate. Instead, the first vortex enters the freestream, as apparent from the vortex trajectory in Fig. 5.7(f). Consequently, the coolant from the first jet diffuses away from the plate, as indicated by the 0.1 iso-line in Fig. 5.7(f) that approximately has the same y -value as for the cases using more coolant, Figs. 5.7(g) and 5.7(h). As a result, the temperature iso-lines look like in a single-jet ejection case, Figs. 5.7(o) and 5.7(p).

At the plate, cases $3d\alpha$ and $31d\delta$ show similar patterns of effectiveness. Considering the spanwise-averaged effectiveness η and efficiency η/M , it is hard to tell whether case $3d\beta$ or $31d\delta$ is more similar to $3d\alpha$. These results can, therefore, not answer the question whether I or VR is the principal parameter determining the cooling. Moreover, the $x/(M \cdot s)$ scaling does not collapse our curves. $x/(M \cdot s)$ only becomes a similarity scaling when the diffusion region has reached the plate, which only happens in the long-domain case $31d\delta$, featuring a closed film as indicated

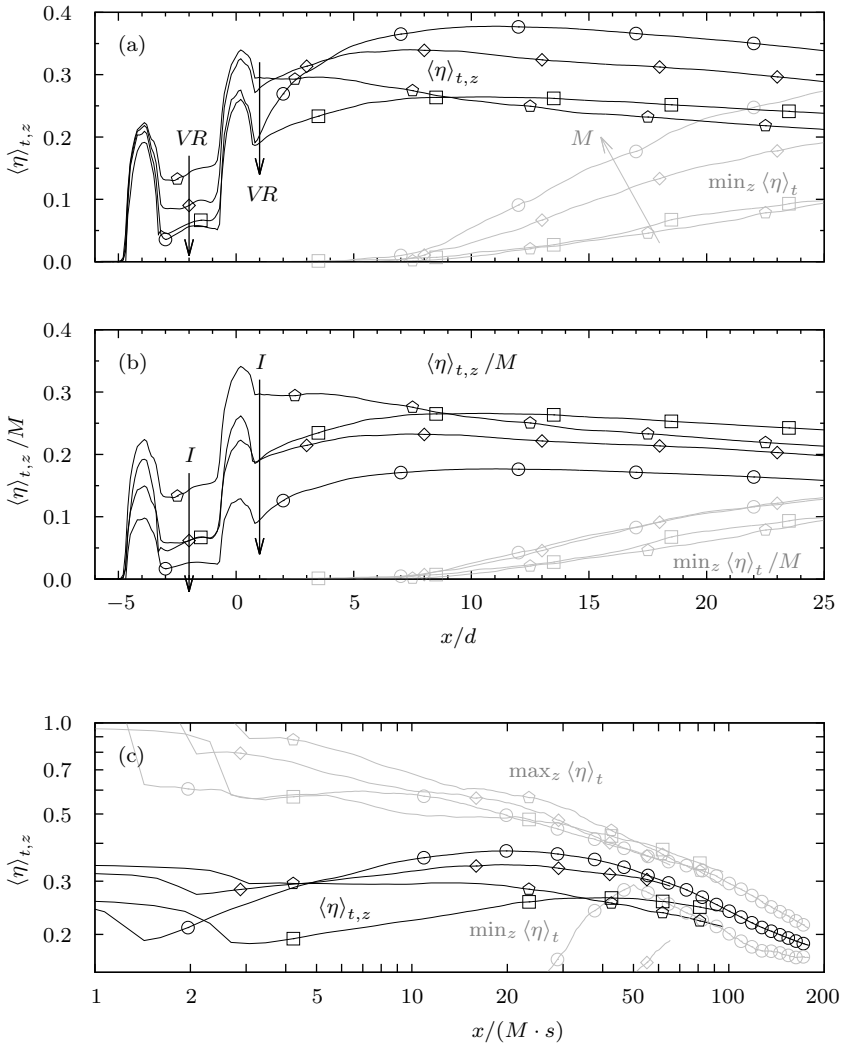


Figure 5.6: (a), (c): Effectiveness and (b): efficiency for different blowing conditions. Black: spanwise-averaged; gray: maximum or minimum effectiveness. Symbols see Tab. 5.5.

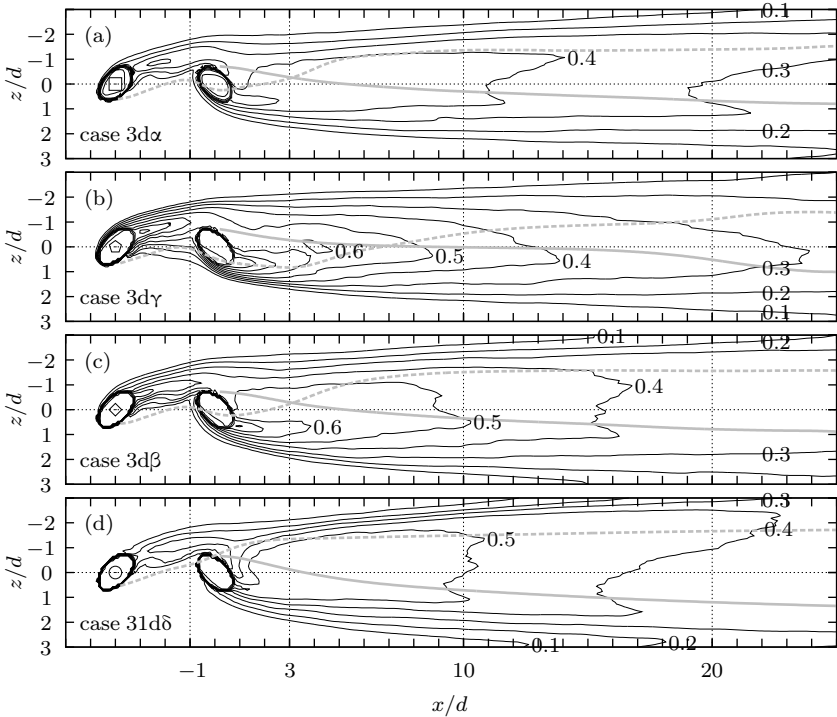


Figure 5.7: (—): Iso-lines of non-dimensional temperature for row-wise different blowing conditions, (---, —): anti-kidney vortex-pair trajectories, and (-.-): plate boundary-layer thickness $\langle U \rangle_t / U_\infty = 0.95$. (a)–(d): Top view of $\langle \eta \rangle_t$; (e)–(h): side view of centerline $\langle \Theta \rangle_t |_{z/d=0}$, note the changed aspect ratio; (i)–(x): downstream view of $\langle \Theta \rangle_t |_{x/d=-1, 3, 10, 20}$; iso-levels: 0.1, 0.2, ... 1.0.

by the minimum curves having passed their peak value, Fig. 5.6(c).

The minimum efficiency curves show similar slopes for all cases and even pairwise matching values, Fig. 5.6(b). The closing of the hot gaps in the film, indicated by a non-zero minimum effectiveness, accelerates when using more coolant, Fig. 5.6(a). We suppose that this is a combination of two effects: On the one hand, the stronger direction-preserving of the coolant jets, due to increased momentum ratio, is confirmed by considering the vortex trajectories, Figs. 5.7(a) to 5.7(d). On the other hand, the effectiveness reduction, due to increased mixing of coolant with hot gas at the interface with the film, scales with the increased velocity

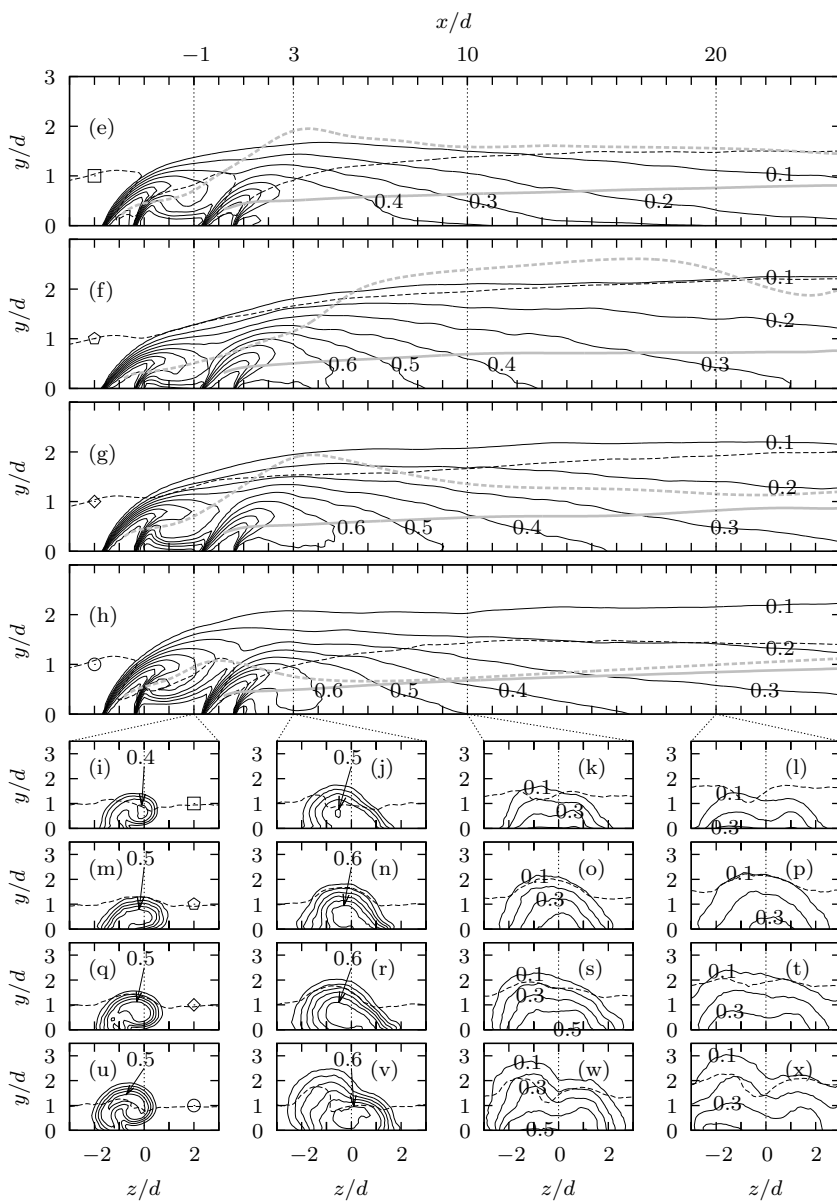


Figure 5.7: (Continued)

ratio. Consequently, the spanwise broadening of the film scales with the momentum to velocity ratio which is the mass-flux ratio $M = I/VR$.

Overall, cases $3d\alpha$ and $3d\beta$, with equal values for I , show most similarities in the temperature field above the plate, Figs. 5.7(k) and 5.7(l) vs. Figs. 5.7(s) and 5.7(t). Moreover, the strongest and most enduring vortices are found in case $31d\delta$ with the highest I , Figs. 5.7(u) to 5.7(x). Thus, we conclude that the strength and downstream endurance of the anti-kidney vortex pair increases with I .

5.2.2 Losses at different blowing conditions

The losses caused by film cooling are evaluated according to Eqs. (2.35) to (2.38) against the varied parameters M , I , and VR . For each loss coefficient, there are two cases with the same parameter and a similar loss value, i.e. two points nearly collapse, Fig. 5.8. We denote this as the principal scaling parameter. As a result, the discharge loss is the only one to scale with M , Fig. 5.8(c), while the other three coefficients scale with I , Figs. 5.8(a), 5.8(b), and 5.8(d).

Surprisingly, the hot gas total-pressure loss $\xi_{p,t,h}$ is reduced by increasing I , Fig. 5.8(a), due to the increased coolant mass-flux of higher total pressure. Note that the coolant properties are not accounted for at all in Eq. (2.35) allowing for negative $\xi_{p,t,h}$ values. Nevertheless, $\xi_{p,t,h}$ is very low compared to the mixture total-pressure loss $\xi_{p,t,mix}$, Fig. 5.8(b).

Counterintuitively, the discharge loss is reduced by increasing M , Fig. 5.8(c). Analyzing the loss individually in different sections of the holes makes this decrease understandable: The loss increases just downstream of the plenum–hole orifices with increasing VR , as expected. This is due to the separation bubble located there, {4}. However, stronger losses are generated downstream in the jetting region and they decrease by increasing M . Summing up, we only see the dominant reducing effect. The discharge loss throughout the cooling hole only (neglecting the plenum) ranges from 0.18 to 0.22, exhibiting the same qualitative behavior as ξ_d . Thereby, the loss of the present configuration is similar to that of diffuser-shaped holes, featuring losses of about 0.1 to 0.2, Gritsch et al. (2005, Fig. 4).

The contribution of the discharge loss ξ_d to the mixture losses $\xi_{s,mix}$, $\xi_{p,t,mix}$ is low, so that they increase with I , Figs. 5.8(b) and 5.8(d). Furthermore, the momentum ratio is the principal scaling parameter in the vicinity of the jet ejections, as discussed in Sec. 5.2.1. This is also

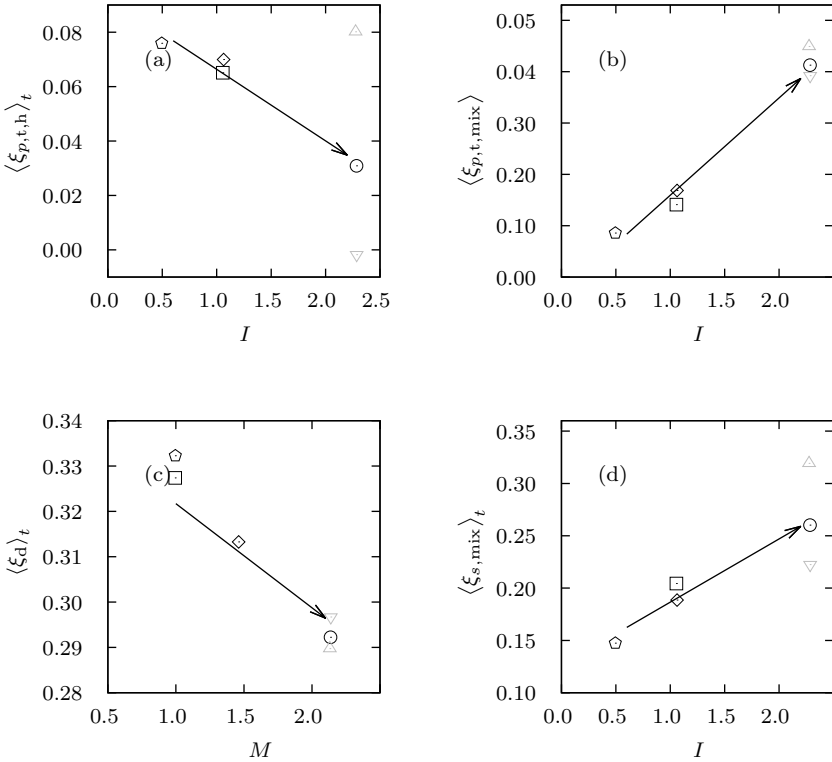


Figure 5.8: Loss coefficients at different blowing conditions. Black symbols: cases 3d α , 3d γ , 3d β , and 31d δ ; gray symbols: cases 41d δ and 51d δ for comparison.

the area in which most of the mixing of the hot gas and the jets takes place. It is, therefore, concluded that the dominant loss mechanism is the mixing loss, increasing with I .

5.3 Effect of yaw angle

So far, the effectiveness contours show large areas of little cooling, Figs. 5.7(a) to 5.7(d). To reduce this drawback, the yaw angle is increased in case 41d δ , Tab. 5.6. Case 51d δ uses a reduced yaw angle to judge the effect of the varied angle more reliably. The high-momentum case 31d δ is the basis for the yaw-angle variation. Thinking in terms of

Table 5.6: Cases with varying yaw angles; common parameters: $\Delta y_{\min}^+ = 2$, $DR \approx 2.0$, $M \approx 2.1$, $I \approx 2.3$, $VR \approx 1.1$.

Symbol, case	β
∇ 51d δ	$\pm 30^\circ$
\circ 31d δ	$\pm 45^\circ$
\triangle 41d δ	$\pm 60^\circ$

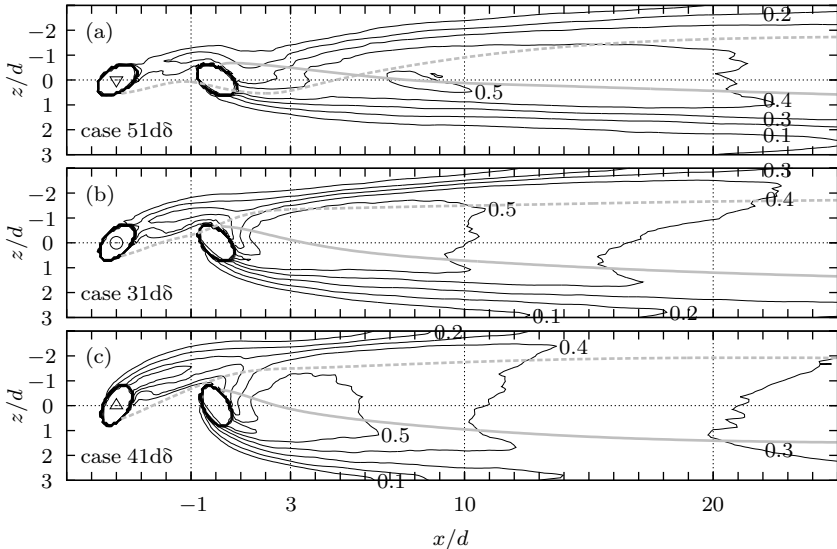


Figure 5.9: Temperature for different yaw angles, analogous to Fig. 5.7.

spatial components of the coolant momentum vector, increasing the yaw angle increases the spanwise and decreases the downstream momentum component.

5.3.1 Cooling at different yaw angles

In the single-jet region upstream of the second ejection, the tendency to detach increases with $|\beta|$, Figs. 5.9(d) to 5.9(g), 5.9(k), and 5.9(o). The reason for this is the higher effective inclination angle with respect to the hot-gas flow, i.e. the ejection angle projected onto an xy -plane.

The increased spanwise momentum, and possibly also the spanwise

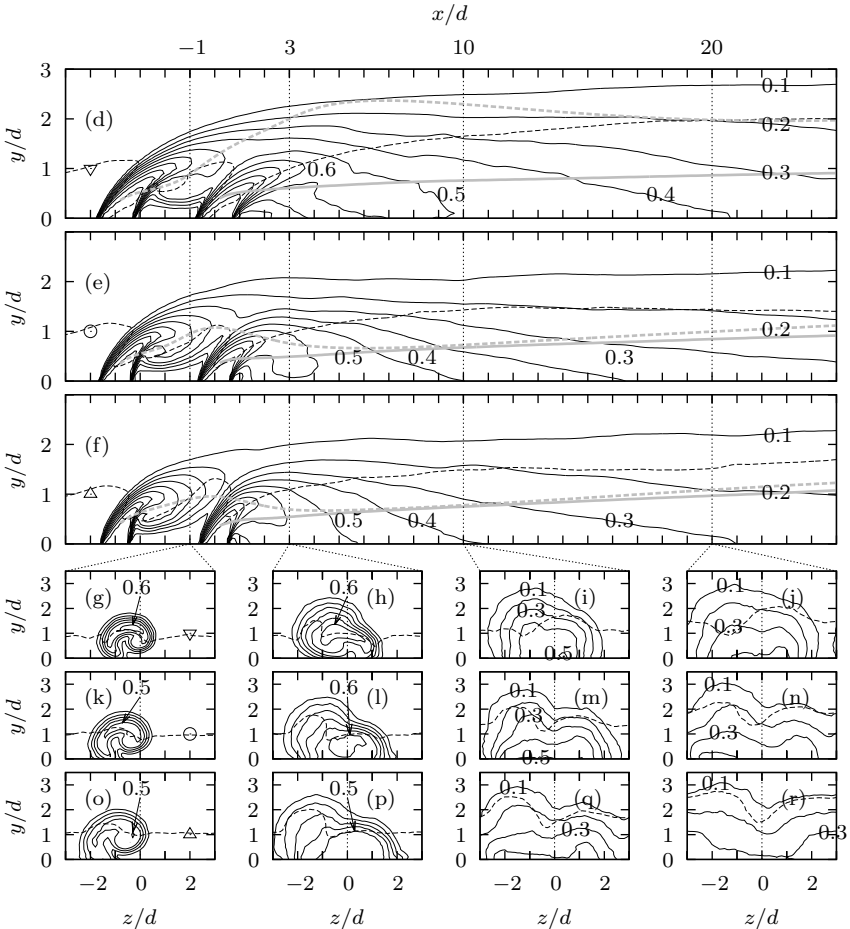


Figure 5.9: (Continued)

broader hole-plate orifice ellipsis, improves the spanwise coolant coverage already in the jet-region, Figs. 5.9(a) to 5.9(c), 5.9(g), 5.9(k), and 5.9(o). This increases the spanwise-averaged effectiveness with the jaw angle, Fig. 5.10(a).

In the jet-interaction region downstream of the second ejection, the increased streamwise momentum again is the driving physical mechanism. It increases the spanwise broadening, denoted by the

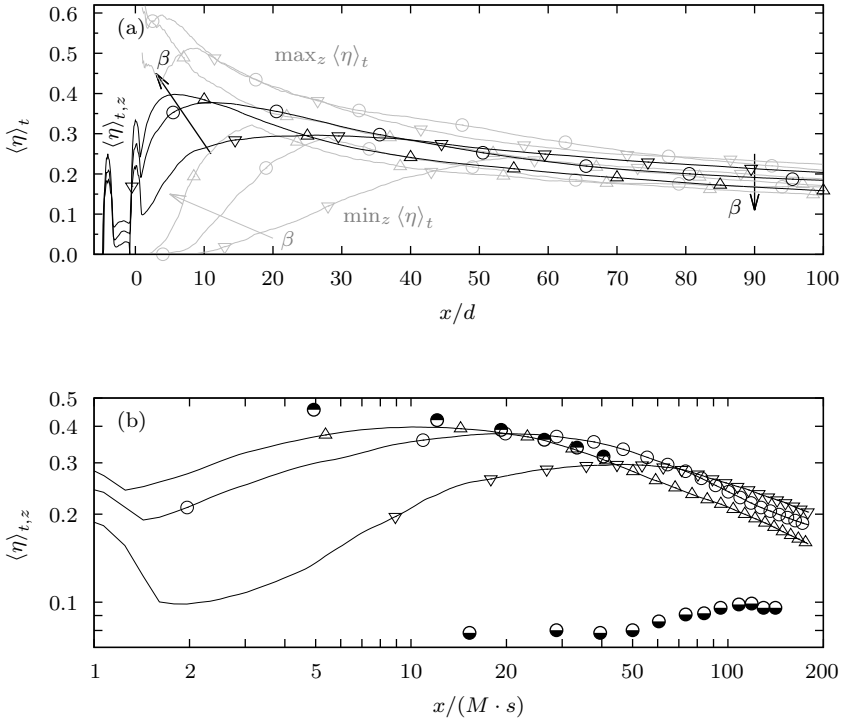


Figure 5.10: (a): Effectiveness for different yaw angles, analogous to Fig. 5.6(a). (b): Comparison of spanwise-averaged effectiveness with experimental cases L7 and L8 (both: $\alpha = 30^\circ$, $\beta = 0^\circ$, $M = 2.0$, $S/d = 0$). \bullet L7: Cylindrical holes from Baldauf et al. (2002) ($L/d = 6$, $P/d = 3$, $DR = 1.8$); \bullet L8: fan-shaped holes from Laveau & Abhari (2010) ($L/d = 5$, $P/d = 4$, $DR = 1.7$); further symbols see Tab. 5.6.

minimum effectiveness in Fig. 5.10(a) and the temperature iso-lines in Figs. 5.9(a) to 5.9(c), 5.9(h), 5.9(l), and 5.9(p). This causes a more rapid increase of η and moves its peak upstream, Fig. 5.10(a). This peak value rises as well since the reduction due to diffusion towards the hot gas has not yet lasted long enough.

The increased spanwise momentum and the increased detachment build up a larger blockage of the hot gas by the coolant. This blockage has a threefold effect that is apparent especially in the diffusion region. First, the spanwise-averaged plate boundary-layer thickness, that can be deduced from Figs. 5.9(i), 5.9(j), 5.9(m), 5.9(n), 5.9(q), and 5.9(r),

thickens with $|\beta|$ since the blockage acts as a tripping device increasing turbulence. Second, the blockage increases the interaction between each jet vortex and the oncoming flow, weakening the anti-kidney vortex pair downstream, Figs. 5.9(j) and 5.9(r). Moreover, the reduced downstream momentum of the jets may favor this weakening. The weaker jets and the improved spanwise spreading of the film shift the diffusion region in the upstream direction. This region is indicated by a nearly constant slope of the spanwise-averaged effectiveness, which almost coincides with the peak of the minimum-effectiveness curve. Another indicator are the spanwise temperature iso-lines which are mainly oriented horizontally for case 41d δ as opposed to case 51d δ , Figs. 5.9(j) and 5.9(r). Third, the blockage increases the interaction between the coolant and hot gas, increasing the mixing in the associated region. Together with the upstream-shifted diffusion region, this results in a reduced spanwise-averaged effectiveness far downstream, Fig. 5.10(a).

For the high-momentum cases, the comparison with cylindrical and fan-shaped holes in Fig. 5.10(b) unveils a good spanwise-averaged effectiveness of the anti-kidney vortex pair. As expected, the cylindrical case L7 shows the lowest effectiveness due to a detached coolant jet. The fan-shaped case L8 shows the highest effectiveness in the vicinity of the coolant ejection, since the jet remains attached and quickly broadens in the spanwise direction. Further downstream, however, the anti-kidney vortex-pair cases 31d δ and 51d δ perform better than case L8, while case 41d δ is similar to case L8. Note that experimental data are compared with coarsely resolved numerical results. Appendix A demonstrates that the coarse simulations are likely to underpredict the experimentally obtained effectiveness by roughly 0.05. This comparison thus is not affected qualitatively by using numerical data for the anti-kidney vortex pair.

5.3.2 Losses at different yaw angles

Comparing the losses of the varied injection angles to those of the varied blowing conditions renders the variation of $\xi_{p,t,mix}$ and ξ_d negligible, Figs. 5.8(b) and 5.8(c). The minor influence of the injection angle on the discharge loss may be due to the yawed flow in the hole-plate orifice ellipsis. In fact, the increases of the total-pressure losses $\xi_{p,t,h}$, $\xi_{p,t,mix}$ with increasing $|\beta|$ are of the same magnitude because of the same blowing conditions of cases 31d δ , 51d δ , and 51d δ , Figs. 5.8(b) and 5.11(a). The increase of the global losses $\xi_{p,t,h}$, $\xi_{p,t,mix}$, and $\xi_{s,t,mix}$ with increasing

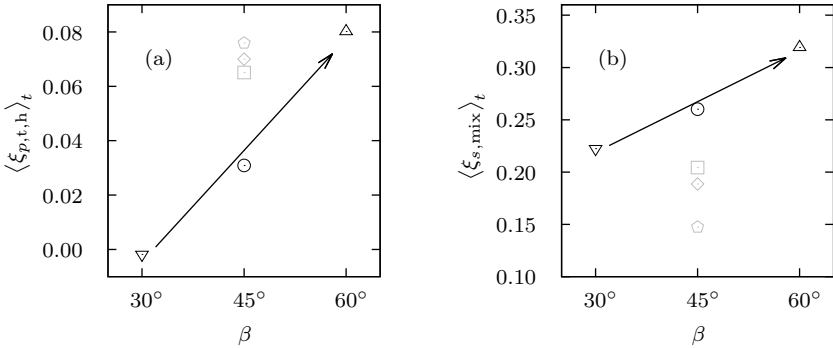


Figure 5.11: Loss coefficients at different yaw angles. Black symbols: cases 31d δ , 41d δ , and 51d δ ; gray symbols: cases 3d α , 3d γ , and 3d β for comparison.

yaw angle, Figs. 5.8(b), 5.11(a), and 5.11(b), is explained as follows. The improved mixing of coolant and hot gas discussed in Sec. 5.3.1 increases the non-isentropic mixing of the two phases and their associated losses.

Interestingly, the influence of the blowing conditions on $\xi_{p,t,mix}$ is stronger than the variation of the yaw angle, whereas the effect of these two parameters on $\xi_{s,mix}$ is comparable. In the present cases, $\xi_{p,t,mix}$ thus scales with the plate-normal component of I , while $\xi_{s,mix}$ scales with the spanwise component of I .

5.4 Summary

Film-cooling configurations exploiting the beneficial anti-kidney vortex-pair system of the coolant jets were investigated by LES for various blowing conditions and yaw angles. The achieved cooling and the generated losses were analyzed to identify the underlying physical mechanisms.

We found that varying the blowing conditions, i.e. the density from $DR = 0.9$ to 2, mass-flux from $M = 1$ to 2.1, momentum from 0.5 to 2.3 and velocity ratios from $VR = 0.5$ to 1.1, results in (a) a variation of the cooling effectiveness just downstream of the jet ejections proportional to the velocity ratio VR , (b) a spanwise spreading proportional to the mass-flux ratio M , (c) the strength of the anti-kidney vortex-pair increasing with the momentum ratio I , but requiring a value of $I \gtrsim 1$, (d) no simple relationship between the downstream cooling efficiency η/M with one of the above ratios alone, (e) increased mixing, being the

principal loss generation mechanism, by increasing the momentum ratio I , and (f) a decreased discharge loss by increasing the mass-flux ratio.

Furthermore, increasing the yaw angle $|\beta|$ from 30° to 60° (g) improves the spanwise spreading, mainly due to an increased spanwise momentum ratio, (h) reduces the cooling effectiveness far downstream, and (i) increases the mixing losses, due to an increased interaction of coolant jets with one another and with the hot gas.

The anti-kidney vortex pair hinders a detachment of the film at high momentum ratios I , where it may even outperform the cooling provided by particular fan-shaped holes some distance downstream of the coolant ejection.

Moreover, a variation of the grid resolution and domain extents showed minor quantitative and, more importantly, no qualitative influence on the results for the considered cases.

Chapter 6

Conclusions and recommendations

Several Large-Eddy Simulations (LES) were conducted using the Finite-Volume flow solver NSMB. The relaxation term of the Approximate-Deconvolution Model (ADM) modeled the sub-grid scales of the turbulent flow and the Synthetic-Eddy Method (SEM) was employed to generate a turbulent inflow. Dirichlet conditions and non-reflecting conditions, both mostly supplemented by sponge zones, were used to account for the flow outside of the computational domain.

For validation of the computational setup, a turbulent flat-plate boundary layer flow was simulated. The results obtained were in good agreement with Direct Numerical Simulation (DNS) data and the law of the wall. The variation of grid topology (used later in the film-cooling simulation), extent of the computational domain, and grid resolution showed only a minor influence on the results.

A film-cooling configuration was investigated including a coolant plenum and two cooling holes. The desired coolant properties at the hole-plenum orifices were obtained by tuning the inflow properties of the plenum. The particular film-cooling configuration simulated is known to generate an anti-kidney vortex pair which is beneficial for the cooling effectiveness. This anti-kidney vortex pair reaches a comparably high film-cooling effectiveness. Our anti-kidney reference case was studied at a rather high resolution and yielded results which agreed reasonably well with experimental data. The flow in the coolant plenum, within the coolant holes, and above the plate was studied in detail focussing on the vortical structures.

Finally, the film-cooling parameters of the reference case were altered towards engine conditions. The resolution was coarsened for this parameter study to allow for multiple simulations with a longer streamwise extent. There was no qualitative and only a minor quantitative effect of the grid coarsening on the cooling effectiveness. The achieved cooling and the generated losses were studied at different coolant-to-freestream mass-flux ratios ($M = 1 \dots 2$) at an engine-like density ratio ($DR = 2$). In addition, the yaw angle influence ($\beta = 30^\circ \dots 60^\circ$) was studied to optimize the spanwise spreading of the film. The simulations show

that the anti-kidney approach may obtain a higher cooling effectiveness for high momentum-ratios than fan-shaped cooling, which so far was assumed to perform better at these parameters. In the vicinity of the cooling holes, however, fan-shaped holes are still superior.

Some major results are as follows. First, local cooling effectiveness maxima are associated with the trajectories of the vortex pair. Second, the combination of coolant injection angles, relative injection position of the two holes, and momentum ratio determines whether an anti-kidney pair will establish or not. Third, a high momentum ratio results in a strong vortex pair whose mutually induced velocity hinders the vortex pair's lift-off. And finally, a larger yaw angle accelerates the spanwise spreading of the film, but at the price of lower cooling effectiveness far downstream due to a more intense mixing with the hot gas.

This work took a look into details of one particular film-cooling arrangement. There are several possible improvements and extensions, which include the computational setup, fewer simplifications, and other film-cooling configurations.

Starting with the computational setup, the MEMCOM data base system of NSMB should be completely removed. MEMCOM causes extra licensing fees and free alternatives, such as HDF5, might be more flexible. The discretization of the diffusive term still extrapolates the block edge and corner values in some situations. This can be circumvented by using a higher order interpolation as proposed by Klinger et al. (2004) at the price of additional memory.

The inflow sponge of the plate boundary-layer may be extended down to the plate to suppress the small-amplitude pressure fluctuations generated there, cf. Bühler & Kleiser (2011). The box of eddies would have to be extended to surround the sponge, which then would have to drive the flow towards an instantaneous reference state given by the SEM. The in- and outflow boundary conditions for the concentration may be formulated using characteristics instead of being extrapolated from the field.

The block-structured grids which we generated using Ansys[®] ICEM[™] CFD show some problems especially in the vicinity of the cooling holes where O-grids are used. There are more specialized grid generators such as GridPro[®], which may be able to generate smoother grids.

Concerning fewer simplifications, one may include surface curvature effects, blade rotation, and oncoming wakes from upstream-passing blades and vanes, to name a few. To finally simulate a whole stage

or even multiple stages, hybrid methods using Reynolds-Averaged Navier-Stokes equations (RANS) and LES should be employed. Solving everything with LES may remain unfeasible for many years, even if the computational power continued to double every 18 months. Therefore, LES of one spanwise slice, as in this work, can be used to provide realistic boundary conditions to (unsteady) RANS (URANS) covering most of the computational domain. The ultimate goal, however, is an LES of a full turbine stage, since the modeling effort and the associated uncertainties are fewer compared to (U)RANS.

Turning towards other film-cooling configurations, most studies concentrate on either perfectly cylindrical or well-defined diffuser-shaped cooling holes. In reality, however, the effective hole shape is strongly influenced by manufacturing tolerances and pollution during operation. Thus a film-cooling geometry is required which is robust with respect to the effective hole geometry. Arrangements using multiple cylindrical holes have the potential of lower manufacturing tolerances than complex diffuser-shaped holes. Second, a novel hole shape by Sargison et al. (2002) starts with a cylindrical hole at the plenum which changes over to a spanwise slot shape at the blade surface. This geometry is most similar to a continuous slot which would be ideal for obtaining a homogeneous cooling film.

Appendix A

Miscellaneous

A.1 Flow chart of NSMB

The flow chart of a calculation is described below. A ghost-cell update includes enforcing of internal and external boundary conditions. Each external boundary-condition update represents a barrier to all MPI processes, i.e. the calculations in each process need to be finished for the update to take place.

- $\underline{V}_{i,j,k}^{n,\text{start}} \leftarrow \text{file}, t \leftarrow t_{\text{start}}$: read data from file ($n = 0$ represents the initial condition of a new calculation and $n > 0$ stands for a continuation of a previous calculation)
- $\underline{U}_{i,j,k}^{n,\text{start}} \leftarrow f(\underline{V}_{i,j,k}^{n,\text{start}})$: compute conservative field
- $\text{file}, \underline{U}_{\text{ref},i,j,k} \leftarrow \underline{U}_{i,j,k}^0$: save reference state for new calculation
 $\underline{U}_{\text{ref},i,j,k} \leftarrow \text{file}$: load reference state for continued calculation
- update ghost cells
- $n = n_{\text{start}} \dots n_{\text{end}}$: time stepping loop
 - $l = 1 \dots 4$: Runge-Kutta sub-stepping loop
 - * $\underline{E}_{\text{NS},i,j,k}^{n+(l-1)/4} \leftarrow f(\underline{U}_{i,j,k}^{n+(l-1)/4})$: compute advective flux
 - * $\underline{E}_{\text{NS},i,j,k}^{n+(l-1)/4} \leftarrow \underline{E}_{\text{NS},i,j,k}^{n+(l-1)/4} + f(\underline{U}_{i,j,k}^{n+(l-1)/4})$: compute and add diffusive flux
 - * $\underline{E}_{\text{hp},i,j,k}^{n+(l-1)/4} \leftarrow f(\underline{U}_{i,j,k}^{n+(l-1)/4})$: compute relaxation term with high-pass filtered field (This includes sixfold application of three one-dimensional filters. After each application of a one-dimensional filter, except the very last one, the ghost cells are updated, i.e. 17 updates altogether. During the computation of this term, the domain boundary-conditions are kept constant.)

- * $\underline{F}_{\text{sponge},i,j,k}^{n+(l-1)/4} \leftarrow f(\underline{U}_{i,j,k}^{n+(l-1)/4}, \underline{U}_{\text{ref},i,j,k})$: compute sponge term
- * $\underline{U}_{i,j,k}^{n+l/4} = \underline{U}_{i,j,k}^n + \frac{1}{5-l} \frac{\Delta t}{V_{i,j,k}} (\underline{F}_{\text{NS}} + \underline{F}_{\text{hp}} + \underline{F}_{\text{sponge}})_{i,j,k}^{n+(l-1)/4}$: perform time integration
- * update ghost cells
- $t \leftarrow t + \Delta t$: advance time
- $\underline{V}_{i,j,k}^{n,\text{end}} \leftarrow f(\underline{U}_{i,j,k}^{n,\text{end}})$: determine primitive field
- file $\leftarrow \underline{V}_{i,j,k}^{n,\text{end}}$: save data to file

A.2 Wall-normal grid stretching

At a wall, located e.g. at grid point x_1 , a finer grid is required compared to the freestream region to resolve occurring steep gradients. This introduces the first two restrictions on the grid spacing: the minimum grid spacing at the wall should not exceed a given value, denoted as Δx_1 , and the maximum grid spacing in the freestream should not exceed a given value, denoted as Δx_{N_x} . A third condition is set up by the accuracy of the differentiation operators which are influenced by the ratio of the size of neighboring grid cells $r_{x,i}$.

$$\Delta x_i = x_{i+1} - x_i \quad , \quad r_{x,i} = \Delta x_{i+1} / \Delta x_i \quad (\text{A.1})$$

To save cells, the grid in the freestream region should be equidistant and the extent of the domain is given by x_{max} . In summary, five conditions are obtained

$$x_1 \stackrel{!}{=} 0 \quad , \quad (\text{A.2}) \quad \Delta x_1 \stackrel{!}{\leq} \Delta x_{\text{min}} \quad , \quad (\text{A.5})$$

$$x_{N_x} \stackrel{!}{=} x_{\text{max}} \quad , \quad (\text{A.3}) \quad \Delta x_i \stackrel{!}{\leq} \Delta x_{\text{max}} \quad , \quad (\text{A.6})$$

$$r_{x,i} \stackrel{!}{\leq} r_{x,\text{max}} \quad . \quad (\text{A.4})$$

Three mappings, i.e. explicit geometrical, explicit exponential, and hyperbolic tangent are discussed in the following using two representative examples, defined as

$$\begin{aligned}
 x_{\max} &= 5 \quad , & x_{\max} &= 5 \quad , \\
 \Delta x_{\min} &= 0.00337 \quad , & \Delta x_{\min} &= 0.020 \quad , \\
 \Delta x_{\max} &= 0.05729 \quad , & \Delta x_{\max} &= 0.336 \quad , \\
 r_{x,\max} &= 1.06 \quad , & r_{x,\max} &= 1.14 \quad .
 \end{aligned}
 \tag{A.7} \qquad \tag{A.8}$$

The explicit geometrical law requires a minimal amount of grid-points. It starts with Δx_{\min} at the wall and continues with a constant stretching ratio of $r_{x,\max}$ until the maximal spacing Δx_{\max} is just not exceeded. From this inflection point (index i_{infl}) on, an equidistant grid using Δx_{\max} is chosen. Mathematically, this reads

$$x_i = \begin{cases} \Delta x_{\min} \frac{1 - r_{x,\max}^{i-1}}{1 - r_{x,\max}} & \text{if } i \in [1 \dots i_{\text{infl}}] \\ x_{i_{\text{infl}}} + \Delta x_{\max}(i - i_{\text{infl}}) & \text{else} \end{cases}
 \tag{A.9}$$

using

$$\begin{aligned}
 i_{\text{infl}} &= 1 + \text{floor} \left(1 + \log r_{x,\max} \frac{\Delta x_{\max}}{\Delta x_{\min}} \right) \quad , \\
 N_x &= i_{\text{infl}} + \text{ceil} \left(\frac{x_{\max} - x_{i_{\text{infl}}}}{\Delta x_{\max}} \right) \quad ,
 \end{aligned}
 \tag{A.10}$$

resulting for the two examples Eqs. (A.7) and (A.8) in

$$\begin{aligned}
 i_{\text{infl}} &= 50 \quad , & i_{\text{infl}} &= 23 \quad , \\
 N_x &= 122 \quad , & N_x &= 31 \quad ,
 \end{aligned}
 \tag{A.11} \qquad \tag{A.12}$$

respectively, as shown in Fig. A.1. Unfortunately, the last point would reside outside the domain in most cases (due to the ceil operation) and the ratio is not smoothly distributed, cf. Fig. A.1.

The explicit exponential law is the slightly modified ansatz employed by the grid generator Ansys[®] ICEM[™] CFD using an exponential function with a polynomial whose coefficients α_l are determined by the conditions of Eqs. (A.2) to (A.6)

$$x_i = \exp(\alpha_4 i^4 + \alpha_3 i^3 + \alpha_2 i^2 + \alpha_1 i + \alpha_0) - 0.1
 \tag{A.13}$$

For the two examples Eqs. (A.7) and (A.8), the coefficients read

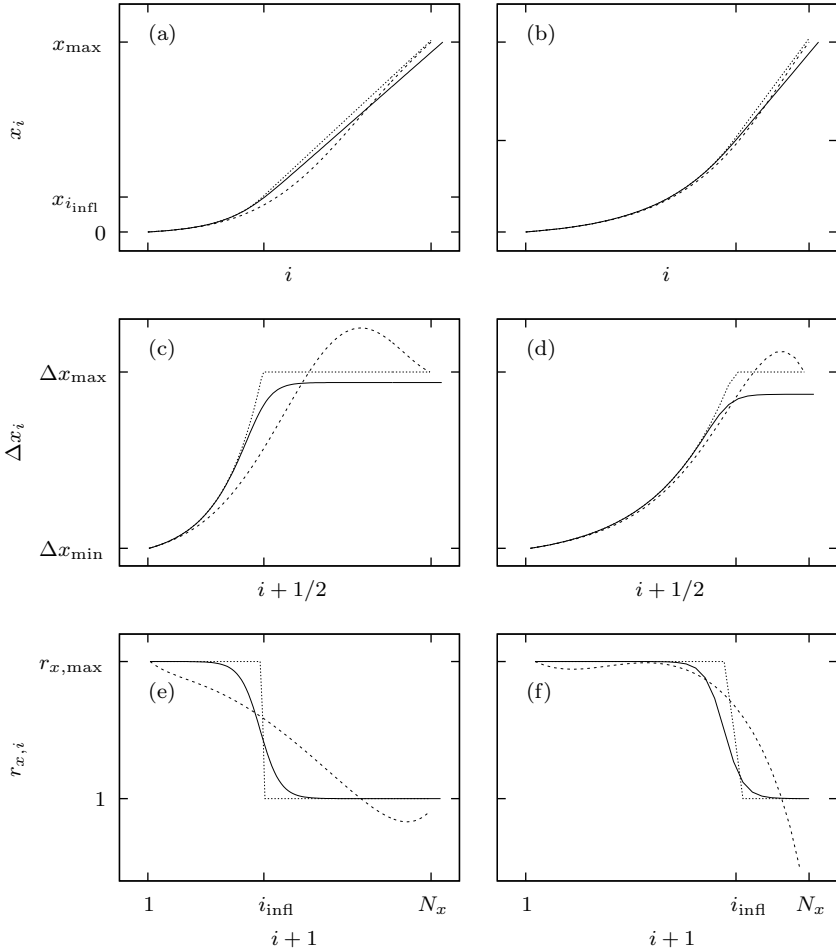


Figure A.1: Grid-point distributions of the two examples following the three laws presented. (a), (c), (e): Example Eq. (A.7), (b), (d), (f): example Eq. (A.8). (a), (b): Grid-point position x_i , (c), (d): grid spacing Δx_i , (e), (f): grid spacing ratio $r_{x,i}$. (.....): Explicit minimal law Eqs. (A.9), (A.11), and (A.12), (---): explicit exponential Fig. A.1 and Eqs. (A.14) and (A.15), (—): implicit hyperbolic tangent Eqs. (A.11), (A.12), and (A.16) to (A.18).

$$\begin{aligned}
 \alpha_0 &= -2.334866431 , & \alpha_0 &= -2.494486076 \\
 \alpha_1 &= 3.183821986 \cdot 10^{-2} , & \alpha_1 &= 1.971167884 \cdot 10^{-1} , \\
 \alpha_2 &= 4.488966414 \cdot 10^{-4} , & \alpha_2 &= -5.436306597 \cdot 10^{-3} , & \text{(A.14)} \\
 \alpha_3 &= 5.796700515 \cdot 10^{-6} , & \alpha_3 &= 2.242291082 \cdot 10^{-4} , \\
 \alpha_4 &= 1.771467681 \cdot 10^{-8} , & \alpha_4 &= -3.727703589 \cdot 10^{-6} .
 \end{aligned}$$

However, this law violates the condition Eq. (A.4) in the example following Eq. (A.8), cf. Fig. A.1.

The implicit hyperbolic tangent law prescribes a smoothly distributed ratio rather than explicitly determining the positions. Choosing a monotonically decreasing function, avoids the violation of Eq. (A.4) if $r_{x,1} \leq r_{x,\max}$. The closer the chosen function follows the step function, the fewer grid-points will be required. In the following, the hyperbolic tangent is chosen (arc tangent would be an alternative choice but its transition is less steep and, thus, would require more grid points). Fixing the inflection point, introducing a steepness factor $\beta > 0$, and setting the asymptotes to $r_{x,\max}$ and 1, the following equation is obtained

$$r_{x,i} = (r_{x,\max} + 1 - (r_{x,\max} - 1) \cdot \tanh(\beta \cdot (i - i_{\text{infl}}))) / 2 \quad . \quad \text{(A.16)}$$

Given the first two grid-points $x_{1,2}$ by Eq. (A.2), Eq. (A.5), respectively, as well as i_{infl} and $N_{x,\tanh}$ as in Eq. (A.10), iterating the evaluation of series Eq. (A.16) on β until Eq. (A.3) is fulfilled ($x_{N_{x,\tanh}}$ too small \rightarrow function too steep $\rightarrow \beta$ too small \rightarrow increase β , vice versa) gives a grid with a smooth transition. If there is no solution after a sufficient number of iterations or Eq. (A.6) is violated (on the last two grid-points), an outer iteration increasing $N_{x,\tanh}$ is to be conducted, cf. Fig. A.2. The coefficients for the two examples Eqs. (A.7) and (A.8) read:

$$\begin{aligned}
 \beta &= 1.166504677 \cdot 10^{-1} , & \beta &= 4.499597539 \cdot 10^{-1} , \\
 N_{x,\tanh} &= 127 \quad , & N_{x,\tanh} &= 32 \quad . & \text{(A.17)} & \text{(A.18)}
 \end{aligned}$$

At the price of additionally required grid-points ($N_{x,\tanh} - N_x$), this distribution fulfills all conditions given in Eqs. (A.2) to (A.6).

A.3 Fourier transform

A discrete Fourier transform

```

 $i_{\text{infl}}, N_{x,\text{tanh}} \leftarrow \text{Eq. (A.10)}$ 
 $x_1 \leftarrow 0$  Eq. (A.2),  $x_2 \leftarrow \Delta x_{\text{min}}$  Eq. (A.5)
 $\beta \leftarrow \text{e. g. } 1, it_{\text{max}} \leftarrow \text{e. g. } 400, \varepsilon \leftarrow \text{e. g. } 10^{-8}$ 
repeat
   $it \leftarrow 0$ 
  repeat
    for  $i = 1 \dots N_{x,\text{tanh}} - 2$  do
       $r_{x,i} \leftarrow \text{Eq. (A.16)}$ 
       $x_{i+2} \leftarrow \text{Eq. (A.1)}$ 
    end for
    if  $|x_{N_{x,\text{tanh}}} - x_{\text{max}}| > \varepsilon$  then
      if  $x_{N_{x,\text{tanh}}} < x_{\text{max}}$  then
         $\beta \leftarrow \beta + \eta$ 
      else
         $\beta \leftarrow \beta - \eta, \beta > 0$ 
      end if
       $it \leftarrow it + 1$ 
    end if
  until  $|x_{N_{x,\text{tanh}}} - x_{\text{max}}| \leq \varepsilon$  or  $it > it_{\text{max}}$ 
  if  $it > it_{\text{max}}$  or  $x_{N_{x,\text{tanh}}} - x_{N_{x,\text{tanh}}-1} > \Delta x_{\text{max}}$  then
     $N_{x,\text{tanh}} \leftarrow N_{x,\text{tanh}} + 1$ 
  end if
until  $|x_{N_{x,\text{tanh}}} - x_{\text{max}}| \leq \varepsilon$  and  $x_{N_{x,\text{tanh}}} - x_{N_{x,\text{tanh}}-1} \leq \Delta x_{\text{max}}$ 

```

Figure A.2: Pseudo-code to evaluate the grid-point distributions according to the implicit hyperbolic tangent law Eq. (A.16).

$$\hat{\phi}(\kappa) = \left| \sum_{n=0}^{N-1} \phi(n) \cdot e^{-i2\pi \frac{\kappa}{N} n} \right| \quad (\text{A.19})$$

is used to determine frequencies and amplitudes of N samples. The absolute value of the complex transformation result is the sinusoid amplitude $\hat{\phi}$, which is the quantity of interest. It is hard to find the dominant frequency, i.e. the frequency with the highest amplitude, in such a spectrum. Furthermore, a Fourier transform is, strictly speaking, only valid for a periodic signal input, which is not present for the somewhat randomly picked sampling period. Therefore, the Hann window function

$$\phi_{\text{Hann}}(n) = \begin{cases} \frac{1}{2} \left(1 - \cos \left(\frac{2\pi(n - n_{\text{win,min}})}{N_{\text{win}} - 1} \right) \right) & \text{if } 0 \leq n - n_{\text{win,min}} < N_{\text{win}} \\ 0 & \text{else} \end{cases} \quad (\text{A.20})$$

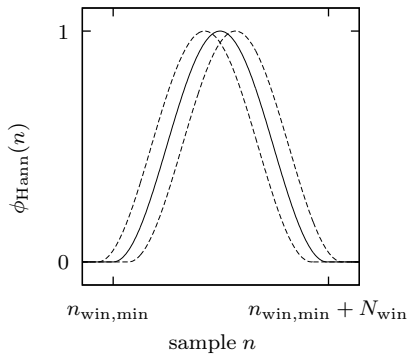


Figure A.3: Hann window function. (—): One instance of function; (---): adjacent, overlapping windows.

is used to generate strongly overlapping windows, containing N_{win} samples, starting from sample $n_{\text{win},\text{min}}$. At the boundaries of these windows, the signal is damped to zero to generate periodic boundaries, cf. Fig. A.3. The data is first windowed, then each window is Fourier transformed, and finally the windows are averaged. This yields a clearer spectrum at the price of lost low frequencies, cf. Figs. 4.23(b), 4.23(c), 4.24(b), and 4.24(c).

The overlap should be as large as possible so that no sequence of the original signal is neglected. A typical overlap that was used for post-processing is depicted in Fig. A.3.

Appendix B

Computational aspects

This chapter discusses computational aspects on the basis of two preliminary simulations listed in Tab. B.1 that are not studied in the rest of the thesis.

First, the performance of principal routines is analyzed for a sequential simulation of a canonical flat-plate turbulent boundary layer case $1bc\alpha$. Second, a strong scaling test of the film-cooling case $33bc\alpha$ is conducted. For both cases, the performance on two different vector architectures is compared.

All computations are carried out on the NEC SX-8 and SX-9 machines at HLRS. Information on some important system parameters are summarized in Tab. B.2. To get the runtime and performance information of different code sequences, the Ftrace routines `ftrace_region_begin` and `ftrace_region_end` are called. Therefore, Ftrace is included during compiling and linking. The binaries are compiled on separate front-ends that are associated with each architecture. The measurements presented compare results obtained on

Table B.1: Computational performance test cases. The resolution bc is between b and c , i.e. $1 < \Delta y_{\min}^+ < \sqrt{2}$. Further parameters as in Tabs. 3.1 and 5.1.

Case	scenario	N_{cell}	N_{block}	x_{max}/d	y_{max}/d
$1bc\alpha$	plate boundary layer	$3 \cdot 10^6$	1	4	3.5
$33bc\alpha$	film cooling	$27 \cdot 10^6$	90	28	7

Table B.2: Important system parameters of the NEC SX installations at HLRS.

Series	# CPUs per Node	peak performance	bandwidth [GByte/s] of	
		per CPU P_{max} [GFLOPS]	memory per CPU	network per node
SX-8	8	16	64	8
SX-9	16	102.4	256	32

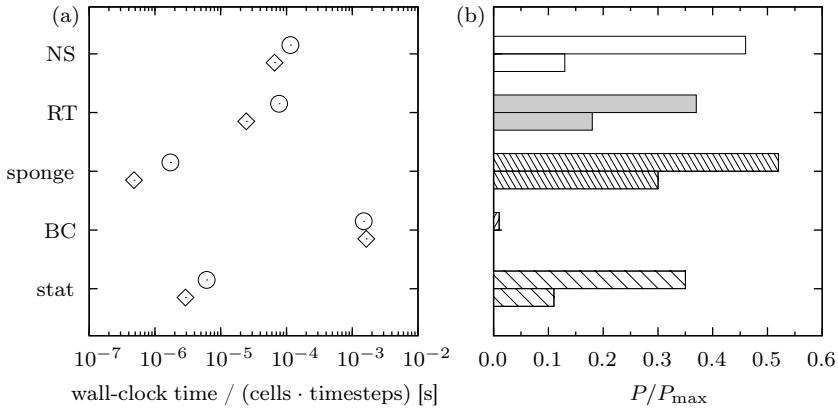


Figure B.1: (a): Timing per cell and (b), \square : relative performance P/P_{\max} of the principal routines on SX-8 (O, upper) and SX-9 (◇, lower).

the two SX-architectures.

B.1 Sequential performance of individual code components

The simple geometry of case 1bc α , a flat-plate turbulent boundary layer, cf. Chap. 3, allows for a single-block topology. Therefore, parallelization overheads like load imbalances or communication time do not appear and the performance of the individual code components can be analyzed. The flow field is sampled for averaging every time step. Besides simple averaging, a number of cross-correlations are computed, too. The data depicted in Fig. B.1 is averaged over 100 timesteps. The graph shows the relative 64-bit floating-point performance P/P_{\max} as well as the time period (in seconds) per timestep and per cell on which the routine is working. Since the single block contains around 3.1 million grid cells, rather high performance rates are obtained. For a computation with converged flow statistics, the grid should be split into multiple blocks to obtain a reasonable turn-around time of the simulation. In the following, the update of the ghost edges as described in Sec. 2.2.2 is not shown separately nor included in the boundary conditions since its share is below 1%.

For the SX-8, the relative performance of the routines acting on

all cells (Navier-Stokes equations (NS) + turbulence model (RT)), cf. Eq. (2.33), is above 35%, cf. Fig. B.1(b). This high value stems from the large portion of vectorizable code and the long vectors that span through the whole field. Consequently, the boundary conditions (BC), acting only on planes of cells obtain a lesser performance of around 1%. The timings in Fig. B.1(a) show that the computation of the sponge zones, cf. last term of Eq. (2.33), and the statistics (stat) is at least one order of magnitude faster compared to the evaluation of the Navier-Stokes equations, cf. Eq. (2.10), and of the turbulence model, cf. last term of Eq. (2.20). Interestingly, the costs to solve the equations of fluid motion are only a bit higher than the costs to model the scales not represented on the grid. The boundary conditions require more than one order of magnitude more time per boundary cell than the evaluation of the Navier-Stokes equations. Fortunately, the number of boundary cells being acted on is, for case 1bc α , about 28 times lower than the total number of cells. Still, the total time spent on evaluating boundary conditions is remarkable, cf. App. B.2.

Considering case 1bc α , the newer machine SX-9 shows a lower level of relative performance for all routines. Therefore, the nominally more than six times higher performance, cf. Tab. B.2, cannot be exploited, which is also observed comparing the timing. Nevertheless, there is a benefit in turn-around time for all routines except for the boundary conditions. Altogether, the computation on the more recent SX-9 is just twice as fast as on the SX-8.

B.2 Overall parallel performance

Case 33bc α represents a film-cooling flow scenario, cf. Chap. 4. It consists of 90 blocks of different extent in physical space and index space. Most of the unstructured block topology, cf. Fig. 4.5, is given by the geometry. Nevertheless, the region above the plate additionally is split to optimize the load balancing for the use of 32 processors ($N_p = 32$). The processors are evenly distributed across the minimum number of nodes. The simulations of 10 timesteps on an increasing number of processors using the same grid incorporating around 27 million cells are measured (strong scaling test).

The relative time share of principal routines averaged over the MPI-processes (one MPI process per processor) used is shown in Fig. B.2. The computational loop is split into Navier-Stokes, turbulence

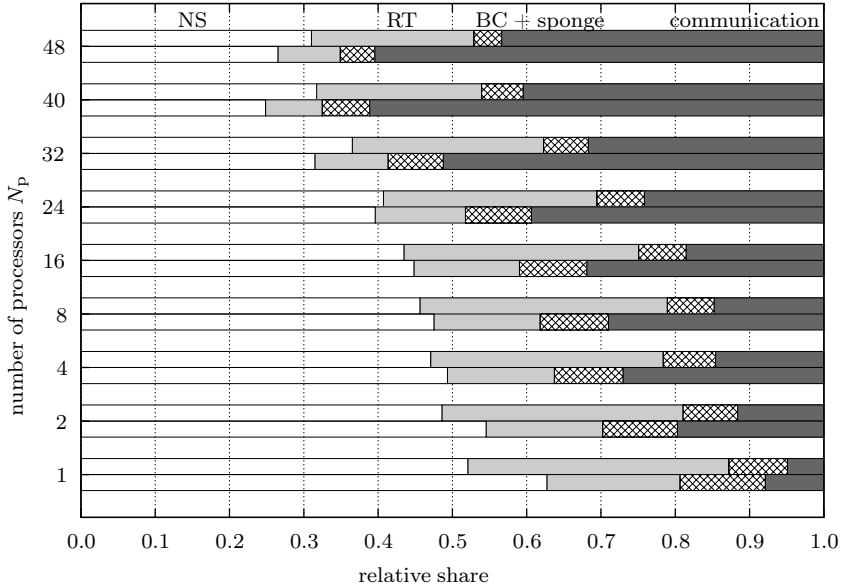


Figure B.2: Relative time share of principal routines on SX-8 (upper) and SX-9 (lower). \square : Navier Stokes (NS); \square : turbulence model (RT); \otimes : boundary treatment (BC + sponge); \blacksquare : communication.

model, boundary treatment (including boundary conditions and sponge zones) and communication part. The communication part includes all ghost-cell updates during repeated filtering (sixfold filtering in three index directions requires $3 \cdot 6 - 1 = 17$ ghost cell updates of the velocities between the filter applications) and time integration, as well as the time that processors have to wait for each other due to load imbalances. For the SX-8, as found in the preceding section, solving the equations of fluid motion and turbulence modeling occupies most of the computing time. Already for the sequential case, a time share of around 5% for ghost-cell updates between the 90 blocks is observed. As discussed before, the low performance of the boundary condition computations plays a minor role. The evaluation of the Navier-Stokes equations, relaxation term and the boundary treatment scales similarly. Increasing the number of processors, the time share of communication increases to over 40%. In this trend, a jump is observed between 32 and 40 processors. This coincides

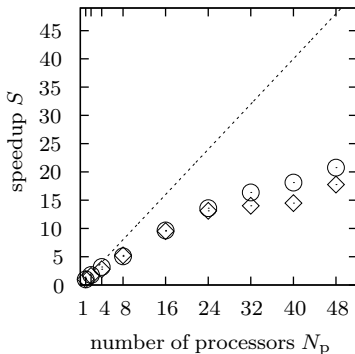


Figure B.3: Speedup of case 33bc α . Ideal speedup (---) and measurements on SX-8 (\circ) and SX-9 (\diamond).

with a kink in the speedup and will be discussed in the next paragraphs.

As apparent in Fig. B.1, the relative time share of the boundary treatment increases for the SX-9 while the filtering performs relatively better compared to the SX-8. For all runs, the relative time spent on communication is higher since the data exchange does not depend on the processor performance but on the network and the memory bandwidth, that both are not six times faster. The configuration using 40 processors distributed across three nodes performs worse, in terms of communication, than using 48 processors. This may be caused by the unequal distribution of 13, 13, and 14 used processors on three nodes.

The speedup S is the ratio of the time t the parallel computation ($N_p > 1$) takes compared to the sequential one ($N_p = 1$),

$$S(N_p) := \frac{t(N_p = 1)}{t(N_p)}. \quad (\text{B.1})$$

Consequently, the ideal speedup would be $S = N_p$. For case 33bc α , Fig. B.3 illustrates the efficiency of the parallel runs based on wall-clock data of 10 timesteps. For the SX-8, a nearly linear speedup with a sub-ideal slope up to 32 processors appears. For the latter configuration, most MPI-processes contain exactly one of the big blocks above the plate, cf. Fig. 4.5, and the others share the remaining blocks that are somehow evenly distributed among them. Beyond 32 processors, the smaller blocks do not fill up the remaining processors sufficiently well, so that they have to idle until the computation of the bigger blocks

is finished. The SX-9 shows an almost identical behavior up to 24 processors. Beyond that limit, the speedup is somewhat lower compared to the SX-8. For 40 processors, a speedup is hardly detectable. To obtain a higher speedup beyond 32 processors, the grid needs to be split-up into more blocks improving the load balancing but introducing additional communication overhead.

B.3 Summary

Computational aspects of boundary-layer and film-cooling simulations with LES using the code NSMB have been discussed. First, the performance of principal routines has been analyzed for a sequential simulation of a canonical flat plate turbulent boundary layer (case $1bc\alpha$). Then, a strong scaling test of the film cooling setup (case $33bc\alpha$) has been conducted. Also, the shift of the share of the most important routines for an increasing number of processors has been documented. The measurements have been compared for the two architectures NEC SX-8 and SX-9.

Concerning the SX-8, from the boundary-layer simulation using a single-block grid (case $1bc\alpha$) it is concluded that the principal routines solving the equations of fluid motion and modeling the turbulence have a high relative performance above 35% of the theoretical peak. The performance of the boundary condition computations is as low as 1%, however, their share of the total computation is small.

For the SX-8, the parallel film-cooling simulations presented (case $33bc\alpha$) show that the share of the communication increases with the number of processors to more than 40% for 48 processors, while the other routines share the remaining computational time with a constant ratio for different numbers of processors. Up to 32 processors, more than half of the ideal speedup is obtained. Obviously, the loss is mainly caused by the time spent on communication.

The SX-9, nominally providing a more than six times higher performance, performs only twice as fast as the SX-8 for the considered case. The relatively slow communication causes its relative share to increase to over 50% already for 32 processors. In the end, the unequal increase of computational performance compared to memory and network access is not beneficial for tightly coupled parallel applications performing frequent communication, as for the considered case $33bc\alpha$.

Bibliography

Previous publications (Gräf et al.) related to the present work are listed at the end of this thesis.

- AGA, V., MANSOUR, M. & ABHARI, R. S. 2009 Aerothermal Performance of Streamwise and Compound Angled Pulsating Film Cooling Jets. *J. Turbomach.* **131** (4), 041015-1–11, DOI: 10.1115/1.3072489.
- AGA, V., ROSE, M. & ABHARI, R. S. 2008 Experimental Flow Structure Investigation of Compound Angled Film Cooling. *J. Turbomach.* **130** (3), 031005-1–8, DOI: 10.1115/1.2775491.
- AHN, J., JUNG, I. S. & LEE, J. S. 2003 Film Cooling from Two Rows of Holes with Opposite Orientation Angles: Injectant Behavior and Adiabatic Film Cooling Effectiveness. *Int. J. Heat Fluid Flow* **24** (1), 91–99, DOI: 10.1016/S0142-727X(02)00200-X.
- BAEHR, H. D. & KABELAC, S. 2009 *Thermodynamik*, 14th edn. Springer.
- BAGHERI, S., SCHLATTER, P., SCHMID, P. J. & HENNINGSON, D. S. 2009 Global Stability of a Jet in Crossflow. *J. Fluid Mech.* **624**, 33–44, DOI: 10.1017/S0022112009006053.
- BALDAUF, S., SCHEURLEN, M., SCHULZ, A. & WITTIG, S. 2002 Correlation of Film-Cooling Effectiveness From Thermographic Measurements at Enginelike Conditions. *J. Turbomach.* **124** (4), 686–698, DOI: 10.1115/1.1504443.
- BARTHET, S. & BARIO, F. 2001 Experimental Investigation of Film Cooling Flow Induced by Shaped Holes on a Turbine Blade. *Ann. N. Y. Acad. Sci.* **934**, 313–320, DOI: 10.1111/j.1749-6632.2001.tb05865.x.
- BODONY, D. J. 2006 Analysis of Sponge Zones for Computational Fluid Mechanics. *J. Comput. Phys.* **212** (2), 681–702, DOI: 10.1016/j.jcp.2005.07.014.
- BOGARD, D. G. & THOLE, K. A. 2006 Gas Turbine Film Cooling. *J. Propu. Power* **22** (2), 249–270, DOI: 10.2514/1.18034.

- BP P.L.C. 2010 BP Statistical Review of World Energy June 2010. URL: <http://bp.com/statisticalreview>.
- BP P.L.C. 2012 BP Energy Outlook 2030. URL: http://www.bp.com/liveassets/bp_internet/globalbp/STAGING/global_assets/downloads/0/2012_2030_energy_outlook_booklet.pdf.
- BRADSHAW, P. 1977 Compressible Turbulent Shear Layers. *Ann. Rev. Fluid Mech.* **9** (1), 33–52, DOI: 10.1146/annurev.fl.09.010177.000341.
- BÜHLER, S. & KLEISER, L. 2011 Inflow Boundary Treatment for the Simulation of Subsonic Jets with Turbulent Nozzle Boundary Layers. *Proc. Appl. Math. Mech.* **11**, 597–598, DOI: 10.1002/pamm.201110288.
- BUNKER, R. S. 2005 A Review of Shaped Hole Turbine Film-Cooling Technology. *J. Heat Transfer* **127** (4), 441–453, DOI: 10.1115/1.1860562.
- BUNKER, R. S. 2007 Gas turbine heat transfer: Ten remaining hot gas path challenges. *J. Turbomach.* **129** (2), 193–201.
- BURDET, A., ABHARI, R. S. & ROSE, M. G. 2007 Modeling of Film Cooling—Part II: Model for Use in Three-Dimensional Computational Fluid Dynamics. *J. Turbomach.* **129** (2), 221–231, DOI: 10.1115/1.2437219.
- CABRAL, B. & LEEDOM, L. C. 1993 Imaging Vector Fields Using Line Integral Convolution. In *Proceedings of the 20th Annual Conference on Computer Graphics and Interactive Techniques*, pp. 263–270. New York: ACM, DOI: 10.1145/166117.166151.
- CHONG, M. S., PERRY, A. E. & CANTWELL, B. J. 1990 A General Classification of Three-Dimensional Flow Fields. *Physics of Fluids A: Fluid Dynamics* **2** (5), 765–777, DOI: 10.1063/1.857730.
- COLBAN, W. F., THOLE, K. A. & BOGARD, D. 2011 A Film-Cooling Correlation for Shaped Holes on a Flat-Plate Surface. *J. Turbomach.* **133** (1), 011002-1–11, DOI: 10.1115/1.4002064.
- COLEMAN, G. N., KIM, J. & MOSER, R. D. 1995 A Numerical Study of Turbulent Supersonic Isothermal-Wall Channel Flow. *J. Fluid Mech.* **305**, 159–183, DOI: 10.1017/S0022112095004587.

- CORTELEZZI, L. & KARAGOZIAN, A. R. 2001 On the Formation of the Counter-Rotating Vortex Pair in Transverse Jets. *J. Fluid Mech.* **446**, 347–373, DOI: 10.1017/S0022112001005894.
- CRIMINALE, W. O., JACKSON, T. L. & JOSLIN, R. D. 2003 *Theory and Computation of Hydrodynamic Stability*. Cambridge University Press.
- DHUNGEL, A., LU, Y., PHILLIPS, W., EKKAD, S. V. & HEIDMANN, J. 2009 Film Cooling From a Row of Holes Supplemented with Antivortex Holes. *J. Turbomach.* **131** (2), 021007-1–10, DOI: 10.1115/1.2950059.
- DUCROS, F., LAPORTE, F., SOULÈRES, T., GUINOT, V., MOINAT, P. & CARUELLE, B. 2000 High-Order Fluxes for Conservative Skew-Symmetric-like Schemes in Structured Meshes: Application to Compressible Flows. *J. Comput. Phys.* **161** (1), 114–139, DOI: 10.1006/jcph.2000.6492.
- FARHADI-AZAR, R., RAMEZANIZADEH, M., TAEIBI-RAHNI, M. & SALIMI, M. 2011 Compound Triple Jets Film Cooling Improvements via Velocity and Density Ratios: Large Eddy Simulation. *J. Fluids Eng.* **133** (3), 031202-1–13, DOI: 10.1115/1.4003589.
- FRIC, T. F. & ROSHKO, A. 1994 Vortical Structure in the Wake of a Transverse Jet. *J. Fluid Mech.* **279**, 1–47, DOI: 10.1017/S0022112094003800.
- GILLEN, D. 2009 International Air Transport in the Future. In *International Transport Research Symposium*, pp. 2009-15-1–23. OECD International Transport Forum, Madrid, Spain, URL: <http://istep2009.cedex.es/downloads/1-Gillen.pdf>.
- GOLDSTEIN, R. J. 1971 Film Cooling. In *Advances in Heat Transfer* (ed. T. F. Irvine, Jr. & J. P. Hartnett), vol. 7, pp. 321–379. New York: Academic Press, DOI: 10.1016/S0065-2717(08)70020-0.
- GOLDSTEIN, R. J., ECKERT, E. R. G. & BURGGRAF, F. 1974 Effects of Hole Geometry and Density on Three-Dimensional Film Cooling. *Int. J. Heat Mass Transfer* **17** (5), 595–607, DOI: 10.1016/0017-9310(74)90007-6.

- GOLDSTEIN, R. J. & JIN, P. 2001 Film Cooling Downstream of a Row of Discrete Holes with Compound Angle. *J. Turbomach.* **123** (2), 222–230, DOI: 10.1115/1.1344905.
- GRITSCH, M., COLBAN, W., SCHÄR, H. & DÖBBELING, K. 2005 Effect of Hole Geometry on the Thermal Performance of Fan-Shaped Film Cooling Holes. *J. Turbomach.* **127** (4), 718–725, DOI: 10.1115/1.2019315.
- GUO, X., SCHRÖDER, W. & MEINKE, M. 2006 Large-Eddy Simulations of Film Cooling Flows. *Comput. Fluids* **35** (6), 587–606, DOI: 10.1016/j.compfluid.2005.02.007.
- HAN, J. C., DUTTA, S. & EKKAD, S. 2000 *Gas Turbine Heat Transfer and Cooling Technology*. New York: Taylor & Francis.
- HARTSEL, J. E. 1972 Prediction of Effects of Mass-Transfer Cooling on the Blade-Row Efficiency of Turbine Airfoils. *AIAA P.* **72-11**, 1–8.
- HAVEN, B. A. & KUROSAKA, M. 1997 Kidney and Anti-Kidney Vortices in Crossflow Jets. *J. Fluid Mech.* **352**, 27–64, DOI: 10.1017/S0022112097007271.
- HAVEN, B. A., YAMAGATA, D. K., KUROSAKA, M., YAMAWAKI, S. & MAYA, T. 1997 Anti-Kidney Pair of Vortices in Shaped Holes and their Influence on Film Cooling Effectiveness. *Tech. Rep.* 97-GT-45. ASME.
- HEIDMANN, J. D. & EKKAD, S. 2008 A Novel Antivortex Turbine Film-Cooling Hole Concept. *J. Turbomach.* **130**, 031020-1–9, DOI: 10.1115/1.2777194.
- HENNIGER, R. 2011 Direct and Large-Eddy Simulation of Particle Transport in Estuarine Environments. PhD thesis, ETH Zurich, DOI: 10.3929/ethz-a-6586770, no. 19656.
- HIRSCH, C. 1988 *Numerical Computation of Internal and External Flows*, 1st edn., vol. 1. John Wiley & Sons.
- HIRSCH, C. 2007 *Numerical Computation of Internal and External Flows*, 2nd edn., vol. 1. Elsevier, ISBN: 978-0-7506-6594-0.

- HUNT, J. C. R., WRAY, A. A. & MOIN, P. 1988 Eddies, Streams, and Convergence Zones in Turbulent Flows. In *Studying Turbulence Using Numerical Simulation Databases 2*, pp. 193–208. URL: <http://adsabs.harvard.edu/abs/1988stun.proc..193H>, proceedings of the 1988 Summer Program.
- HYAMS, D. G. & LEYLEK, J. H. 2000 A Detailed Analysis of Film-Cooling Physics: Part III — Streamwise Injection With Shaped Holes. *J. Turbomach.* **122**, 122–132, DOI: 10.1115/1.555435.
- JARRIN, N. 2008 Synthetic Inflow Boundary Conditions for the Numerical Simulation of Turbulence. PhD thesis, Faculty of Engineering and Physical Sciences, University of Manchester.
- JARRIN, N., BENHAMADOUCHE, S., LAURENCE, D. & PROSSER, R. 2006 A Synthetic-Eddy-Method for Generating Inflow Conditions for Large-Eddy Simulations. *Int. J. Heat Fluid Flow* **27** (4), 585–593, DOI: 10.1016/j.ijheatfluidflow.2006.02.006.
- JAVADI, K., TAEIBI-RAHNI, M. & DARBANDI, M. 2007 Jet-into-Crossflow Boundary-Layer Control: Innovation in Gas Turbine Blade Cooling. *AIAA J.* **45** (12), 2910–2925, DOI: 10.2514/1.28770.
- JEONG, J. & HUSSAIN, F. 1995 On the Identification of a Vortex. *J. Fluid Mech.* **285**, 69–94, DOI: 10.1017/S0022112095000462.
- JUBRAN, B. & BROWN, A. 1985 Film Cooling From Two Rows of Holes Inclined in the Streamwise and Spanwise Directions. *J. Eng. Gas Turbines Power* **107** (1), 84–91, DOI: 10.1115/1.3239701.
- JUBRAN, B. A. & MAITEH, B. Y. 1999 Film Cooling and Heat Transfer from a Combination of Two Rows of Simple and/or Compound Angle Holes in Inline and/or Staggered Configuration. *Heat Mass Transf.* **34** (6), 495–502, DOI: 10.1007/s002310050287.
- VON KAENEL, R. 2003 Large-Eddy Simulation of Compressible Flows Using the Finite-Volume Method. PhD thesis, ETH Zurich, diss. ETH No. 15255.
- VON KAENEL, R., ADAMS, N. A., KLEISER, L. & VOS, J. B. 2003 The Approximate Deconvolution Model for Large-Eddy Simulation of Compressible Flows With Finite Volume Schemes. *J. Fluids Eng.* **125**, 375–381, DOI: 10.1115/1.1567471.

- KANANI, H., SHAMS, M., EBRAHIMI, R. & AHMADIAN, T. 2008 Numerical Simulation of Film Cooling Effectiveness on a Flat Plate. *Internat. J. Numer. Methods Fluids* **56** (8), 1329–1336, DOI: 10.1002/fld.1745.
- KAYS, W., CRAWFORD, M. E. & WEIGAND, B. 2005 *Convective Heat and Mass Transfer*, 4th edn. McGraw-Hill.
- KEIDERLING, F. 2008 Direct Noise Computation of High Reynolds Number Subsonic Jet Flow Using LES. PhD thesis, ETH Zurich, DOI: 10.3929/ethz-a-005771866, no. 17955.
- KLINE, S. J., REYNOLDS, W. C., SCHRAUB, F. A. & RUNSTADLER, P. W. 1967 The Structure of Turbulent Boundary Layers. *J. Fluid Mech.* **30**, 741–773, DOI: 10.1017/S0022112067001740.
- KLINGER, L., VOS, J. B. & APPERT, K. 2004 A simplified gradient evaluation on non-orthogonal meshes; application to a plasma torch simulation method. *Comp. Fluids* **33** (4), 643 - 654, DOI: 10.1016/j.compfluid.2003.07.005.
- KUSTERER, K., BOHN, D., SUGIMOTO, T. & TANAKA, R. 2007 Double-Jet Ejection of Cooling Air for Improved Film Cooling. *J. Turbomach.* **129** (4), 809–815, DOI: 10.1115/1.2720508.
- LAVEAU, B. & ABHARI, R. S. 2010 Influence of Flow Structure on Shaped Hole Film Cooling Performance. *ASME Conf. Proc.* **GT2010-23032**, 1677–1689, DOI: 10.1115/GT2010-23032.
- LEE, S. W., KIM, Y. B. & LEE, J. S. 1997 Flow Characteristics and Aerodynamic Losses of Film Cooling Jets with Compound Angle Orientations. *J. Turbomach.* **119** (2), 310–319, DOI: 10.1115/1.2841114.
- LEE, S. W., LEE, J. S. & RO, S. T. 1994 Experimental Study on the Flow Characteristics of Streamwise Inclined Jets in Crossflow on Flat Plate. *J. Turbomach.* **116** (1), 97–105, DOI: 10.1115/1.2928283.
- LEYLEK, J. H. & ZERKLE, R. D. 1994 Discrete-Jet Film Cooling: A Comparison of Computational Results with Experiments. *J. Turbomach.* **116**, 358–368, DOI: 10.1115/1.2929422.
- LIGRANI, P. M., WIGLE, J. M., CIRIELLO, S. & JACKSON, S. M. 1994 Film-Cooling from Holes with Compound Angle Orientations. Part 1: Results Downstream of Two Staggered Rows of Holes

- with $3d$ Spanwise Spacing. *J. Heat Transfer* **116** (2), 341–352, DOI: 10.1115/1.2911406.
- LINN, J. & KLOKER, M. J. 2008 Numerical Investigations of Film Cooling. In *RESpace—Key Technologies for Reusable Space Systems, Notes on Numerical Fluid Mechanics and Multidisciplinary Design*, pp. 151–169. Springer, DOI: 10.1007/978-3-540-77819-6_9.
- LIU, J., KAPLAN, C. R. & ORAN, E. S. 2006 A Brief Note on Implementing Boundary Conditions at a solid Wall Using the FCT Algorithm. *Tech. Rep.* NRL/MR/6410–06-8943. Naval Research Laboratory, 4555 Overlook Avenue, SW, Washington, DC 20375-5320.
- MAGAGNATO, F., PRITZ, B. & GABI, M. 2006 Inflow Conditions for Large-Eddy Simulation of Compressible Flow in a Combustion Chamber. In *Proceedings of the 5th International Symposium on Turbulence, Heat and Mass Transfer* (ed. Y. N. K. Hanjalić & S. Jakirlic), pp. 1–6. Dubrovnic, Croatia, URL: http://www.dl.begellhouse.com/download/article/5d7357c84dc0a9c3/MAGAGNATO_PRITZ_GABI.PDF.
- MCGOVERN, K. T. & LEYLEK, J. H. 2000 A Detailed Analysis of Film Cooling Physics: Part II — Compound-Angle Injection With Cylindrical Holes. *J. Turbomach.* **122**, 113–121, DOI: 10.1115/1.555434.
- MENDEZ, S. & NICOUD, F. 2008 Large-Eddy Simulation of a Bi-Periodic Turbulent Flow with Effusion. *J. Fluid Mech.* **598**, 27–65, DOI: 10.1017/S0022112007009664.
- MONKEWITZ, P. A., CHAUHAN, K. A. & NAGIB, H. M. 2007 Self-consistent High-Reynolds-Number Asymptotics for Zero-Pressure-Gradient Turbulent Boundary Layers. *Phys. Fluids* **19**, 115101-1–12, DOI: 10.1063/1.2780196.
- MONKEWITZ, P. A., CHAUHAN, K. A. & NAGIB, H. M. 2008 Comparison of Mean Flow Similarity Laws in Zero Pressure Gradient Turbulent Boundary Layers. *Phys. Fluids* **20**, 105102-1–16, DOI: 10.1063/1.2972935.
- MÜLLER, S. 2007 Numerical Investigations of Compressible Turbulent Swirling Jet Flows. PhD thesis, ETH Zurich, DOI: 10.3929/ethz-a-005523326, no. 17375.

- PAMIÈS, M. 2008 Contrôle d'une couche limite turbulente au moyen d'un micro-système distribué. PhD thesis, Université Lille 1.
- PAMIÈS, M., WEISS, P.-E., GARNIER, E., DECK, S. & SAGAUT, P. 2009 Generation of synthetic turbulent inflow data for large eddy simulation of spatially evolving wall-bounded flows. *Phys. Fluids* **21** (4), 045103, DOI: 10.1063/1.3103881.
- PEDERSEN, D. R., ECKERT, E. R. G. & GOLDSTEIN, R. J. 1977 Film cooling with large density differences between the mainstream and the secondary fluid measured by the heat-mass transfer analogy. *J. Heat Transfer* **99** (4), 620–627, DOI: 10.1115/1.3450752.
- PEET, Y. V. 2006 Film Cooling from Inclined Cylindrical Holes Using Large Eddy Simulations. PhD thesis, Stanford University, URL: http://www.mcs.anl.gov/~peet/thesis_ypeet_single.pdf, UMI Number: 3235321.
- PETKOV, A. P. 2006 Transparent Line Integral Convolution: a New Approach for Visualizing Vector Fields in OpenDX. Master's thesis, University of Montana, Missoula, Montana, supervisor: Jesse V. Johnson.
- PEYRET, R. & TAYLOR, T. D. 1983 *Computational Methods of Fluid Flow*. Springer.
- PIETRZYK, J. R., BOGARD, D. G. & CRAWFORD, M. E. 1989 Hydrodynamic Measurements of Jets in Crossflow for Gas Turbine Film Cooling Applications. *J. Turbomach.* **111**, 139–145, DOI: 10.1115/1.3262248.
- POINSOT, T. J. & LELE, S. K. 1992 Boundary conditions for direct simulations of compressible viscous flows. *J. Comput. Phys.* **101** (1), 104–129, DOI: 10.1016/0021-9991(92)90046-2.
- QUADRIO, M. & LUCHINI, P. 2003 Integral Space-Time Scales in Turbulent Wall Flows. *Phys. Fluids* **15**, 2219–2227, DOI: 10.1063/1.1586273.
- RENZE, P., SCHRÖDER, W. & MEINKE, M. 2007 LES of Film Cooling Efficiency for Different Hole Shapes. In *5th Int. Symp. Turbulence Shear Flow Phenomena*, pp. 683–688. Munich.
- RENZE, P., SCHRÖDER, W. & MEINKE, M. 2008 Large-Eddy Simulation of Film Cooling Flows at Density Gradients. *Int. J. Heat Fluid Flow* **29** (1), 18–34, DOI: 10.1016/j.ijheatfluidflow.2007.07.010.

- RENZE, P., SCHRÖDER, W. & MEINKE, M. 2009 Large-Eddy Simulation of Interacting Film Cooling Jets. *ASME Conf. Proc.* **GT2009-5916**, 81–90, DOI: 10.1115/GT2009-59164.
- RIZZI, A. 1978 Numerical Implementation of Solid-Body Boundary Conditions for the Euler Equations. *Z. angew. Math. Me.* **58** (7), T301–T304, DOI: 10.1002/zamm.19780580703.
- ROBINSON, S. K. 1991 Coherent Motions in the Turbulent Boundary Layer. *Ann. Rev. Fluid Mech.* **23**, 601–639, DOI: 10.1146/annurev.fl.23.010191.003125.
- SAGAUT, P. 2006 *Large Eddy Simulation for Incompressible Flows—an Introduction*, 3rd edn. Springer Verlag.
- SARGISON, J. E., GUO, S. M., OLDFIELD, M. L. G., LOCK, G. D. & RAWLINSON, A. J. 2002 A Converging Slot-Hole Film-Cooling Geometry—Part 1: Low-Speed Flat-Plate Heat Transfer and Loss. *J. Turbomach.* **124** (3), 453–460, DOI: 10.1115/1.1459735.
- SCHLATTER, P. 2005 Large-Eddy Simulation of Transition and Turbulence in Wall-Bounded Shear Flow. PhD thesis, ETH Zurich, diss. ETH No. 16000.
- SCHLATTER, P., ÖRLÜ, R., LI, Q., BRETHOUWER, G., FRANSSON, J. H. M., JOHANSSON, A. V., ALFREDSSON, P. H. & HENNINGSON, D. S. 2009 Turbulent Boundary Layers up to $Re_\delta = 2500$ Studied through Simulation and Experiment. *Phys. Fluids* **21**, 051702-1–4, DOI: 10.1063/1.3139294.
- SCHLATTER, P., STOLZ, S. & KLEISER, L. 2004 LES of Transitional Flows Using the Approximate Deconvolution Model. *Int. J. Heat Fluid Flow* **25** (3), 549–558, DOI: 10.1016/j.ijheatfluidflow.2004.02.020.
- SCHLICHTING, H. 1979 *Boundary-Layer Theory*, 7th edn. McGraw-Hill.
- SCHLICHTING, H. & GERSTEN, K. 2006 *Grenzschichttheorie*, 10th edn. Springer.
- SCHLÜTER, J. U. & SCHÖNFELD, T. 2000 LES of Jets in Cross Flow and Its Application to a Gas Turbine Burner. *Flow, Turb. and Combust.* **65**, 177–203, DOI: 10.1023/A:1011412810639.

- SINHA, A. K., BOGARD, D. G. & CRAWFORD, M. E. 1991*a* Film-Cooling Effectiveness Downstream of a Single Row of Holes with Variable Density Ratio. *J. Turbomach.* **113** (3), 442–449, DOI: 10.1115/1.2927894.
- SINHA, A. K., BOGARD, D. G. & CRAWFORD, M. E. 1991*b* Gas Turbine Film Cooling: Flowfield Due to a Second Row of Holes. *J. Turbomach.* **113** (3), 450–456, DOI: 10.1115/1.2927895.
- SOARES, C. 2007 *Gas Turbines*. Elsevier, URL: <http://www.sciencedirect.com/science/book/9780750679695>, ISBN: 978-0-7506-7969-5.
- SPALART, P. R. 1988 Direct Simulation of a Turbulent Boundary Layer up to $Re_\theta = 1410$. *J. Fluid Mech.* **187**, 61, DOI: 10.1017/S0022112088000345.
- STOLZ, S. 2000 Large-Eddy Simulation of Complex Shear Flows Using an Approximate Deconvolution Model. PhD thesis, ETH Zurich, diss. ETH No. 13861.
- STOLZ, S. & ADAMS, N. A. 1999 An approximate deconvolution procedure for large-eddy simulation. *Phys. Fluids* **11**, 1699–1701.
- STOLZ, S., ADAMS, N. A. & KLEISER, L. 2001 The Approximate Deconvolution Model for Large-Eddy Simulations of Compressible Flows and its Application to Shock-Turbulent-Boundary-Layer Interaction. *Phys. Fluids* **13** (10), 2985–3001, DOI: 10.1063/1.1397277.
- SUNDEN, B. & XIE, G. 2010 Gas Turbine Blade Tip Heat Transfer and Cooling: A Literature Survey. *Heat Transfer Engineering* **31** (7), 527–554, DOI: 10.1080/01457630903425320.
- SWANSON, R. C. & TURKEL, E. 1997 Multistage Schemes With Multigrid for Euler and Navier-Stokes Equations. Tech. Paper 3631. NASA Langley.
- VON TERZI, D. A., SANDBERG, R. D. & FASEL, H. F. 2009 Identification of Large Coherent Structures in Supersonic Axisymmetric Wakes. *Comp. Fluids* **38** (8), 1638–1650, DOI: 10.1016/j.compfluid.2009.01.007.

- THOMPSON, K. W. 1987 Time Dependent Boundary Conditions for Hyperbolic Systems. *J. Comput. Phys.* **68**, 1–24, DOI: 10.1016/0021-9991(87)90041-6.
- THOMPSON, K. W. 1990 Time Dependent Boundary Conditions for Hyperbolic Systems, II. *J. Comput. Phys.* **89**, 439–461, DOI: 10.1016/0021-9991(90)90152-Q.
- TRUESDELL, C. A. 1954 *The Kinematics of Vorticity*. Indiana University Publications Science Series 19. Bloomington: Indiana University Press.
- TYAGI, M. 2003 Large Eddy Simulations of Complex Turbulent Flows. PhD thesis, Indian Institute of Technology, Kanpur, URL: http://etd.lsu.edu/docs/available/etd-0214103-162012/unrestricted/Tyagi_dis.pdf.
- VOS, J. B., VAN KEMENADE, V., YTTERSTRÖM, A. & RIZZI, A. W. 1997 Parallel NSMB: An Industrialized Aerospace Code for Complete Aircraft Simulations. In *Parallel Computational Fluid Dynamics 1996* (ed. P. Schiano, A. Ecer, J. Periaux & N. Satofuka), pp. 49–58. Amsterdam: North-Holland, DOI: 10.1016/B978-044482327-4/50073-5.
- WALTERS, D. K. & LEYLEK, J. H. 2000 A Detailed Analysis of Film-Cooling Physics: Part I—Streamwise Injection With Cylindrical Holes. *J. Turbomach.* **122**, 102–112, DOI: 10.1115/1.555433.
- WEGENKITTL, R., GROLLER, E. & PURGATHOFER, W. 1997 Animating Flow Fields: Rendering of Oriented Line Integral Convolution. In *Computer Animation '97*, pp. 15–21. DOI: 10.1109/CA.1997.601035.
- WILCOX, D. C. 2000 *Basic Fluid Mechanics*, 2nd edn. La Cañada: DCW Industries.
- YAO, Y. & MAIDI, M. 2011 Direct Numerical Simulation of Single and Multiple Square Jets in Cross-Flow. *J. Fluids Eng.* **133** (3), 031201–1–10, DOI: 10.1115/1.4003588.
- YUAN, L. L. & STREET, R. L. 1998 Trajectory and Entrainment of a Round Jet in Crossflow. *Phys. Fluids* **10** (9), 2323–2335, DOI: 10.1063/1.869751.

- ZIEFLE, J. 2008 Large-Eddy Simulation of Complex Massively-Separated Turbulent Flows. PhD thesis, ETH Zurich, no. 17846.
- ZIEFLE, J. & KLEISER, L. 2008 Assessment of a Film-Cooling Flow Structure by Large-Eddy Simulation. *J. Turbul.* **9** (29), 1–25, DOI: 10.1080/14685240802232855.
- ZIEFLE, J. & KLEISER, L. 2009 Large-Eddy Simulation of Round Jet in Crossflow. *AIAA J.* **47** (5), 1158–1172, DOI: 10.2514/1.38465.

Publications

Parts of this thesis have been published as listed below.

- GRÄF, L. & KLEISER, L. 2010 Large-Eddy Simulation of Double-Row Compound-Angle Film-Cooling: Computational Aspects. In *High Performance Computing on Vector Systems 2010* (ed. M. Resch, K. Benkert, X. Wang, M. Galle, W. Bez, H. Kobayashi & S. Roller), pp. 185–196. Berlin: Springer, DOI: 10.1007/978-3-642-11851-7_14.
- GRÄF, L. & KLEISER, L. 2011*a* Flow-Field Analysis of Anti-Kidney Vortex Film-Cooling. In *Proceedings of the 10th International Symposium on Experimental and Computational Aerothermodynamics of Internal Flows*, pp. 1–10. Brussels, Belgium.
- GRÄF, L. & KLEISER, L. 2011*b* Large-Eddy Simulation of Double-Row Compound-Angle Film Cooling: Setup and Validation. *Comput. Fluids* **43** (1), 58–67, DOI: 10.1016/j.compfluid.2010.09.032.
- GRÄF, L. & KLEISER, L. 2012*a* Film Cooling Using Anti-Kidney Vortex Pairs at Different Blowing Conditions and Yaw Angles pp. 1–10, submitted.
- GRÄF, L. & KLEISER, L. 2012*b* Flow-Field Analysis of Anti-Kidney Vortex Film-Cooling. *J. Therm. Sci.* **21** (1), 66–76, DOI: 10.1007/s11630-012-0520-y.

Curriculum vitae

Name	Lars Gräf
Date of birth	December 30, 1980
Place of birth	Tübingen, Germany
Nationality	German
since	PhD. student and research assistant at the Institute of Fluid Dynamics, ETH Zürich
July 2007	
Apr.	Visiting researcher at the Institute of Aero- and Gas Dynamics, Universität Stuttgart
to June 2010	
June 2007	Dipl.-Ing. Universität Stuttgart
Mar.	Research assistant at the High Performance Computing Center Stuttgart
to May 2007	
Oct. 2001	Mechanical Engineering
to Feb. 2007	at Universität Stuttgart
Sep. 2006	Diploma thesis
to Feb. 2007	at DaimlerChrysler AG, Stuttgart
Oct. 2005	Internship at BMW Group, München
to Feb. 2006	
Aug.	Internships in Mössingen and Reutlingen
to Sep. 2001	
Sep. 2000	Civilian service
to July 2001	at Gustav Werner Stiftung, Reutlingen
June 2000	Abitur (graduation from high-school) at Quenstedt-Gymnasium Mössingen